

Geometrical Distortion of Magnetic Resonance Images

Alain Gauvin

Department of Physics
McGill University, Montréal

May, 1992

A thesis submitted to the Faculty of Graduate Studies and Research
in partial fulfillment of the requirements for the degree of
Master of Science.

©Alain Gauvin, 1992.

Abstract

The problem of geometrical distortion in MR images is addressed in the context of the applicability of stereotactic techniques. For this purpose, the distortion of phantom images is measured at various readout bandwidths and the spatial linearity is evaluated in view of the use of a stereotactic frame. The presence of a contribution to the overall distortion of non-linear magnetic gradients is shown from the data, although the distortion observed seems to be mostly attributable to the main field inhomogeneity. The specific problems of distortion of the fiducial markers due to bulk magnetic susceptibility effects is addressed. The occurrence of such effects is characterized with the help of imaging, and the role of the phenomenon on proper target localization is demonstrated. In addition, a method of bypassing the detrimental aspect of these effects is presented.

Various distortion correction approaches are discussed, and their benefits and drawbacks are evaluated. In the light of this discussion, a recently reported correction method is then presented. This method allows the calculation of an image free from geometrical and intensity distortion from the combined effect of main field inhomogeneity, susceptibility effects and chemical shift. Two input images acquired at two different readout gradient strengths are necessary to allow the post-processing from which the final image is obtained. The general details of the implementation of this method are discussed along with the considerations related to its adaptation for stereotaxy. A program based on this technique was developed and tested with the images of a phantom of known geometry mounted in the stereotactic frame. This allows for the evaluation of the linearity of the processed images with the help of stereotactic techniques. The effectiveness of the program is thereby demonstrated. Degradation in image quality, observed with the presented adaptation, is discussed and a remedy is suggested.

Resumé

Le problème de la distorsion des images de résonance magnétique est étudié en vue de leur adaptation pour les besoins de la stéréotaxie. Ainsi, la distorsion des images d'un fantôme est évaluée à différentes largeurs de bande de codage en fréquence et la linéarité spatiale des images est vérifiée pour l'utilisation d'un cadre stéréotactique. La contribution de l'effet caractéristique de gradients magnétiques non-linéaires est mise en évidence, bien qu'il soit démontré que la non-uniformité du champ magnétique principal est dominante à cet égard. Le problème particulier de susceptibilité magnétique des marqueurs stéréotactiques en terme de distorsion est abordé. La présence de ce type de phénomène est démontrée et son impact négatif sur l'aptitude à localiser une cible avec exactitude est souligné. De plus, une solution au problème est présentée.

Plusieurs méthodes de correction de la distorsion des images de résonance magnétique sont discutées. Les avantages et inconvénients des différentes techniques sont énoncés et ceci est suivi de la présentation d'une récente méthode de correction. Cette méthode permet l'obtention d'images exemptes de distorsion spatiale et d'intensité due à l'effet combiné de la non-uniformité du champ principal, la susceptibilité magnétique et le décalage chimique de la fréquence. Deux images acquises à l'aide de deux différentes bandes de codage en fréquence sont requises pour procéder au traitement conduisant à l'obtention de l'image finale. Le détail de l'implantation numérique de cette technique est discuté de même que les considérations plus directement reliées à la stéréotaxie. Un programme basé sur cette méthode a été développé et testé avec les images d'un fantôme de géométrie connue placé dans un cadre stéréotactique. Cette façon de faire permet l'évaluation de la linéarité des images ainsi traitées grâce aux techniques stéréotactiques. L'efficacité de cette approche est démontrée. La détérioration de la qualité de l'image suivant l'application du traitement est discutée et une solution est proposée.

Acknowledgements

I first wish to express my sincere gratitude to my supervisor, Dr. Terry Peters, for his encouragement and advice throughout my work at the MNI. Especially, I appreciate the confidence Dr. Peters showed in me and in my course of action in carrying out this project.

I thank the members of the Neuro-Imaging Laboratory for their friendship and encouragement. Particularly, I am grateful to Chris Henri who initiated me to the features of the stereotactic workstation and who never hesitated to spend time to provide both help and advice. I appreciate the help of Glenna Waters for her patient proofreading of the manuscript and, of course, for her unfailing and invaluable support. Thanks to Jacqueline Fortin for her talented help with some of the figures and Thilaka Sunanawecera of Stanford University for helpful exchanges.

Financial support from the Natural Sciences and Engineering Research Council of Canada is gratefully acknowledged.

Preface

The problem of distortion in Magnetic Resonance Imaging is probably as old as the modality itself, having been addressed even before the arrival of spin-warp imaging [29,51]. The stringent main field homogeneity needed for magnetic resonance imaging (MRI) was in the earlier days of this technology a requirement that was poorly met by today's standards and this often constituted the main limitation in the geometrical integrity of the images.

The dramatical increase of the popularity of MRI was accompanied by an improvement in magnet design which decreased the problem of homogeneity as well as geometrical distortion of MR images. Nonetheless, this caused some elements of image accuracy limitation, namely magnetic gradient field non-linearity, eddy currents, magnetic susceptibility of the interrogated material and chemical-shift effect, to play a relatively greater role. At present, this image quality parameter is generally of limited concern except in the field of stereotaxy, or in the utilization of patient diagnostic image information to spatially direct the use of some active therapeutic or diagnostic measure, which calls for image accuracy better than $1mm$.

This work was conducted at the Montreal Neurological Institute (MNI) where stereotaxy has been the object of an intensive research effort whose main accomplishment was probably the development of the OBT (Olivier-Bertrand-Tipal) stereotactic frame [44,88,89,91,93]. Since this device was from the beginning intended to be used with a variety of imaging modalities, some comparative experience was gained concerning the accuracy of MR images with respect to other diagnostic techniques such as computed

tomography (CT) and digital subtraction angiography (DSA). This revealed the limitation of the accuracy of position calculation as performed with the help of MR images that eventually convinced the local practitioners of stereotaxy to reserve the use of this modality for qualitative purposes.

However, the unique nature of the diagnostic information obtained through MRI limits the potential of stereotactic techniques that lack this imaging modality. Hence, the question of distortion in MRI has been examined in the specific context of the use of the OBT frame [27,35,94,95]. This thesis represents another aspect of this investigation. However, while the previous efforts generally focussed on the problem in an empirical way, a more fundamental approach is adopted here.

Chapter 1 introduces in a general way the two elements that motivated this work, namely stereotaxy and image distortion. Chapter 2 begins with an overview of the principles of NMR, and also of MRI in non-ideal conditions. Following this, the main causes of geometrical distortion of MR images are tackled. Chapter 3 presents experimental data acquired with the help of a phantom to evaluate the image distortion. An analysis is carried out in view of obtaining an interpretation revealing the distinct roles of some of the known causes of geometrical distortion. As well, Chapter 3 treats the problem of distortion of the fiducial markers from bulk magnetic susceptibility effects. Note that this last element was both discovered and characterized in the course of this work. Chapter 4 constitutes a brief introduction to the ways to counteract the problem of geometrical distortion of MR images. Chapter 5 is a study of a recent distortion correction method whose implementation was investigated. Finally, Chapter 6 presents the conclusions obtained from this work.

The contributions of this thesis are

- Analysis of the spatial linearity over the volume required for stereotactic MR imaging with the OBT stereotactic frame.
- Differentiation of the contributions of inherent causes of distortion over this same volume.

- Characterization of a bulk magnetic susceptibility effect that causes the fiducial marker plate to exhibit a distortion effect which is dependent on its orientation with respect to the main magnetic field. The consequences of this phenomenon on the accuracy of position calculation with the help of stereotaxy are evaluated
- Investigation of a recent distortion correction method and quantitative validation of its efficiency in the context of stereotaxy.

Contents

Abstract	i
Résumé	ii
Acknowledgements	iii
Preface	iv
1 Introduction	1
1.1 Image distortion	1
1.2 Stereotaxy	3
1.2.1 Development of Stereotaxy	3
1.2.2 Modern stereotaxy	5
1.3 Objectives	8
2 Theory and principles	10
2.1 Nuclear magnetic resonance	10
2.2 Magnetic Resonance Imaging	14
2.2.1 Introduction	14
2.2.2 Imaging in non-ideal conditions	15
2.3 Signal-to-noise ratio	22

2.4	Magnetic susceptibility and chemical shift effect	24
2.5	Eddy currents	26
2.6	Conclusion	29
3	Distortion in the context of stereotaxy	30
3.1	Main field homogeneity and gradient field linearity	30
3.2	Contribution of the main field inhomogeneity to inherent distortion	38
3.3	Transient currents effect on spatial linearity	44
3.4	OBT stereotaxy frame	44
3.5	Localization with the fiducial markers	47
3.6	Distortion on the fiducial markers	49
3.6.1	Influence of the stereotactic frame on marker positioning	49
3.6.2	BMS shift effect on the markers	51
3.7	Effect of top plate distortion on accuracy of localization	64
3.8	Conclusion	66
4	Distortion correction methods	68
4.1	B_0 inhomogeneity correction using hardware methods	68
4.2	Correction using <i>a priori</i> distortion knowledge	71
4.3	Other correction methods	73
5	Image correction using double-gradient acquisition	76
5.1	Theory	77

5.2	Effect of slice selection	79
5.3	Miscellaneous considerations	82
5.3.1	Image intensity normalization	82
5.3.2	Repositioning of the fiducial markers	84
5.3.3	Application of the differential equation	85
5.4	Algorithm	87
5.5	Experimental results	89
5.5.1	Evaluation of image accuracy using stereotaxy	89
5.5.2	Digitization errors	94
6	Conclusion	98
6.1	Summary	98
6.2	Future work	101
	Bibliography	103
	Glossary	115

List of Figures

1.1	Types of stereotactic apparatus.	6
2.1	One-dimensional illustration of an imperfect frequency encoding.	16
2.2	Pulse sequence for 2D FT multiple slices imaging with spin-echo.	19
3.1	Spatial linearity phantom.	32
3.2	Image distortion in <i>mm</i> at various distances from the isocenter in the caudal direction.	36
3.3	Image distortion in <i>mm</i> at various distances from the isocenter in the cranial direction.	37
3.4	Average distortion at different readout gradient strengths with various phantom cranial positions.	41
3.5	Displacement vector when the frequency and phase encoding gradients are exchanged using a readout bandwidth of $195.3Hz/pxel$	43
3.6	OBT stereotactic frame.	45
3.7	MRI and CT fiducial marker plates.	47
3.8	Phantom for imaging with the stereotactic frame.	50
3.9	Coronal image acquired with the stereotactic phantom.	53
3.10	Fiducial markers distortion in coronal and sagittal subtracted pairs.	54

3.11	Subtraction of transverse images.	57
3.12	Subtraction of the images of a marker plate perpendicular and parallel to the direction of the main field.	58
3.13	Cross section of the fiducial marker plate with acrylic added over one channel.	62
3.14	Subtraction of coronal images with acrylic added over one channel of the top plate.	63
3.15	Error on 3D position with shifted cranial marker position.	65
4.1	Spherical coordinate system.	70
4.2	Typical pulse sequence of the phase encoding technique for distortion correction.	74
5.1	Example of distortion of extent exceeding the limits of the double-gradient distortion correction method.	80
5.2	Input images for distortion correction program.	91
5.3	Processed image from the two input images and absolute subtraction of the processed image with the image acquired at $72.4\text{Hz}/\text{pixel}$	92
5.4	Points used for distance evaluation.	93
5.5	Processed image from two input images reduced to a 6 bits depth and from two input images with a smoothed intensity profile.	96

List of Tables

3.1	Average distortion in <i>mm</i> of the transverse images of the rod phantom at different cranial-caudal positions using various gradient strengths. . .	39
3.2	Resonant frequency of the stereotactic phantom.	52
5.1	Assessment of the efficiency of the algorithm with the help of the original and processed images.	94

Chapter 1

Introduction

1.1 Image distortion

The word "distortion" may be defined as

Twisted out of the true meaning or proportion.

Although the term assumes a wide variety of senses, it is the meaning associated with imaging that will be considered. Image distortion could be seen as the geometrically incorrect representation of the information that the image reflects with respect to what it should be from its actual location in space.

In medical imaging, the subject of interest here, various modalities are used to obtain information related to the human anatomy. In this context, it is a somewhat better approach to clarify the notion of "geometrically incorrect representation" for each one of these modalities. For example, it is found in the technique of projection, used in conventional radiography, such an instance of incorrect representation, namely the magnification of imaged objects and loss of one dimension in positional information. In the same fashion, the latter phenomenon is also involved in computed tomography (CT) due to the finite thickness of the slices that are represented in 2D.

On the other hand, some fluoroscopic images may show a distortion that has a definite pattern such as the so-called s-distortion which makes a cross centered at the image axis appears like a propeller [37]. The fundamental difference between both types of distortion is that the former one is implied in the physics of the acquisition whereas the latter is a characteristic of some part of the imaging system.

In CT, the problem of distortion is generally absent so this modality offers a way to accurately localize structures in space when thin enough slices are used. Nevertheless, its images reflect the attenuation properties towards ionizing radiation. Since this characteristic does not vary much between the different tissues of the brain, this limits its usefulness with tumor boundary localization. Furthermore, it may sometimes be sensitive to artifacts that can affect the image contrast in the vicinity of bony structures. However, nuclear magnetic resonance imaging¹ has long shown its ability to provide good contrast with brain structures. This is due to the fact that the MR image intensity relies on proton density while providing the possibility to weight this intensity with T_1 and T_2 relaxation times. The value of these parameters in tumors was shown to be sometimes different than the one of normal tissues as first reported by Damadian [24].

However, MRI is not free from the problem of distortion which is complicated by the variety of its causes. As chapter 2 will show, the localization of a point in MRI is dependent upon the local magnetic field and the origin of the causes of distortion all amount to modifying this magnetic field in some way. Some or all of these causes may be present at the same time.

Although the search for distortion minimization is in itself a valuable aim, its importance needs to be examined from a clinical point of view. It is generally agreed that the information desired by physicians from diagnostic images is mainly of a qualitative nature, most of the required localization being performed through the knowledge of anatomy. In this context, it appears that the localization performance achieved by

¹The "N" will generally be dropped in deference to the now dominant use of the expression MR imaging or MRI to designate this imaging technique, but it will be conserved when referring to the NMR physical phenomenon

present systems is generally acceptable for the purpose of diagnostic radiology. On the other hand, some recent advances require a greater geometrical integrity than the one generally available with present MR images. Correlative imaging, which consists of combining images from various imaging modalities has shown some promising results [31,70,80,125]. But more than everything else, the increasing popularity of *stereotaxy* is the strongest motivator for obtaining accurate MR images [35,82,94,95]. In many cases, this class of methods calls for submillimeter image accuracy. As stereotaxy will dictate many of the considerations that will be further enounced, it is appropriate to study it in greater detail.

1.2 Stereotaxy

1.2.1 Development of Stereotaxy

Stereotaxy is the methodology involving the use of a reference frame to localize in a reproducible fashion anatomical structures in terms of coordinates inherent to that frame and to support instruments to be used to reach a target localized in this manner. This reference frame therefore needs to be anchored to the patient's head. Although stereotactic methods ² began to achieve an extensive popularity with the arrival of CT and MRI, the concept was first exploited in the late 19th century. An anatomy mounted device used as an instrument support was reported by Dittmar in Germany in 1873 [26]. In 1890, the Russian anatomist Zernov reported and used a few times an instrument which went further by involving a polar coordinate system to describe the position of the targets to be reached [124].

²Despite the previous use of the noun stereotaxy, the adjective stereotactic in contrast with stereotaxic will be used to qualify the corresponding methods and to follow the now established convention. Even if both terms share the common root stereo from the Greek word "stereos" which means "three-dimensional", the suffix "tactic" from "tangere" (to touch, latin) was recognized more appropriate than "taxy" ("taxis", greek for system) in representing the nature of the technique.

The first report of exhaustive development and trial of the stereotactic methodology is commonly credited to Horsley and Clarke. In 1908, they published a paper describing a study of the cerebellum by using a frame mounted on experimental animals to support a device intended to create some lesion within the brain in a very precise manner [48]. This mounted device had to be moved in such a way that any point within a target volume could be reached. Their work yielded the first stereotactic brain atlas. In 1918, Mussen, a physiologist, had a similar apparatus modified for use with humans but was unsuccessful in convincing neurosurgeons to use this first human stereotactic device [97].

Hence, it is probably in 1947 in Philadelphia that Spiegel and Wycis carried out the first clinical trial of a stereotactic device [111]. Their apparatus was of the translational type, thus called since it allowed motion of a mounted operative device in a single plane. They successfully eliminated the problem of brain anatomy variability in humans with respect to cranial landmarks (used by Horsley and Clarke to locate subcortical structures with animals) by using ventriculography, a technique that allowed radiographic visualization of the ventricular system, thus providing a landmark which was more representative of the brain anatomy. An electrode could then be lowered to the target, but its angulation relative to the bearing device could not be modified. Another early device consisted of an electrode holder fixed to the skull with a single burr hole through which the probe was to be inserted [73]. However, the use of a single attachment point made it rather unstable and the absence of a frame on which to fix the device still only allowed a unique trajectory to the target once it was in place.

The work of Spiegel and Wycis had drawn the attention of a Swedish neurosurgeon, Lars Leksell. In 1947, Leksell left Philadelphia inspired by the American's stereotactic technique and returned to Stockholm where he started the development of his own apparatus. In 1949, Leksell described his new stereotactic frame [66] and the appropriateness of the original concept explains why many of today's devices are derived from Leksell's first model [67,68,69,91,92,116]. Basically, his system consisted of an arc supported by a frame attached to the patient's head. This arc could be displaced so that the position of its center would correspond to the site of the target to be reached with a needle

or electrode placed perpendicularly to the arc and pushed down to the target. As the needle could be moved along the arc and this arc rotated about an axis running through its center (so through the target), there was no longer one sole choice for the path of penetration once the frame was in position. This frame was the first instance of the so-called arc type.

Many devices were developed following this but most of them belong to one or another of the categories illustrated in Fig. 1.1. The types A and C respectively correspond to the Spiegel-Wycis and the single burr hole models previously mentioned, but the vast majority of contemporary models are of type B or D, respectively the arc-quadrant type and general arc type. In the systems of type B, the target is placed at the center of the arc by either allowing this arc to move as in the Leksell concept [68,69] or by adjusting the patients head thus yielding the same result as in the Todd-Wells system [116]. An instance of the second case is the Riechert-Mundinger system for which the stereotactic apparatus adjustment required for correct aiming is found by phantom simulation from the target position obtained from radiographs [7,103]. A somewhat different instrument was developed by Talairach in France and relies for localization on the probe holder itself to be visualized with the help of radiographs obtained with a large tube-object distance ($\sim 6\text{m}$) to minimize the magnification effect [113]. In the sixties, stereotactic procedures were mainly indicated for movement disorders. The introduction of L-dopa for treatment of Parkinson's disease in 1968 triggered a fast decline of stereotaxy during the few following years until new advances reversed this tendency by expanding the list of indications beyond functional neurosurgery.

1.2.2 Modern stereotaxy

Clarke had already considered the possible use of his method for the treatment of deep-seated brain tumors with an eventual human stereotactic frame that he never built [21]. Soon after the first instances of human stereotaxy, Talairach started exploring the possibilities of tumor treatment using interstitial implantation of radioactive sources [112].

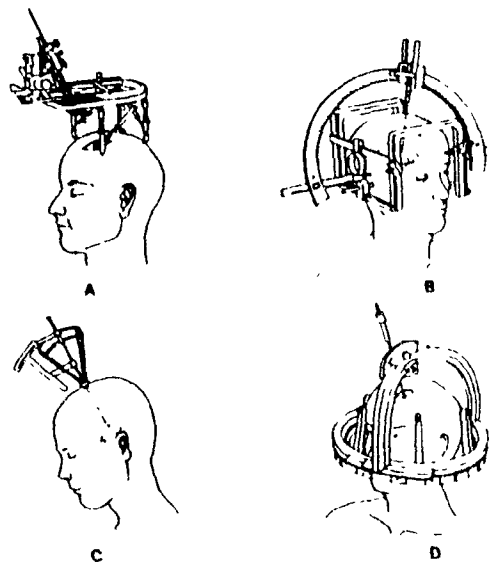


Figure 1.1: Illustration of 4 basic types of stereotactic apparatus. (A) Spiegel-Wycis model. (B) Arc-quadrant type. (C) Single burr hole mounted device. (D) General arc type. Reprinted with permission from PL Gildenberg: Functional neurosurgery, in *Operative Neurosurgery* by Schmidek H and Sweet H (eds). Grune & Stratton, New York 1987.

This was the beginning of tumor stereotaxy but for many years, implants remained the only instance of stereotactic radiotherapy. The introduction of the still used “Leksell Gamma Knife” by Leksell in 1971 was the first definite instance of *radiosurgery*, a non-invasive irradiation of the brain with the help of stereotaxy [67].

The last version of the Gamma Knife consists of 201 ^{60}Co sources placed in a hollow lead sphere. The γ emission of those collimated sources is focussed on a central point within the sphere which is provided with a shielded shutter allowing the head of the patient to be introduced inside for irradiation, the target being placed at the focus point by the appropriate adjustment of a dedicated stereotactic frame. The radiation dose distribution thus obtained shows a fast falloff around the target and despite the original

of the gamma knife solution is rarely denied, the amount involved in launching such a specialized unit ($\sim \$ 3\,000\,000$) is by far out of range for the budget of most institutions. This has motivated studies for adapting existing radiotherapy apparatus, generally linear accelerators (linac), to be used for stereotactic irradiation. By now, many linac based radiosurgery systems have been successfully developed and often show performance comparable to gamma units [98,99,100,118]. In any case, all these radiosurgical techniques call for localization accuracy better than 1mm.

However, the major contributor to the revival of stereotaxy is probably computed tomography, attributable to Hounsfield [49]. This changed completely the perspectives in stereotaxy by providing geometrically accurate images to the physician who were then able to detect deep-seated brain lesion in its early stages from CT slices. At present, most stereotactic systems allow position calculation using a system of fiducial markers of known geometry that can be visualized with a CT image. In the last few years, the most common stereotactic neurological procedure was CT-aided biopsy, but many new applications are considered [53].

Closely following CT, the introduction of MRI constituted another major step in the field of stereotaxy. The methodology of adapting existing systems to MRI was basically the same as for CT, except that ferrous materials were to be eliminated. This is due to the high susceptibility of these materials which would make their introduction in a MR imager hazardous from the magnetic attraction exerted on them, as well as to the fact that they would create overwhelming magnetic field disturbances making imaging virtually impossible. This proscribed the use of many initial versions of the various apparatus. However, as previously mentioned, its ability to reflect proton density (essentially water molecules density) weighted in a controllable way by molecular parameters is of great interest, especially in tumor detection. Newly developed systems such as the Brown-Robert-Wells and the Olivier-Bertrand-Tipal used for some of the experiments of this work take advantage of the possibilities offered by both CT and MRI [13,88,89,91].

Future trends are likely to include a growing effort toward oncological applications relying primarily on CT, and also on MRI provided that ways to obtain geometrically accurate images with this modality are found. Radiosurgery using linacs is certainly going to improve even further. One possible avenue for this is the exploitation, during irradiation, of all degrees of freedom that modern machines provide in order to tailor the dose distribution to better fit the target [109]. This again will call for distortion free MR images in order to provide the accuracy needed to make it possible. On the planning side, there is little doubt that 3D visualization will take over in the planning room [12], probably along with multi-modality image integration [44]. Ultrasonography might be seen shortly as part of this set of modality. Concerning the stereotactic apparatus, most development will conceivably be carried out in the direction of a non-invasive frame [39] or even a frameless approach for image acquisition using superficial landmarks on the patient's surface to allow the stereotactic coordinate system to be rebuilt [46,58,105]

1.3 Objectives

MRI will certainly continue to achieve a continuous development in the next few years. Fast imaging techniques, particularly, will improve the performance with regards to imaging times. It is therefore probable that image accuracy becomes a constraint that is called for more and more frequently. In the light of this, the objectives of this work can be stated by the following.

1. To study the problem of geometrical image distortion in MRI whose main causes are:
 - Non-uniform magnetic susceptibility of the imaged material.
 - Main magnetic field inhomogeneity.
 - Magnetic gradient field non-linearity.
 - Non-uniform chemical shift of the nuclear species undergoing NMR.

- Transient currents induced by the magnetic gradients switching.
2. To evaluate some aspects of MR image distortion related to a current stereotactic methodology.
 3. To examine in a general fashion the avenues of distortion correction, and to assess the efficiency of one recent technique of performing such a correction.

Chapter 2

Theory and principles

2.1 Nuclear magnetic resonance

In physics, resonance is defined as the phenomenon by which a system absorbs energy with a certain characteristic frequency, the *resonant frequency*. This frequency is dependent upon the nature of the system being considered. It is only in 1946 that Bloch and Purcell independently demonstrated a resonance phenomenon for a population of nuclear spins in response to a magnetic field oscillating at radio frequency (RF) [8,9,101]. This phenomenon was therefore called nuclear magnetic resonance, or NMR.

At the basis of NMR is a quantum mechanical property shown by some particles, the angular momentum L (or spin) generally measured in units of h . Protons and neutrons (nucleons) possess this property, and some nuclei have it as well provided that they have an odd number of nucleons. This is the first basic consideration that dictates which nuclei can demonstrate NMR properties. This, along with the concentration of the nuclear species in the human body and its energy absorptivity toward the RF field, restrains the possible choices for NMR studies with humans to ^1H (by far the most used nucleus for this purpose from its presence in water), ^{13}C , ^{19}F , ^{23}Na and ^{31}P .

¹Bold faced characters express vectorial quantities while the ordinary font represents the modulus of this same quantity.

The presence of a non-zero angular momentum involves a certain magnetic moment μ parallel to it. This magnetic moment can be expressed by

$$\mu = \gamma \hbar L \quad (2.1)$$

where γ is the gyromagnetic ratio and \hbar is the Planck constant h divided by 2π . The potential energy when a magnetic field B is present, is given by

$$U = -\mu \cdot B. \quad (2.2)$$

When B lies along the z axis, the component of the angular momentum in this direction is quantized according to $L_z = L, L - 1, \dots, -L$. Assuming some incoming energy of frequency ω such that $U = \hbar\omega$, the well known Larmor formula is obtained for a transition between the two possible energy states of a single proton (hydrogen), $L_z = 1/2$ and $L_z = -1/2$, by equating Eq. 2.2 with $\hbar\omega$ and replacing μ using Eq. 2.1 [62,85].

$$\omega = \gamma B \quad (2.3)$$

Eq. 2.3 represents the frequency required to induce a transition and is the fundamental condition for magnetic resonance. Moreover, a particle having a non-zero magnetic moment precesses about the direction of the magnetic field and Eq. 2.3 represents the frequency of this precession.

It is known that the rate of variation of the angular momentum of a system is proportional to the torque acting on it. Since the torque acting on a magnetic moment μ in a magnetic field B is $\mu \times B$, one can write using Eq. 2.1

$$\frac{d\mu}{dt} = \gamma \mu \times B. \quad (2.4)$$

For a unit volume, the magnetization M is given by $\sum \mu_i$, and Eq. 2.4 can be rewritten

$$\frac{dM}{dt} = \gamma M \times B \quad (2.5)$$

² $\gamma = 2.675 \times 10^8 s^{-1} T^{-1}$ for the proton whereas $h = 6.626 \times 10^{-34} J \cdot T$.

for an inertial frame of reference xyz . Although Section 2.3 will treat this in greater detail, it is now supposed that M is non-zero. Assuming a cartesian frame of reference $x_1y_1z_1$ rotating about its z_1 axis at frequency Ω and having the same origin as xyz , Eq. 2.5 can be rewritten. It can be proven that the new description of the system is similar to the initial one if a fictitious magnetic field component Ω/γ opposite in sign with B is introduced [85]. Hence, the effective field in the rotating frame is made zero provided that

$$\Omega = \gamma B. \quad (2.6)$$

Eq. 2.6 reveals the essence of NMR excitation. With a spin system placed in a magnetic field B , the effect of a magnetic field of amplitude B_1 oscillating at RF frequency and oriented perpendicularly to z can be seen as the result of 2 circularly polarized fields rotating in opposite senses. If the frequency of this oscillation is given by Eq. 2.6, the only remaining static magnetic field present is in the x_1y_1 plane and is attributed to the influence of one of the two polarized fields. The second circularly polarized field is neglected since it has no resulting effect.

Following the application of a RF pulse of duration t_a , the magnetization as seen in the rotating frame will then be tipped by an angle θ given by

$$\theta = \gamma B_1 t_a. \quad (2.7)$$

from Eq. 2.3. Upon completion of this excitation, the magnetization as seen in the inertial frame will no longer be at equilibrium and will start to precess about the direction of B . The excitation is provided by applying a time varying magnetic field perpendicularly to B , thus in the xy plane, at a frequency given by Eq. 2.3. The precessing magnetization can then induce a signal in a coil whose axis is also placed in the xy plane so that it sees a time varying magnetic flux. Often, a single coil is used for both transmitting and receiving.

Implied in Eq. 2.5 is the assumption of a precession movement about the direction of B that is not dampened. In reality, this is not adequate and Eq. 2.5 has to be

modified so that it accounts for damping. In order to do that, one may use the following assumptions:

1. The time variation of the z (longitudinal ³) component of the magnetization is proportional and opposite to its departure from equilibrium.
2. The time variation of the transverse ³ component of the magnetization is proportional and opposite to its size.

The above proportionalities apply respectively with exponential time constants T_1 and T_2 . T_1 is termed spin-lattice relaxation time as its presence implies a change in the total magnetization of the population of spins, supposedly brought about by the presence of a "lattice" which makes it possible for the population to exchange energy with the environment and thereby modify its total magnetization. T_2 represents the increasing dephasing of the transverse magnetization implied by an appropriate tipping pulse in a homogeneous magnetic field. It is called spin-spin relaxation time [114].

This yields Eqs. 2.8, 2.9 and 2.10, or the Bloch equations describing the time evolution of each component of the magnetization outside of equilibrium [8].

$$\frac{dM_z}{dt} = \frac{M_0 - M_z}{T_1} \quad (2.8)$$

$$\frac{dM_x}{dt} = \gamma(\mathbf{M} \times \mathbf{B})_x - \frac{M_x}{T_2} \quad (2.9)$$

$$\frac{dM_y}{dt} = \gamma(\mathbf{M} \times \mathbf{B})_y - \frac{M_y}{T_2} \quad (2.10)$$

M_0 represents the size of the magnetization at equilibrium. If B_1 and t_a in Eq. 2.7 are such that $\theta = 90^\circ$, then Eq. 2.8 can be integrated to yield the expression of the longitudinal magnetization as a function of time

$$M_z(t) = M_0 [1 - \exp(-t/T_1)] \quad (2.11)$$

³Longitudinal and transverse express the direction of \mathbf{M} with respect to \mathbf{B} .

where $t = 0$ corresponds to the 90° pulse. Likewise, the transverse magnetization is obtained by integrating and combining Eqs. 2.9 and 2.10 to yield the expression of the transverse magnetization.

$$M_x(t) = M_0 \exp(-t/T_2) \cos(\omega t) \quad (2.12)$$

$$M_y(t) = M_0 \exp(-t/T_2) \sin(\omega t) \quad (2.13)$$

2.2 Magnetic Resonance Imaging

2.2.1 Introduction

In 1973, Lauterbur reported some results concerning a new imaging method using NMR [65]. His *back projection reconstruction* technique used along with the main magnetic field some magnetic gradient fields in order to spatially encode the NMR signal, this yielding some projections of the object. The image was then reconstructed using a back projection method similar to typical CT reconstruction schemes [57]. MRI with a different method, zeugmatography, was also reported by Kumar in 1975 [63]. Most of today's techniques use either a derivation from Kumar's method, the *spin-warp* method [29] or an extension of the latter with multiple excitations of the whole volume [25].

Practically all of MR imaging methods can be classified in one of the following categories which describe the nature of the element excited at any one cycle [55].

Point. One single *voxel*, or the most elementary volume to be analyzed, is interrogated by applying oscillating magnetic gradients that allow excitation and reading on an individual voxel basis [45]. The method is very inefficient from the point of view of the signal-to-noise ratio (SNR) ⁴.

Line Extension of the former method to the excitation of one column at a time. Like its point counterpart, it has a poor SNR efficiency [78].

⁴The SNR is the ratio of the signal and noise voltages

Planar Routinely used in MR imaging. The selected plane or more commonly *slice* can be encoded using various schemes such as the spin-warp method, or more rarely Lauterbur's projection reconstruction. Interest has also been shown about another method of encoding a selected slice, the echo-planar technique which requires only one cycle [79].

Volume The signal acquired with volume methods contains some information about the whole volume to be imaged. The 3D spin-warp method is used to accomplish that.

2.2.2 Imaging in non-ideal conditions

Imaging using NMR relies on the use of one or two RF frequency antennae in conjunction with magnetic gradient coils (or simply magnetic gradients) providing a space variant contribution to the total magnetic field. The scheme determining the switching on or off of these elements during the imaging process is referred to as a *pulse sequence*. Even though the general expression for a magnetic gradient involves a second rank tensor, its effect in a large static field along the z direction⁵ is well characterized by the 3 partial derivatives $\partial B_z/\partial x$, $\partial B_z/\partial y$ and $\partial B_z/\partial z$. To each of these components corresponds a generating gradient coil that is saddle-shaped in the first and second cases and cylindrically symmetric in the third [115]. The subscript z can be omitted.

Considering the situation depicted by the dotted line of Fig. 2.1, it is seen that if a magnetic gradient $G_x = \partial B/\partial x$ is applied, the resonant frequency at position x of an excited sample can be described with

$$\omega(x) = \gamma(B_0 + xG_x) \quad (2.14)$$

where B_0 is the nominal size of the imager main magnetic field. Eq. 2.14 follows from

⁵Following the general convention, the cartesian coordinates xyz will be used to describe the imager space whose origin corresponds to the center of the magnet. z is the direction of the main magnetic field (between 0.1 and 4.0T in imaging) which is assumed to lie along the bore axis.

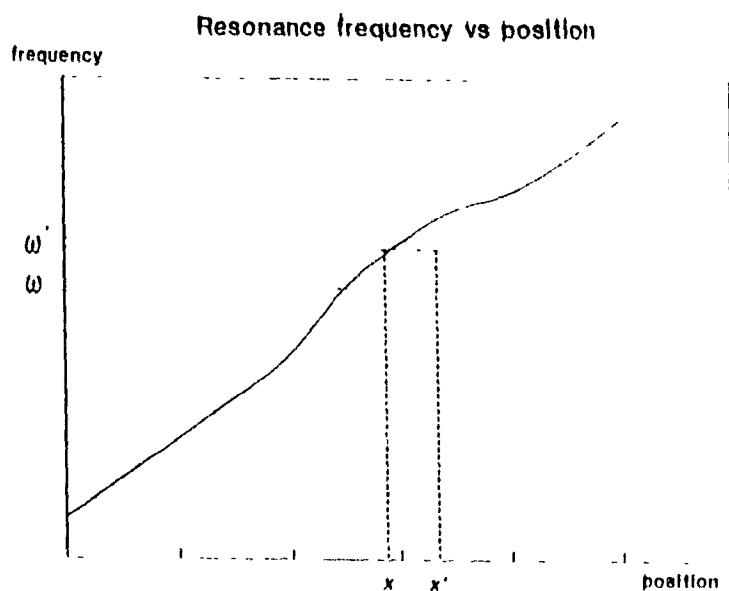


Figure 2.1: Representation of frequency encoding in non-ideal conditions (continuous line), that is using a non-linear gradient and an inhomogeneous static field compared to ideal conditions (dotted line).

Eq. 2.3.

However, if the static field is inhomogeneous and the gradient field is non-linear, Eq. 2.14 has to be rewritten as

$$\omega'(x) = \gamma(B_0 + \Delta B(x) + xG_x + \Delta G_x(x)) \quad (2.15)$$

since it is the frequency ω' rather than ω that will be emitted from a point situated at x . $\Delta B(x, y, z)$ is the deviation of the static field from homogeneity while $\Delta G_x(x)$ is the deviation of the gradient from linearity *at a given gradient strength*. When the gradient strength is modified, $\Delta G_x(x)$ will be modified in the same proportion. The next step is to detect the emitted signal and to associate a position x with each frequency ω' . The situation expected from Eq. 2.14 would falsely yield a position x' . However, the actual emission occurs at x which is related to x' by equating Eq. 2.15 with Eq. 2.14, the latter

carrying the expected x' rather than x . This gives Eq. 2.16.

$$x' = x + \frac{\Delta B(x) + \Delta G_x(x)}{G_x} \quad (2.16)$$

However, it shall be assumed that the gradients (readout or other) are perfectly linear over the region of interest, thus not contributing to the image distortion. This assumption will be further discussed in the next chapter.

If a coil is placed about the excited sample, the latter's bulk magnetization produces a time varying magnetic flux through it, and a voltage with the same frequency characteristics is produced. Since the above situation implies the presence of a finite NMR frequency band, the induced signal will be the sum of all frequencies present within the extent of the sample in the x direction. In practice, much lower frequencies are measured as the picked-up signal undergoes quadrature phase-sensitive detection, which implies filtering out the high frequency component.

In order to obtain a profile of the spin density, one can acquire this filtered signal and apply a Fourier transformation which allows the frequencies present to be separated. This profile is obtained along the x direction, also called the *frequency encoding* or *readout* direction. To acquire a full 2D spin density map, the already mentioned back projection reconstruction technique carries out many of these profiles in various directions as determined by the sum of 2 gradients applied perpendicularly to each other [65].

However, the spin-warp method introduced by Edelstein handles that problem by preceding the application of the readout gradient by another gradient in a perpendicular direction [29]. Following the application during a period τ_y of this gradient of strength G_y , a linear gradient $\gamma\tau_y G_y$ is imposed on the phase in the direction of application of this *phase encoding* or *preparation* gradient. The procedure is repeated every TR⁶, $2m$ times with different gradients of strength $\pm mG_y$ preceding as many readout gradient applications (generally m possible preparation strengths at both polarities where one generally has $m = 128$).

⁶The length of one cycle (also called view) is the *repetition time* (TR)

The extension of the methodology described above to 3D is straightforward. It was assumed previously that an already excited sample was to be imaged in two dimensions. However, Eq. 2.14 may be used to describe the way one *excites* a sample rather than receives its signal. This is at the basis of the *slice selection* technique which consists of applying an RF pulse of a certain frequency bandwidth (a truncated sine function in time domain) along with a gradient. The absorption of this RF pulse is confined to the slice of material that fulfills Eq. 2.3. This slice can then be encoded using a 2D method. When the slice is 2D encoded using the spin-warp method, the scheme is called 2D FT multiple slices acquisition and Fig. 2.2 illustrates the pulse sequence used to perform it.

As before, it is Eq. 2.15 instead of Eq. 2.14 that applies and this has as a consequence that the excited slice is non-planar, having a deviation in the slice selection direction described by Eq. 2.16 [72]. Once the slice is excited, a 2D method may be used to encode the image. As a slice has to be made thin enough to avoid too much blurring due to depth averaging of the 2D representation, a series or stack of such slices is generally desired. In order to reduce the time inherent to such a type of acquisition, one can use the delay between 2 views of the same slice to perform one or many views on other slices. This may in some cases reduce considerably the time required to measure a complete volume.

In Fig. 2.2, the applications of the x and z gradients closely following the 90° pulse are respectively intended to counteract the z dephasing due to the slice selection gradient and to ensure that the x dephasing will be eliminated in the middle of the data acquisition. If not compensated, this dephasing could inhibit the acquisition of any useful signal.

However, Fig. 2.2 shows the presence of a supplementary pulse prior to reading. This is the *echo* pulse which is applied at a time $TE/2$ where TE is the time between the 90° pulse and the echo. Its presence is due to the fact that the actual transverse relaxation time in a system where the static magnetic field is inhomogeneous is not T_2 , but a much shorter time called T_2^* since these inhomogeneities also contribute to the dephasing of

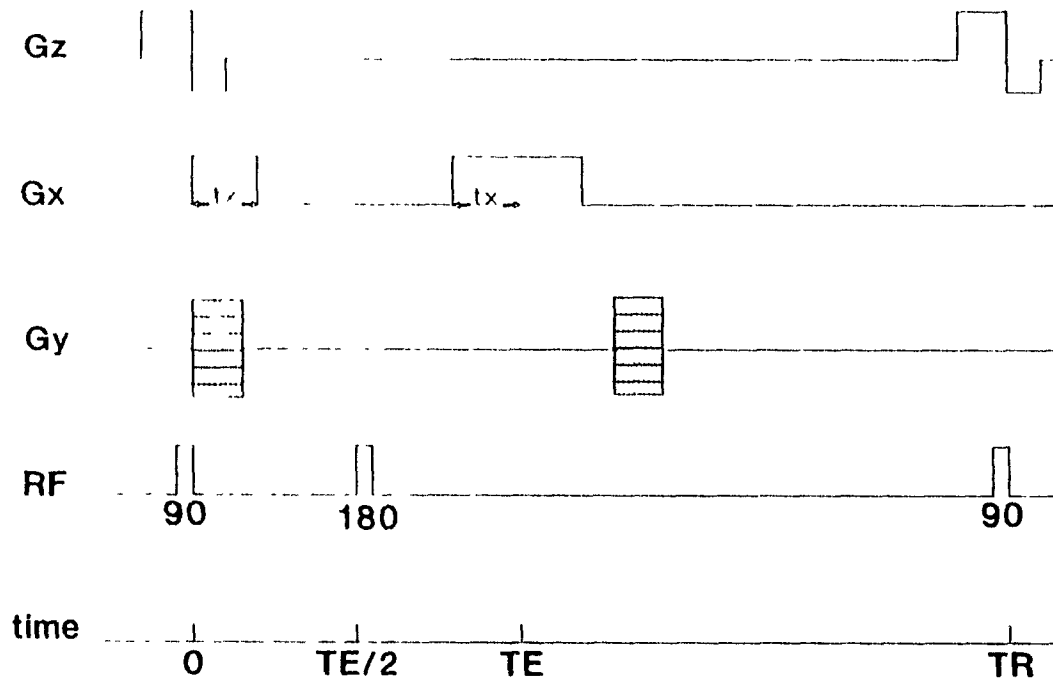


Figure 2 2: Pulse sequence used with 2D multiple slices spin-echo imaging. The z direction is used for slice selection whereas the x and y directions correspond respectively to the frequency and phase encodings. Note that the origin of the time axis is chosen as $t = 0$.

the transverse magnetization. Nevertheless, their effect is reproducible and inverting the magnetization using a 180° pulse after a time $TE/2$ following the initial 90° pulse causes the transverse magnetization of the system to reach a maximum TE after the 90° pulse application since the effects of the dephasing due to field inhomogeneities temporarily cancel out [15,38,81]. Thus, only T_2 will contribute to the decay of the signal acquired after a time TE . A gradient echo sequence where such a 180° rephasing pulse is present is called spin-echo.

Assuming an ideally selected slice and ignoring relaxation effects, the demodulated signal $S(t)$ (also called FID for free induction decay) after preparation and during the time t such that $0 \leq t < TE/2$ is satisfied is described by

$$S(t) = C \int \int \sigma(x, y) \exp [i\gamma(\Delta B(x, y)t + ymG_y\tau_y + xG_x t_x)] dx dy. \quad (2.17)$$

$\sigma(x, y)$ represents the 2D spin distribution and C is a constant. At $TE/2$, a 180° pulse is applied. At $TE-t_x$, the readout gradient is again turned on and the acquisition resumes. It is then terminated at $TE+t_x$. During this period, the signal takes the form [60]

$$S(t) = -C \int \int \sigma(x, y) \exp [i\gamma(\Delta B(x, y) + xG_x)(t - TE) - ymG_y\tau_y] dx dy. \quad (2.18)$$

One can introduce a term $k_y = -\gamma m G_y \tau_y$ along with $k_x = \gamma G_x (t - TE)$. Moreover, it is convenient to define a new variable x' such that

$$x = x' - \frac{\Delta B(x, y)}{G_x} \quad (2.19)$$

and introduce it in Eq. 2.18 along with the Jacobian of this coordinate transformation

$$J(x', y) = \frac{dx'}{dx}. \quad (2.20)$$

This yields

$$S(k_x, k_y) = -C \int \int \sigma(x, y) \exp [i(x'k_x + yk_y)] [J(x', y)]^{-1} dx' dy. \quad (2.21)$$

where $S(k_x, k_y)$ is used to denote the set of signals obtained with different phase encoding gradient strengths mG_y . The application of a Fourier transform (FT) allows

to obtain the final image from the signal $S(k_x, k_y)$ [11,96]. Nevertheless, conventional reconstruction algorithms ignore the presence of a term $\Delta B(x, y)$ and yield a distorted density $\sigma'(x, y)$ that is related to the true density by

$$\sigma'(x', y) = \sigma(x, y)/J(x', y). \quad (2.22)$$

The signal $S(k_x, k_y)$ is sampled at many discrete points. The number of cycles needed to acquire an image depends on the number of preparation gradients (and slice selections) used, but is generally 256. The reconstruction process is numerically implemented using the fast Fourier transform (FFT) [6].

Fundamental is the fact that Eq. 2.22 implies the immunity of the phase encoding direction in the face of static field errors expressed by $\Delta B(x, y) \neq 0$. With spin-echo methods, this comes from the fact that the dephasing caused by these reproducible types of field errors cancel out at $t = TE$ along with the dephasing due to the readout gradient. When no such 180° echo pulse is present as in gradient-echo images, the reconstructed density carries a phase error. However, no distortion effect along the preparation direction is present with modulus images.

This feature of the spin-warp method is an improvement over the original Kumar's "Zeugmatography" in which the scanning of k -space⁷ in the y direction was accomplished with the help of a phase encoding gradient applied at fixed strength during a different time for each view [29,63]. This implied that the time between excitation and acquisition had to be varied, thereby defeating the independence of the phase perturbation toward k_y and the immunity of the phase encoding direction against static field errors.

One further interesting element is that the point spread function inherent to the spin-warp method is not degraded by the presence of main field inhomogeneity but is merely shifted in position [87]. The recovery of distorted spin-warp images is consequently easier

⁷The so-called k -space representation is simply a way to formalize the introduction of the k_x and k_y terms as dimensions of a 2D space which is the Fourier domain counterpart of the image to be reconstructed.

than the one of projection reconstruction images since the latter undergoes degradation in shape from the presence of $\Delta B(x, y)$. Furthermore, Lai [64] showed that the loss of information due to this degradation is recoverable only prior to reconstruction.

Another technique to perform volume encoding is the 3D FT method. The description of the reconstruction performed with this scheme is similar to the 2D version except that the former slice selection gradient is replaced by a second phase encoding gradient. Hence, the signal acquired with this method is given by

$$S(k_x, k_y, k_z) = -C \int \int \int \rho(x, y, z) \exp [i(x'k_x + yk_y + zk_z)] [J(x', y, z)]^{-1} dx' dy dz. \quad (2.23)$$

with $k_z = -\gamma n G_z \tau_z$. The reconstructed three dimensional density of spin $\rho(x, y, z)$ is obtained through the application of the 3D FT, thus yielding

$$\rho'(x', y, z) = \rho(x, y, z) / J(x', y, z). \quad (2.24)$$

Again, the absence of distortion along both phase encoding directions allows one to describe the Jacobian of the transformation with $J(x', y, z) = dx'/dx$. This can be compared advantageously with 2D FT multiple slices acquisition where the excited slice is non-planar from the presence of these distortions.

The use of different TR's and TE's allows one to weight the relative contributions of T_1 and T_2 in the final image from Eqs. 2.12, 2.13 and 2.11. Finally, note that the slice selection performed with the 180° echo pulse needs no compensation as its application is shared evenly between the moments preceding and following the 180° pulse.

2.3 Signal-to-noise ratio

In NMR, the received signal depends upon the presence of a non-zero equilibrium magnetization in the sample. Assuming that the magnetic field has a size given by B_0 , a nucleus of spin $1/2$ has 2 energy states given by Eq. 2.2, that is μB_0 and $-\mu B_0$. Those 2 states correspond to a magnetic moment and a magnetic field being respectively antiparallel ($N_{\uparrow\downarrow}$) and parallel ($N_{\downarrow\uparrow}$) to each other. The relative occupancies of these 2 energy

states in a population of N such nuclei can be described by a Boltzmann distribution [62]. The resultant magnetization is obtained by using the approximation $\mu B_0/\kappa T \ll 1$, where κ is the Boltzmann constant and T represents the temperature. One can then write

$$N_{\uparrow\uparrow} - N_{\uparrow\downarrow} = N \tanh\left(\frac{\mu B_0}{\kappa T}\right) \cong \frac{N\mu B_0}{\kappa T}. \quad (2.25)$$

In MRI, T is obviously not an available parameter. Consequently, only B_0 is provided to influence the magnetization of a given population.

However, increasing the field strength also has some other consequences. Since it is reasonable to assume that the relative magnet homogeneity⁸ varies little with the field strength considered [40], the strength of the readout gradient has to be increased in proportion to the field strength in order to keep the difference $x' - x$ constant in Eq. 2.16.

Now, Brownian motion of the electrons in both the sample and RF system implies the presence of a randomly fluctuating voltage between any 2 points situated in one of these resistive media. This creates the so-called Johnson noise which can be characterized using the Nyquist formula expressing the root mean square of this voltage fluctuation as

$$V = (4\kappa TR\Delta\nu)^{1/2}. \quad (2.26)$$

In Eq. 2.26, $\Delta\nu$ represents the frequency bandwidth of the receiving system and R the electrical resistance between the measuring points. At high frequencies, Johnson noise in the sample dominates. However, the use of lower field strengths increases the relative importance of the noise in the coil which then complicates its design [28]. At high frequencies such as the ones employed in MRI, RF attenuation in the patient can be of some importance with regards to SNR, but Johnson noise alone generally constitutes a reasonable approximation [28].

⁸The most common way to characterize this feature of a magnet is the use of a relative unit, the *ppm* or parts per million. The homogeneity is expressed for a given volume centered about the center of the magnet (isocenter) and represents the largest field deviation between 2 any points within that volume divided by the nominal static field strength and multiplied by 10^6 .

This noise voltage will be added to the one induced by the fluctuating magnetization, thereby degrading the image. One can then write about the signal-to-noise ratio that $\text{SNR} \propto (\Delta\nu)^{1/2}$ [71]. This important result shows that the discrepancy between x' and x from the presence of $\Delta B(x)$ in Eq. 2.16 is minimized at the cost of the SNR.

Expressions for the relative efficiency of 2D FT and 3D FT techniques in terms of SNR, respectively for SNR_{2D} and SNR_{3D} , are obtained from Eq. 2.26 and the derivations of Bradley [12] as

$$\text{SNR}_{2D} \propto \rho w_x w_y w_z \left[\frac{r N_x N_y}{4\kappa T R \Delta\nu} \right]^{1/2} \quad (2.27)$$

and

$$\text{SNR}_{3D} \propto \rho w_x w_y w_z \left[\frac{r N_x N_y N_z}{4\kappa T R \Delta\nu} \right]^{1/2} \quad (2.28)$$

In Eqs. 2.27 and 2.28, ρ represents the effective spin density, $w_{\text{direction}}$ represents the voxel dimension, r the number of signal averages and $N_{\text{direction}}$ the number of gradient encodings or the dimensions of the k -space.

It is seen that the SNR depends directly on the voxel volume. This contrasts somewhat with other imaging modalities where the behavior of noise is directed by Poisson statistics and implies a dependence on the square root of the voxel volume. Also, there is nothing analogous to the dependence on radiation dose as B_1 is not present in the above expressions [28]. Considering the efficiency figure of merit η used by Parker [90] and given by $\eta = \text{SNR}/\sqrt{t}$, it can be seen that interleaving can totally compensate for the apparent SNR advantage of 3D FT by dividing the 2D FT imaging time t by a factor of up to N_z (as for N_z excitations per TR).

2.4 Magnetic susceptibility and chemical shift effect

Magnetic susceptibility is a phenomenon by which an external source of magnetic field magnetizes a material, or creates some magnetic moments at the atomic level. The local magnetic field is therefore different than what it would be if the outside field source were the only one contributing to the overall magnetic field.

Literature in MRI and MRS ⁹ often deceptively attributes the origin of the NMR phenomenon to a "magnetic field" H ¹⁰ rather than B . This may cause one to forget about a basic aspect of NMR, that is that the value of the magnetic field reflected by ω includes a certain susceptibility contribution to B that is proportional to it. Nonetheless, both spectroscopy and imaging are intended to detect a *difference* in resonant frequency, so that susceptibility is of little concern as long as its contribution is homogeneous throughout the studied volume.

In MRS, this difference is due to the *chemical shift* of molecules. This is more or less a type of molecular susceptibility effect that is seen as the difference in resonant frequency of the same atom hosted by different molecules. As with susceptibility, its contribution to B is proportional to the bias field. A typical instance of such an effect is seen with the 2 most common hydrogen compounds in the human body, water and fat (the latter's contribution mainly comes from the $-CH_2-$ segment) where a difference of resonant frequency of about $3.3ppm$ is seen.

Since the importance of the susceptibility and chemical shift effects only depends upon the magnetic field and that the latter is constant in time (neglecting the gradient switching that represents less than 1% of the total field), the susceptibility effect can be assimilated into the earlier $\Delta B(x, y, z)$ term along with main field inhomogeneity and chemical shift. Hence, the knowledge of the overall $\Delta B(x, y, z)$ effectively indicates the distortion from these 3 causes, whatever their respective contribution is. This knowledge is obviously patient dependent to the extent that susceptibility and chemical shift effects are present.

One can distinguish between many types of susceptibility.

diamagnetism Diamagnetism is classically described as a change in the orbital velocity of the electrons from the action of the component of the magnetic field along the

⁹Magnetic Resonance Spectroscopy.

¹⁰The origin of the field H often called magnetic intensity lies in the presence of a current density J distribution in the vicinity of the point considered and excludes susceptibility effects.

axis of the orbit. The resulting field from that contribution is typically $10^{-6} \times B$ and always opposed to the main field. Diamagnetism alone determines the susceptibility if the total angular momentum \mathbf{J} of the molecule is zero

paramagnetism If however \mathbf{J} is not zero, the diamagnetism is generally dominated by the paramagnetism whose effect in terms of magnetization is in the direction of \mathbf{B} and of magnitude 10^{-4} to $10^{-6} \times B$.

ferromagnetism Just like paramagnetic materials, ferromagnetic substances also cause the presence of magnetization in the same direction as \mathbf{B} , but with a much greater magnitude. Ferromagnetic impurities in a material may considerably affect this material's magnetic properties.

In MRI, the field variation due to magnetic gradients over a field of view of 50cm is more than $10^{-4} \times B_0$, which allows one to conclude that diamagnetic effects are generally not the source of large geometrical distortion. However, they may be more important when using gradient echo imaging techniques by modification of T_2^* relaxation time to which these methods are sensitive [23,75]. Paramagnetism and ferromagnetism are much more likely to cause geometrical distortion. Such artifacts are well known in MRI [72]. Even though magnetic susceptibility may be detrimental to MR image quality, it has been hypothesized that clinically useful information can be extracted from a magnetic susceptibility map [123]. Nonetheless, susceptibility is a bulk effect and its contribution to distortion depends on the shape, the susceptibility and the orientation with respect to the main magnetic field of the objects considered. Exact calculation of its effect is possible only in simple cases [20,120,121].

2.5 Eddy currents

The use of rapidly pulsed magnetic gradients in an environment where conducting elements are present implies that eddy currents may be associated with gradient switching.

Such elements include the cryostat, main magnet winding, shimming coils, RF coils and even the other gradient coils [41]. Such transient currents, according to Lenz law, have an effect in opposition to the linear gradient field and modify it in a time dependent fashion. The resulting effect can be detrimental to the resulting image. Ahn [2] reports effects such as SNR and point spread function (PSF) degradation, the latter undergoing both deformation and shift which implies spatial distortion. Misregistration of up to 2 pixels was observed.

In many aspects, the contribution of eddy currents to the field about the isocenter can be assimilated into a time varying linear gradient in the same direction as the inducing gradient. The appropriateness of this concept is of critical importance to the feasibility of the so-called pulse reshaping methods that attempt to modify the driving waveform in such a way that the overall gradient is close to the trapezoidal shape required. Ahn [2] verified through computer simulation the validity of the gradient reshaping technique for a system whose waveform was compensated for in this manner. His results show that it is satisfactory for a volume centered at the isocenter and within 60% of the gradient coil diameter. However, it has also been reported that the effect of eddy currents in the first few *ms* following gradient switching is more complex [22,50,74].

Time behavior of eddy currents can be modelled using an exponential formulation where a linearly rising step response $u(t)$ represents the uncorrected gradient. Also, a term represents the multiexponential damping from the presence of eddy currents with the corresponding time constant τ , and amplitude β , and this can be written as [61]

$$G(t) = u(t) \left[1 - \sum_{i=1}^n \beta_i \exp(-t/\tau_i) \right]. \quad (2.29)$$

A compensated waveform $G'(t)$ accounts for m out of the n decay terms that are present [52]. The filtering needed to obtain $G'(t)$ can be described by [84]

$$G'(t) = u(t) \left[1 + \sum_{j=1}^m \alpha_j \exp(-t/T_j) \right] \quad (2.30)$$

where T_j is the new time constant and α_j the new amplitude. The sets T_1, \dots, T_m and $\alpha_1, \dots, \alpha_m$ in Eq. 2.30 are derived from τ_1, \dots, τ_m and β_1, \dots, β_m in Eq. 2.29.

Another consideration for the applicability of pulse reshaping methods is the relative importance of long lived components in Eq. 2.29, a problem made more important in superconductive systems by the presence of the low temperature conductive surfaces of the dewar. In some cases, it may not be possible to compensate for them with filtering using m exponential terms to account for the n actually present. More importantly, long lived components may introduce a pulse sequence dependence on compensation [61].

It was reported that the importance of long lived components was greater in a large bore system (such as the ones used in MRI), so that the effect during the *on* period of the gradient can be seen as a mere gradient offset [1]. A typical manifestation of this is seen at short echo times when the compensating portion of the readout gradient is turned off too soon before the first echo pulse. The transient readout-like current is then present during the 180° echo pulse application and is added to the slice selection gradient, thereby tilting the actual selected plane [1,41]. Presently, most pulse reshaping techniques use the exponential decay model or more empirical waveform correction techniques, but generally exclude any kind of pulse sequence dependence [74,84].

The gradient shielding methods can be one of either *active* or *passive* techniques. The active approach attempts to decouple the gradient from the outer surface by surrounding the former by a network of cancellation currents [10,76]. A consequence of this approach is that the contribution of the cancellation currents is also sensed *within* the volume delimited by the gradient shield which calls for an integrated gradient-shield design [18]. The generalization of this solution to multishield screening has also been proposed to overcome this problem [77].

Passive screening consists of surrounding the gradient with a thick conducting shield [117]. If the sheet of conductor is made much thicker than the skin depth δ at the frequency of gradient switching, the shield perfectly mimics the gradient in its time behavior and spatial dependence. Nonetheless, gradient pulses with offset at the origin such as the ones used for slice selection cannot be perfectly compensated for using this

approach [76]. Similarly, the shield and gradient have to be perfectly colinear or base field shifts with otherwise offset free eddy currents will appear at the isocenter [30].

2.6 Conclusion

This chapter demonstrated that any practical approach to distortion correction must include its characterization in the context of application, as each cause may call for a dedicated solution. Nonetheless, it was shown that at least 3 causes, namely main field inhomogeneities, magnetic susceptibility and chemical shift can be assimilated into a unique effect. In the slice selection and readout directions, this effect causes geometrical distortion of magnitude characterized by the strength of the corresponding gradient, with no change in the shape of the point spread function. This suggests the appealing strategy of orienting the development of correction toward this type of distortion.

Chapter 3

Distortion in the context of stereotaxy

The last chapter outlined the principal theoretical considerations in MR image distortion. Following the main objectives of this thesis, this chapter details the problem of image inaccuracy in the general context of MRI with special emphasis on stereotactic applications.

3.1 Main field homogeneity and gradient field linearity

For the purpose of this work, the term *inherent distortion* represents the distortion attributable to the imager, including main field inhomogeneity and gradient field non-linearity but excluding susceptibility and chemical shift effects. Transient current effects are also excluded from the inherent distortion. Nevertheless, their effect will be examined in a later section in order to verify whether their presence introduces some pulse sequence dependence on the image non-linearity.

The MRI system on which experiments were carried out is a 1.5T S15HP Gyroscan

imager (Philips, Best, The Netherlands) with 10mT/m gradients. This superconductive unit features gradient waveform compensation but no gradient shielding. The manufacturer's data describes a field homogeneity of 4ppm over a 30cm diameter sphere centered at the isocenter of the magnet. The main magnetic field of the system is oriented along the axis of the magnet bore.

Inherent distortion of the system was first studied using the phantom shown in Fig. 3.1. The phantom provides a map of the distortion at 45 points on a square lattice of 50mm separation. Evaluating the distortion of the image with the help of a phantom involves evaluating the role of the main field inhomogeneity, the gradient field non-linearity and also possibly the eddy current effects with a given pulse sequence in the overall spatial linearity of the image. Nevertheless, it is known that such an approach may also be sensitive to bulk magnetic susceptibility (BMS) effects from the shape, composition and orientation of the phantom with respect to the direction of the main magnetic field, indicating the need for a large size phantom [20,102]. The use of this cylindrical phantom partly circumvents this problem since its axis was kept parallel to the z axis (also main field direction) and imaged at different positions along this direction¹ on either side of the system isocenter. The cylindrical symmetry involved ascertains that the BMS effect, if present, has only a radial dependence. This provides a way to evaluate its importance in the distortion map.

The error on the positioning of the rods was determined using the program "Test-program for calculation of spatial linearity" (TSPL) provided by Philips. The algorithm carries out the following steps:

1. High-pass filtering the image in order to sharpen the intensity profile of the rods.
2. Localizing the center of each rod, yielding a list of "candidates".
3. Determining the 9 candidates corresponding to the inner 9 rods.

¹Generally known as the cranial-caudal (CC) direction.

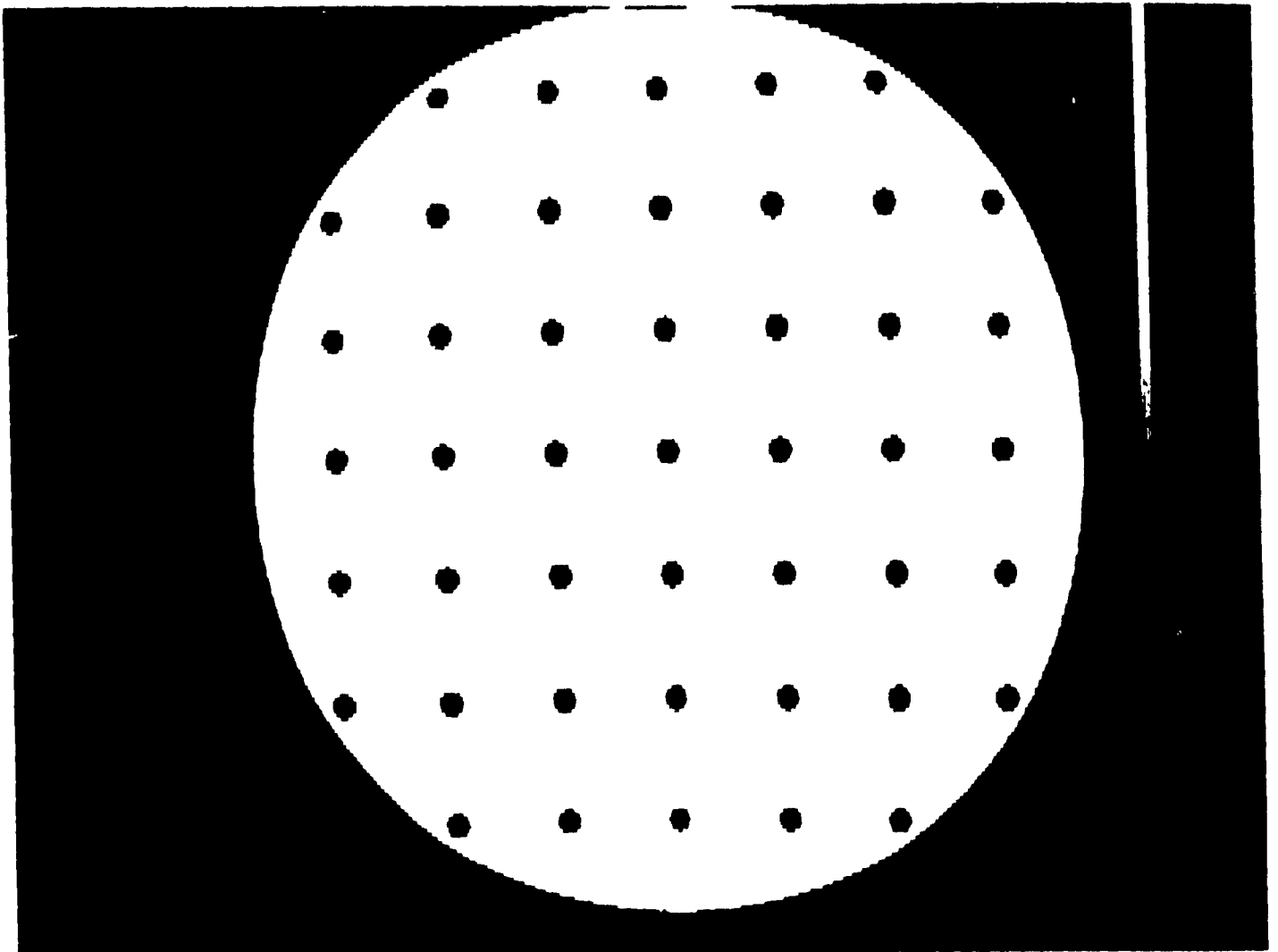


Figure 3.1: MR image of the phantom used for the spatial linearity test. It is a 400mm diameter cylinder containing 45 20mm long rods of 10mm diameter. The center of each rod is 50mm away from the centers of its 4 closest neighbors. The phantom is 13cm thick

4. Finding the absolute position of the central of the above 9 rods to determine the shift of the phantom from the coordinate axis.
5. Finding the angulation between one central line of rods and the angularly closest gradient ². This determination relies on the assumption that the image non-linearity in the area where the 9 central rods are situated is not important.
6. Matching the remaining 36 rods.
7. Determining the distortion seen by each rod from their theoretical position in an undistorted phantom with the shift and angulation found at steps 4 and 5.

For the purpose of performing this distortion evaluation so that it reflects the conditions of stereotaxy with the OBT frame, described in Section 3.4, one has to consider the dimensions of the parallelepiped bound by the fiducial marker plates, i. e. a volume of approximate dimensions $17\text{cm} \times 25\text{cm} \times 18\text{cm}$ in the CC, anterior-posterior (AP) and left-right (LR) directions respectively. Since most of the patient's head lies within the stereotactic frame, this volume comprises practically all targets. A series of transverse images was acquired using a spin-echo sequence with $TE = 50\text{ms}$ and $TR = 200\text{ms}$. Also, the slice thickness was 3mm with a field of view (FOV) of 420mm and an image matrix of 256^2 . A 2D FT sequence with slice selection was used, but the 2D nature of the phantom ensured that image non-planarity did not change the apparent position of the rods, assuming that the inherent distortion did not vary much within the distance corresponding to the error on slice selection. The phantom was imaged in 7 positions along the CC axis, the midplane of each of these slices being placed at 120, 100, 50 and 0mm from the isocenter on both the cranial and the caudal side.

For each position of the phantom, 5 or 6 ³ readout gradient bandwidths were assessed: 195.3, 108.6, 72.4, 54.3, 43.4 and 36.2 Hz/pixel . Mesh plot representations of the

²For the purpose of evaluating this rotation, positive values represent a clockwise rotation as perceived from *behind* the patient head

³In some cases, the software could not handle the important distortions present at 36.2Hz/pixel .

distortion in the given plane of the image are given for each CC phantom offset at 108.6 and 43.4Hz/pixel over the portion of the FOV which was considered as significant from the point of view of stereotaxy. Assuming that the center of the volume specified above is positioned within 2cm from the isocenter, this was chosen as 300mm in the AP direction vs 200mm in the LR direction. As an aid to the eye, surface smoothing through biharmonic interpolation was carried out. The coordinates of the points delimiting the space domain of the phantom are given along with proper identification of the image orientation. For all practical purposes, the maps can be considered as centered at the isocenter since the actual shift was generally kept under 1cm in each transverse dimension.

The error on rod localization can be considered as equal to half a pixel, or 0.8mm. Also, this uncertainty is repeated on the central rod. Imprecision on this last rod position unavoidably has some repercussions on the distortion as calculated for each other rod since the theoretical phantom position at the basis of this calculation depends upon central rod localization (step 4 in the algorithm). The error on the evaluation of the distortion in each direction was therefore 1.2mm. Furthermore, the distortion of the central rod is normalized to zero, which may not correspond to reality, particularly away from the isocenter along the CC direction as this is the case for some of these images. The component of this central rod distortion attributable to main field inhomogeneities therefore mimics a constant field added to the existing inhomogeneities as seen from the distortion map of the image. Its effect is reflected in the different apparent shifts of the phantom along the readout gradient direction when varying the readout bandwidth. The extent of this inaccuracy on the position of the central rod was generally less than 3mm for the readout bandwidth and the CC offset of the images used. Another source of uncertainty on the geometrical distortion as measured with the phantom of Fig. 3.1 was found to be the error on the evaluation of the phantom angulation $\Delta\theta$ about its axis. As stated above, this angle is used to determine the initial position of the phantom and any uncertainty on its value corresponds to an imprecision of the shift that each disc has actually experienced. The error on each disc corresponding to this cause is

proportional to the distance of the disc considered from the center. The error on the angle was estimated as being $\pm 0.2^\circ$, which corresponds to $\pm 0.6\text{mm}$ for the radially farthest points and can be neglected in the face of the error due to finite pixel size.

As expected, all images include an area that is situated around the intersection of the plane with the bore axis and that exhibits good spatial linearity. However, the extent of this area is considerably reduced when looking at transverse slices away from the isocenter. The role of the readout gradient strength is clearly demonstrated for each given phantom position by the use of various bandwidths; images using 108.6 and 43.4 Hz/pixel are shown in Figs. 3.2 and 3.3. Table 3.1 also provides the average distortion at other readout bandwidth values. In Figs. 3.2 and 3.3, it appears that the decrease of the gradient strength does not provide a uniform increase in the average distortion, presumably reflecting the mixed contributions of the gradient field non-linearity and main field inhomogeneity, of which only the latter directly depends on the bandwidth. Moreover, no cylindrical symmetry in the distortion is apparent. Since any BMS effects should show such a characteristic from the previous argument concerning the symmetry of the phantom with respect to the main magnetic field, this contribution seems relatively small.

Even though it was previously enounced that the dimension along the CC axis of the volume for which good spatial linearity is required is approximatively 17cm (8.5cm at both sides of the isocenter) images are provided for a CC offset as high as 120mm in order to give an insight into the importance of adequate centering of the volume to be imaged. For instance, the distortion over most of the right-anterior quadrant of Fig. 3.2(C) is appreciably increased when looking at the corresponding area in Fig. 3.2(E), albeit the distance between these planes is only 2cm in the CC direction. Thus, it appears that a fast decline of the image linearity may affect the markers of an improperly centered frame at these distances from the isocenter.

The situation is improved significantly at smaller CC offset and at high gradient strength (108.6Hz/pixel), although some important values of distortion are met such

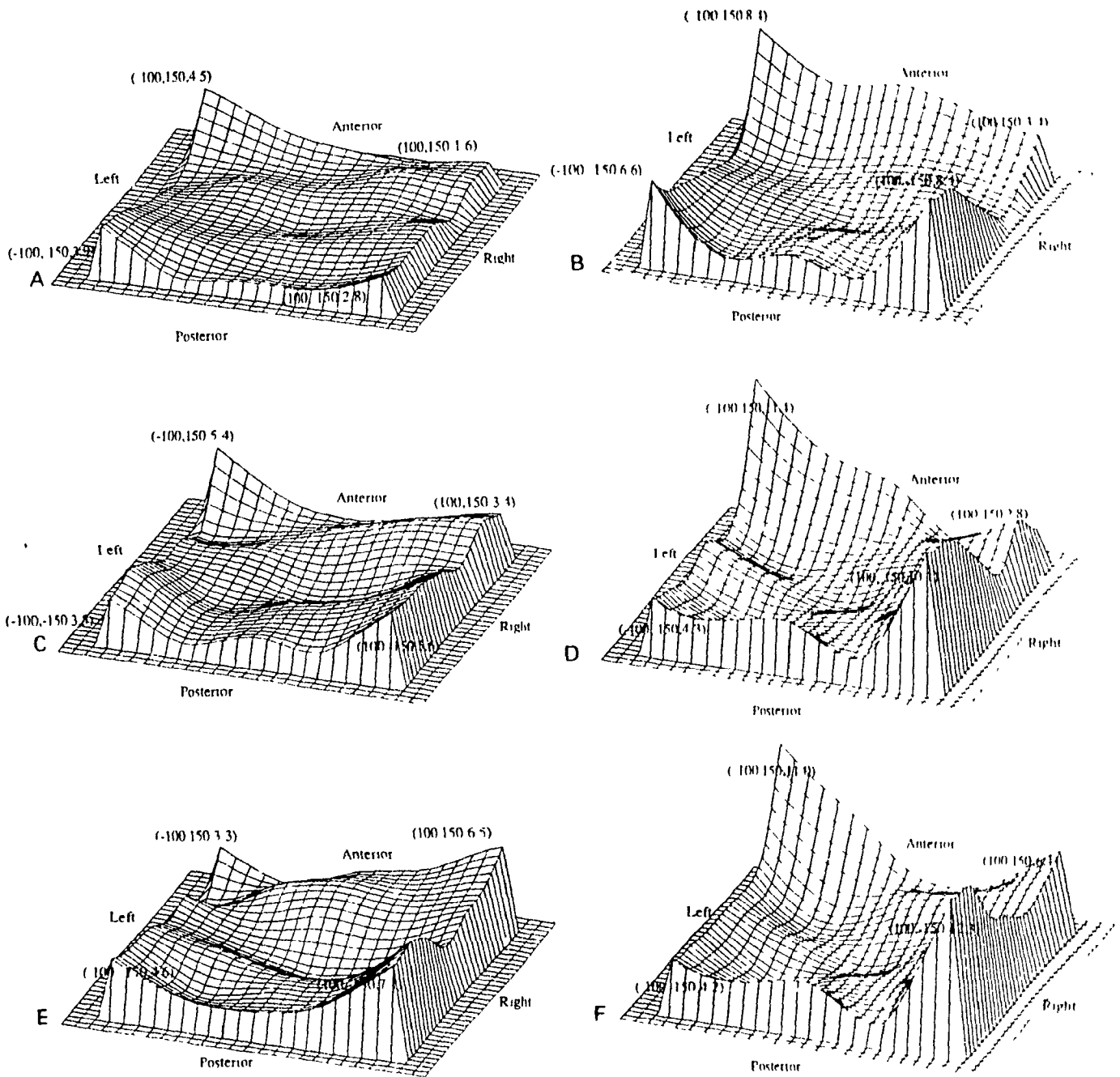


Figure 3.2: Image distortion in mm using a readout gradient bandwidth of $108.6 Hz/pixel$ ((A), (C) and (E)) and $43.4 Hz/pixel$ ((B), (D), (F)) The transverse plane positions from the isocenter in the caudal direction are from top to bottom 50, 100 and 120 cm . The phantom offset from the bore axis is generally inferior to 1 cm along both the readout and the preparation directions. The angulation ranges from 0 to 1.2°

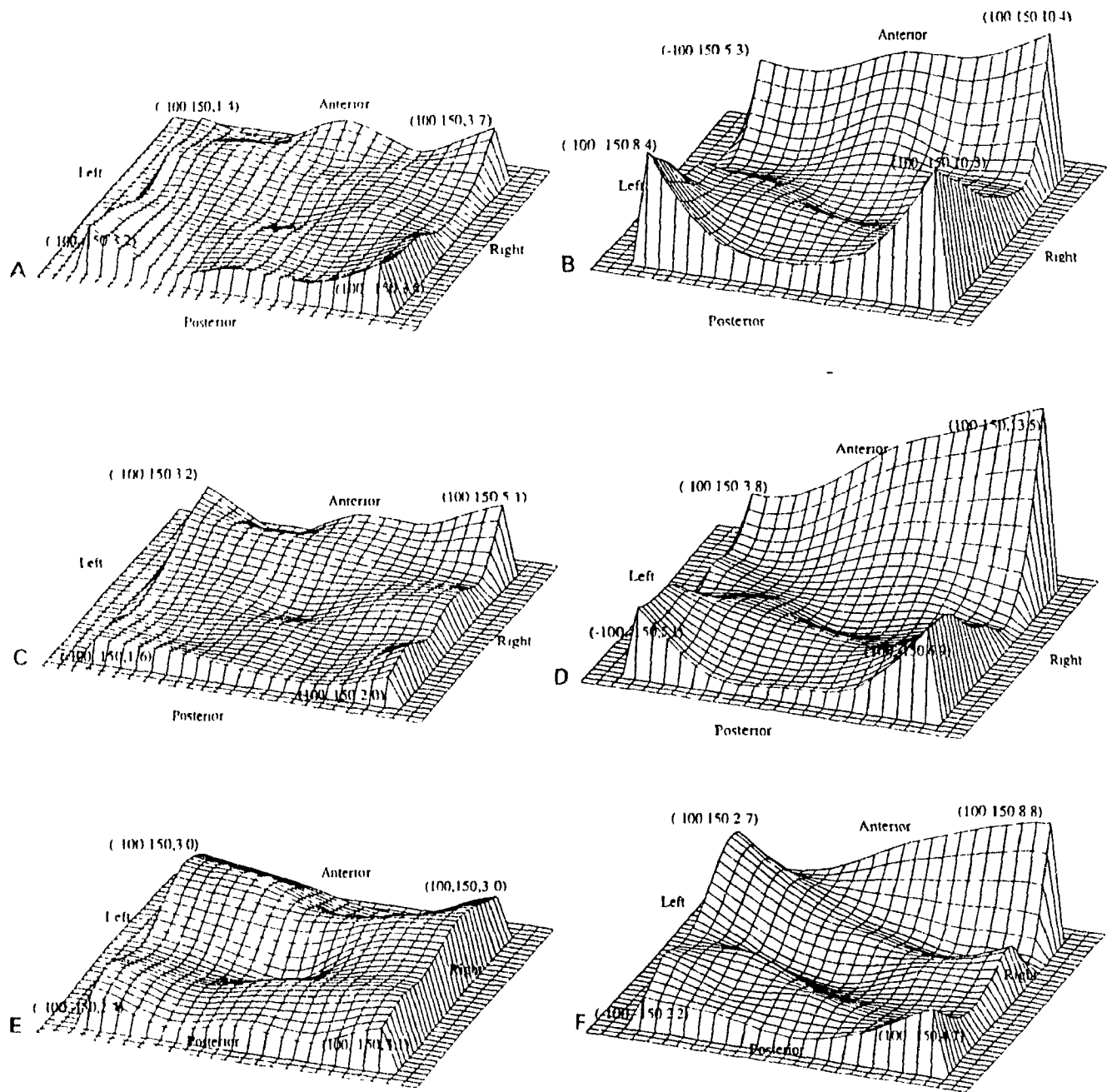


Figure 3.3: Image distortion in *mm* using a readout gradient bandwidth of 108.6Hz/pixel ((A), (C) and (E)) and 43.4Hz/pixel ((B), (D), (F)) The transverse plane positions from the isocenter in the cranial direction are from top to bottom 0, 50 and 100*cm*. The phantom offset from the bore axis is generally inferior to 1*cm* along both the readout and the preparation directions. The angulation ranges from 0.5 to 1.2°.

as in the anterior-right corner in Fig. 3.2(A). This indicates that distortion may occur at the edges of the FOV, where the fiducial markers may be found [27]. On the other hand, most of the FOV is affected by important image distortions when a low gradient strength is employed. Hence, it seems that the question of image integrity is mostly important for the proper imaging of the fiducial markers rather than the head, provided that a higher gradient strength is used ($\geq 100 Hz/pixel$). Nevertheless, one must not forget that a larger readout bandwidth is used at the expense of a decreased SNR.

In Table 3.1, the distinct behavior of the distortion between the readout and preparation directions is apparent. In the preparation direction, no significant change occurred when different readout bandwidths were used. On the other hand, there is a distinct trend in the readout direction for the distortion to decrease with increasing readout gradient strength. This is consistent with the expected inverse proportionality of distortion, caused by B_0 inhomogeneities, with readout bandwidth.

3.2 Contribution of the main field inhomogeneity to inherent distortion

It was seen in Figs. 3.2 and 3.3 that the spatially variable dependence of distortion on the gradient strength indicated that the main field inhomogeneity does not represent the sole contribution to inherent distortion. One other hint of this is the presence of distortion along the phase encoding or preparation gradient direction in Table 3.1. Also, the observed variation of the distortion with gradient strength along the readout direction does not seem to be solely the consequence of the inverse proportionality with the gradient strength. This last feature is more obvious when one examines the plot of relative distortion in the readout direction versus water-fat shift in Fig. 3.4 obtained from the data of Table 3.1. Note that water-fat shift is just another way of expressing the gradient strength at fixed FOV and image matrix size, and characterizes the number of pixels in the readout direction separating 2 point sources of fat and water situated

Offset [mm]	$\Delta\nu$ [Hz/pixel]	Δ Position (Prep.) [mm]	s_p [mm]	Δ Position (Read) [mm]	s_r [mm]	Δ Position (Total) [mm]
120 Caudal	43.4	1.8	1.3	4.6	4.5	4.9
	54.3	1.9	1.4	4.3	4.0	4.7
	72.4	2.0	1.5	3.9	3.2	4.4
	108.6	2.0	1.5	2.8	1.9	3.4
	195.3	2.1	1.5	2.6	1.7	3.3
100 Caudal	43.4	1.3	1.0	4.4	4.2	4.6
	54.3	1.4	1.0	3.6	3.6	3.9
	72.4	1.2	1.0	3.5	3.0	3.7
	108.6	1.3	0.9	2.3	1.7	2.6
	195.3	1.4	1.1	1.9	1.4	2.4
50 Caudal	36.2	0.8	0.6	4.9	5.1	5.0
	43.4	0.7	0.5	3.5	3.7	3.6
	54.3	0.8	0.6	3.1	3.1	3.2
	72.4	1.0	0.7	2.9	2.6	3.1
	108.6	0.7	0.5	1.5	1.4	1.7
Isocenter	195.3	0.8	0.5	1.4	1.1	1.6
	36.2	0.8	0.7	4.1	4.9	4.2
	43.4	0.8	0.6	4.0	4.0	4.1
	54.3	0.7	0.5	2.6	3.1	2.7
	72.4	0.7	0.5	2.4	2.6	2.5
50 Cranial	108.6	0.8	0.6	1.4	1.4	1.6
	195.3	0.8	0.5	1.1	1.0	1.4
	36.2	1.4	0.9	3.3	3.6	3.6
	43.4	0.9	0.6	3.4	3.3	3.5
	54.3	0.8	0.6	2.3	2.2	2.4
100 Cranial	72.4	1.0	0.7	1.9	1.9	2.1
	108.6	0.8	0.6	1.4	1.1	1.6
	195.3	0.9	0.7	1.1	0.8	1.4
	36.2	1.5	1.0	2.9	3.1	3.3
	43.4	1.7	1.1	2.4	2.5	2.9
120 Cranial	54.3	1.4	1.0	2.3	2.1	2.7
	72.4	1.5	1.1	2.0	1.7	2.5
	108.6	1.6	1.1	1.8	1.3	2.4
	195.3	1.5	1.0	1.8	1.2	2.3
	36.2	2.4	1.5	3.4	3.2	4.2
120 Cranial	43.4	2.5	1.6	2.9	2.5	3.8
	54.3	2.1	1.5	2.9	2.0	3.6
	72.4	2.3	1.5	2.8	2.0	3.6
	108.6	2.0	1.4	2.5	1.5	3.2
	195.3	2.0	1.4	2.7	1.5	3.4

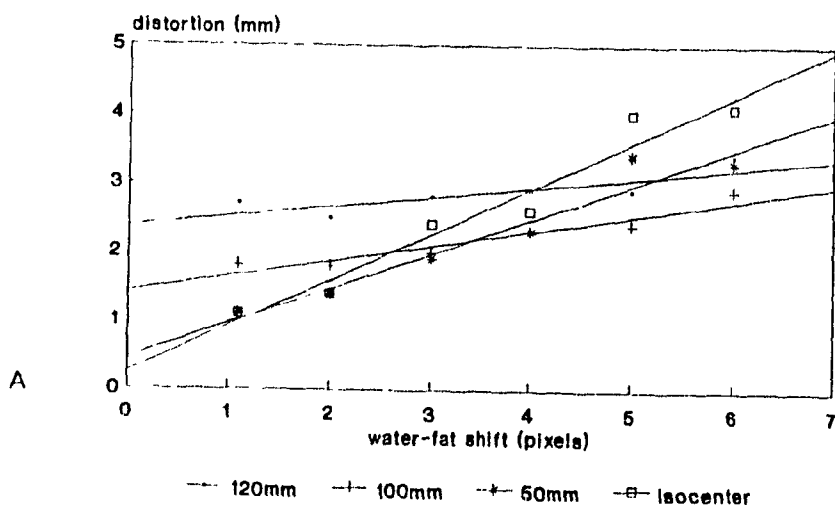
Table 3.1: Summary of the distortion mapping experiments using the spatial linearity phantom. Transverse slices were acquired with various phantom positions and were repeated with at least 5 different gradient strengths. The average Δ Position and standard deviation s for each direction are taken on all 45 rods of the phantom in Fig. 3.1

at the same position due to their different chemical shift. For instance, a water-fat shift of 1 pixel corresponds to a readout gradient bandwidth of $217\text{Hz}/\text{pixel}$ with the imager used for the experiments described here. Fig. 3.4 was obtained from the data of Table 3.1 for all 7 phantom positions.

The plots (A) and (B) of Fig. 3.4 exhibit the expected behavior with gradient strength when fitted in a least squares sense. The non-zero y -axis intercept confirms the presence of another contribution to distortion which is not affected by the use of a high gradient strength. To see that this is compatible with the presence of non-linearity of the readout gradient field, it suffices to consider that this latter type of distortion has the same effect in the readout gradient direction as main field inhomogeneities, except for the dependence upon readout gradient strength. This simply comes from the fact that this non-linearity is proportional to the current circulating in the coils, itself determining the strength of the gradient. This therefore implies that the y axis intercept represents the effects of gradient field non-linearity alone since the effect of main field inhomogeneities is thereby extrapolated to zero. For the plots of Fig. 3.4, the value of this intercept increases when moving away from the isocenter. This is consistent with the known characteristics of the magnetic gradients, namely that their linearity is optimized about the isocenter and constitutes another justification for imaging as close as possible to this point.

Another technique to verify the role of both types of encoding consists of comparing 2 images taken using the same imaging parameters except that the direction of the preparation and readout gradients are exchanged. In these conditions, the contribution of distortion due to main field inhomogeneity should remain unchanged in magnitude but be in the new direction. On the other hand, there is no reason for the effect of gradient field non-linearity in terms of distortion to be the same when playing the role of phase rather than frequency encoding. Consequently, a technique to study the relative importance of gradient field non-linearity *vs* main field inhomogeneities is to verify the relative displacement of the rods in the image of the spatial linearity phantom when the

Average distortion vs water-fat shift
(cranial)



Average distortion vs water-fat shift
(caudal)

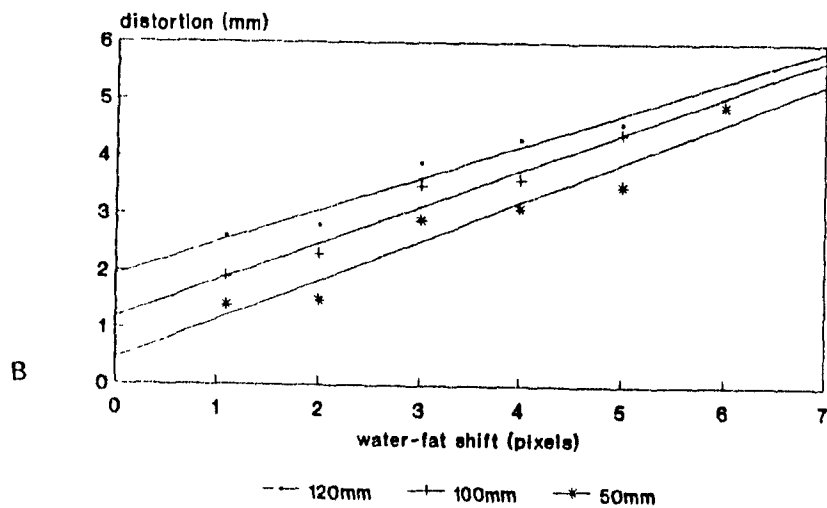


Figure 3.4: Plot of average distortion observed in the readout gradient direction using different bandwidths expressed in pixels of water-fat shift. 4 cranial phantom positions are given in (A) while 3 caudal positions are present in (B). Straight lines are obtained using the least squares fit.

gradient exchange is performed. A 45° orientation of this displacement with respect to both gradients would then indicate the predominant role of main field inhomogeneities.

In order to explore this behavior, such pairs of images were acquired at many water-fat shift settings (1.1, 1.5, 2.0, 2.5, ..., 6.0) at all three image orientations and using the same phantom as before. Prior to acquiring the second image of each pair with exchanged gradients, resonant frequency determination was inhibited in the scan preparation sequence in order to ensure consistency. This time, the positions of the rods were measured manually with the help of a computer mouse. One image of each pair was normalized in order to ensure that the position of the isocenter would be the same with both images, a reasonable assumption since the geometrical distortion from most causes is small at this point. The precision of manual rod localization is 2mm in each direction.

Fig. 3.5 shows typical results obtained for such a test. The maps illustrate the direction of the displacement vector represented by the arrows from the pairs of images described above. The length of these arrows is proportional to the modulus of this displacement vector. Results for all three slice orientations are presented.

Even though the precision of the method did not allow for the significant measurement of distortion greater than 2mm in each gradient direction, it is easily appreciated that the orientation of the readout gradient is of prime importance with higher values since the resultant displacement then has an orientation obtained from the addition of two perpendicular and equal magnitude vectors. If gradient field non-linearity were a relatively important cause for the distortion observed, the inversion of the roles of both gradients would be expected to change the importance of the distortion in the given direction from this new traded role and thereby cause the displacement vector to behave in a more complicated way than it does.

It is thus possible to conclude that field inhomogeneity determines much of the geometrical integrity of the images at low gradient strength, such as with $43.4\text{Hz}/\text{pixel}$. This indicates that these inhomogeneities, in that situation, offer a greater contribution

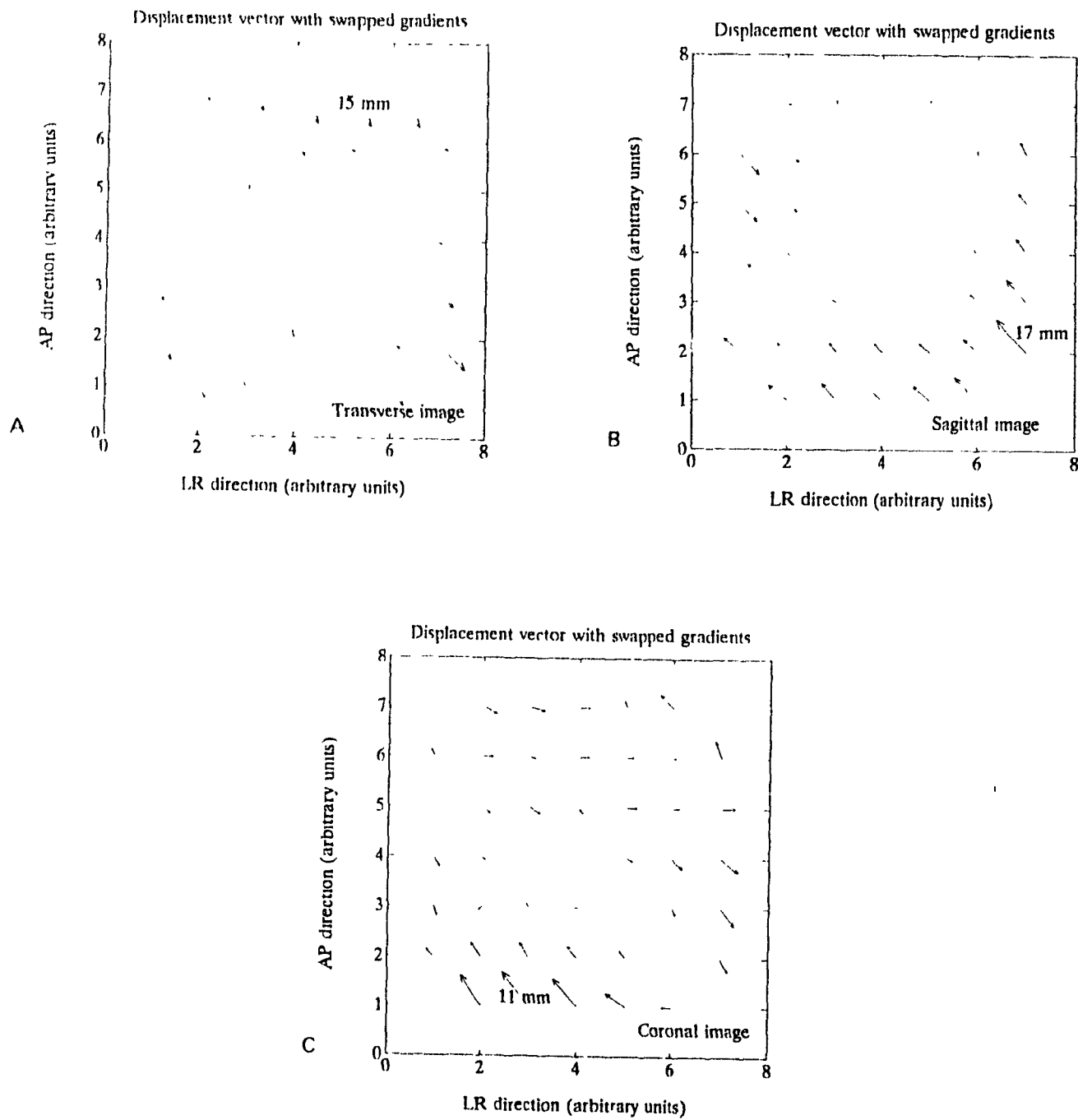


Figure 3.5 Displacement vectors at various sites of the 420mm FOV when the frequency and phase encoding gradients are interchanged. The images were acquired with $TR=200ms$ and $TE=50ms$ at a readout gradient strength of $43.4Hz/px/cl$. In each case, the midplane of the image is centered at the isocenter. The highest magnitude of the displacement vector is indicated. The image orientations are transverse, sagittal and coronal corresponding to (A), (B), and (C) respectively.

to image geometrical distortion than magnetic gradient field non-linearity. Therefore, distortion correction of images acquired at low readout gradient strength first calls for ways of dealing with B_0 inhomogeneities.

3.3 Transient currents effect on spatial linearity

As mentioned in Chapter 2, the geometrical integrity of the image can depend upon the pulse sequence used. This happens if the gradient switching preceding the readout gradient application contributes to distortion by inducing eddy currents which have not fully relaxed by the time of signal acquisition. This generally happens if eddy currents with a long time constant are present since these are often not compensated for when waveform reshaping is used. Note that the MR imager used for the described experiments uses a compensated gradient waveform as described by Eq. 2.30 but has unshielded gradients. In order to obtain some insight into this aspect of image distortion, images were acquired using different TE's. The extent of the echo time reflects the time allowed for transient currents induced by previous gradient switchings to relax prior to signal acquisition.

Transverse imaging of the spatial linearity phantom was performed. Different echo times, from 30ms to 100ms and a readout bandwidth of 94.4Hz/pixel were used. No single pair of images with different echo times exhibited discrepancies in the position of the rod, which suggests that eddy currents play a limited role in the distortion with this imager.

3.4 OBT stereotaxy frame

As mentioned in the first chapter, the stereotactic frame used for these experiments was the Olivier-Bertrand-Tipal stereotactic model developed at the beginning of the 80's and intended to be a multi-modality device [88,89,92]. At the Montreal Neuro-

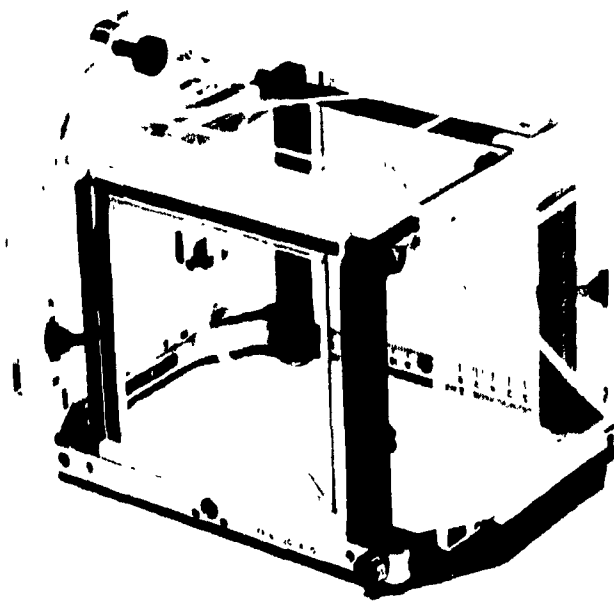


Figure 3.6: Illustration of the OBT stereotactic frame used in the described experiments. The frame is shown with the set of fiducial marker plates used with MRI.

logical Institute (MNI), it has been used for many years on a routine basis with CT, MRI and digital subtraction angiography (DSA), although MRI is used primarily for visual guidance rather than position calculation due to geometrical distortion problems. The imaging session is followed by treatment, either surgery or radiosurgery which is generally performed on the same day. Fig. 3.6 illustrates the OBT frame.

The frame is a cubical structure mounted on a base ring, the plane of which is normal with respect to the scanner axis (in the case of CT and MRI) and therefore to the main magnetic field in these experiments. The frame is made of both aluminum and plastic (polyamide-imide). The choice of either material for each post is dictated by 2 considerations: the need to avoid a metallic closed loop creating induction problems in MRI and to ensure that the four posts normal to the radiation plane in CT are made of a low effective atomic number in order to avoid potential CT artifacts due to excessive

x-ray attenuation in the neighborhood of the scanned volume. The RF body coil is used in stereotactic MR imaging because the frame does not fit comfortably in the head coil.

The frame is rigid and resistant which renders it able to support surgical instruments for stereotaxy guided operations. It provides locking chucks through which up to 5 carbon fiber pins can be inserted and placed in small cavities dug in the skull under local anesthesia. They are then locked into place with the help of the chucks and provide complete immobilization of the head with respect to the frame. The apparatus is light and can be well tolerated by the patient for the one day duration required to perform both imaging and treatment.

In order to perform localization with stereotactic imaging, the field of view of each image must comprise some landmarks of known geometry, a role played by the fiducial marker plates. The frame is illustrated in Fig. 3.6 bearing the MRI fiducial marker plates. When imaging with CT, another set of plates is used in which markers of high radio-opacity, generally aluminum or copper, are embedded. In the case of MRI, channels of square section serve as the markers and are filled with a CuSO_4 solution.

All MRI and CT marker plates are made of five segments constituting a square with a side of 130mm (considering the axis of the channels) added of a diagonal as shown in Figs. 3.6 and 3.7. In CT, 4 plates (AP and laterals) are used and the patient head is inserted in the frame through one of the remaining sides. When the MRI set is used, 5 out of the 6 sides of the cubical structure formed by the stereotactic frame are occupied by a marker plate. Hence, 3 plates are intersected with coronal and sagittal slices in MRI, whereas 4 appear on transverse slices with MRI and CT. With DSA, localization is carried out with the help of a pair of marker plates mounted on the frame on the AP and lateral sides and made of plastic in which are embedded metal pellets corresponding to the corners of a 6cm side square [42]. Differential magnification of the square allows unique determination of 3D coordinates of any point if two views are provided.

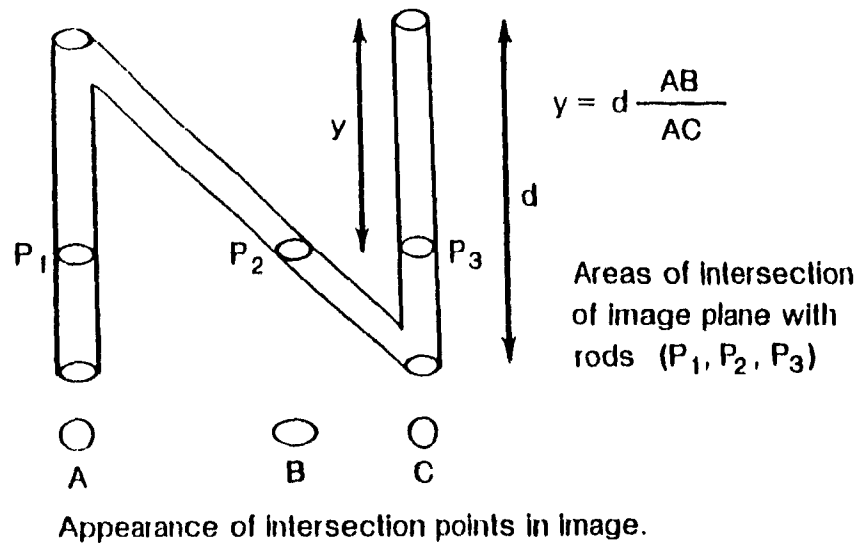


Figure 3.7: Fiducial marker plate mounted on the OBT stereotactic frame. It is made of plastic in which is embedded a z-shaped marker. In the case of MRI, it is a cavity filled with a copper sulfate solution whereas the CT counterpart is made of aluminum or copper.

3.5 Localization with the fiducial markers

The OBT stereotactic frame possesses its own coordinate system xyz in which the position of any point is described. The origin of the frame coordinate system is at the lower left corner of a sagittal midplane image (with respect to the frame), at $1cm$ in the caudal direction and $1cm$ in the anterior direction with respect to the marker situated in the lower left corner. The orientation of the 3 axis are respectively for x , y and z the posterior, cranial and right directions. The fiducial markers are used to provide a correspondence between any screen coordinates (u, v) of a given image and the frame coordinates (x, y, z) . At least 3 points are necessary to provide a complete knowledge of the relationship between the systems uv and xyz and for each plate, the point P_2 of Fig. 3.7 is the one whose coordinates are sought. Since all image orientations provide

at least 3 sets P_1, P_2, P_3 (at least as many plates are intersected), this knowledge can be acquired.

Fig. 3.7 illustrates for a plate the relative positions of the 3 intercepted markers P_1, P_2, P_3 of an image at a distance y from the side of this plate. y is calculated from the relative positions of the markers using a formula obtained from the presence of similar triangles. A second coordinate is readily obtained since $P_1 P_2 = y$ whereas the third locates the point P_2 of a plate along an axis normal to this same plate, so is already known. All the calculated distances are added some value to account for the position of the origin of the stereotactic frame coordinate system.

Once the frame coordinates of all 3 points P_2 have been determined, they and their corresponding screen coordinates may be used to retrieve the frame coordinates (x, y, z) of any point in the image from its screen coordinates (u, v) using

$$\begin{bmatrix} x & y & z \end{bmatrix} = \begin{bmatrix} u & v & 1 \end{bmatrix} \begin{bmatrix} u_1 & v_1 & 1 \\ u_2 & v_2 & 1 \\ u_3 & v_3 & 1 \end{bmatrix}^{-1} \begin{bmatrix} x_1 & y_1 & z_1 \\ x_2 & y_2 & z_2 \\ x_3 & y_3 & z_3 \end{bmatrix} \quad (3.1)$$

where the 3 pairs of points $(x_i, y_i, z_i), (u_i, v_i)$ corresponding to the point P_2 of every 3 plates are determined as described above [13,44]. The inverse correspondence is therefore

$$\begin{bmatrix} u & v & 1 \end{bmatrix} = \begin{bmatrix} x & y & z \end{bmatrix} \begin{bmatrix} x_1 & y_1 & z_1 \\ x_2 & y_2 & z_2 \\ x_3 & y_3 & z_3 \end{bmatrix}^{-1} \begin{bmatrix} u_1 & v_1 & 1 \\ u_2 & v_2 & 1 \\ u_3 & v_3 & 1 \end{bmatrix} \quad (3.2)$$

and allows one to retrieve the pixel position from the stereotactic coordinates. Although slices parallel to one of the 3 coordinate plates were assumed above, the formalism still holds for angled slices and the same equations can be used, although non-angled slices are generally sufficient.

3.6 Distortion on the fiducial markers

Results of the beginning of this chapter motivated further studies to characterize the integrity of the fiducial markers positioning in MR images. This showed that some distortion phenomenon particular to the fiducial marker plates plays in fact a greater role than the contribution from inherent distortion of the imager. Some authors have previously verified the integrity of the stereotactic coordinates calculation using the fiducial markers and the OBT stereotactic frame and characterized the effect of the frame on the distortion seen by the markers [27]. Their results are briefly summarized in the next subsection. Nevertheless, this research focussed on the contribution of bulk magnetic susceptibility (BMS) effects to account for distortion observed despite the use of a modified stereotactic apparatus free from the first problem. The results of this investigation are exposed in the other subsection.

3.6.1 Influence of the stereotactic frame on marker positioning

This work was first aimed at verifying the spatial linearity of images of the phantom in Fig. 3.8. This was accomplished with the help of the stereotactic analysis software routinely used at the MNI for, among other uses, the calculation of the position of displayed targets. Such an approach reflects both the proper imaging of the phantom and of the fiducial markers with the help of which the frame coordinates are calculated. It was first demonstrated that BMS effects from the irregular shape of the phantom were not significant so that this phantom was an appropriate choice for the study of image linearity.

Errors on the relative separation of points on the phantom of up to $5mm$ were observed. Following that, efforts were directed towards isolating the cause of those errors. Since the distortion effect in play occurred along the readout direction, the phenomenon was attributed to a static field type of error. This suggests as possible causes the main field inhomogeneities or the misimaging of the fiducial markers from

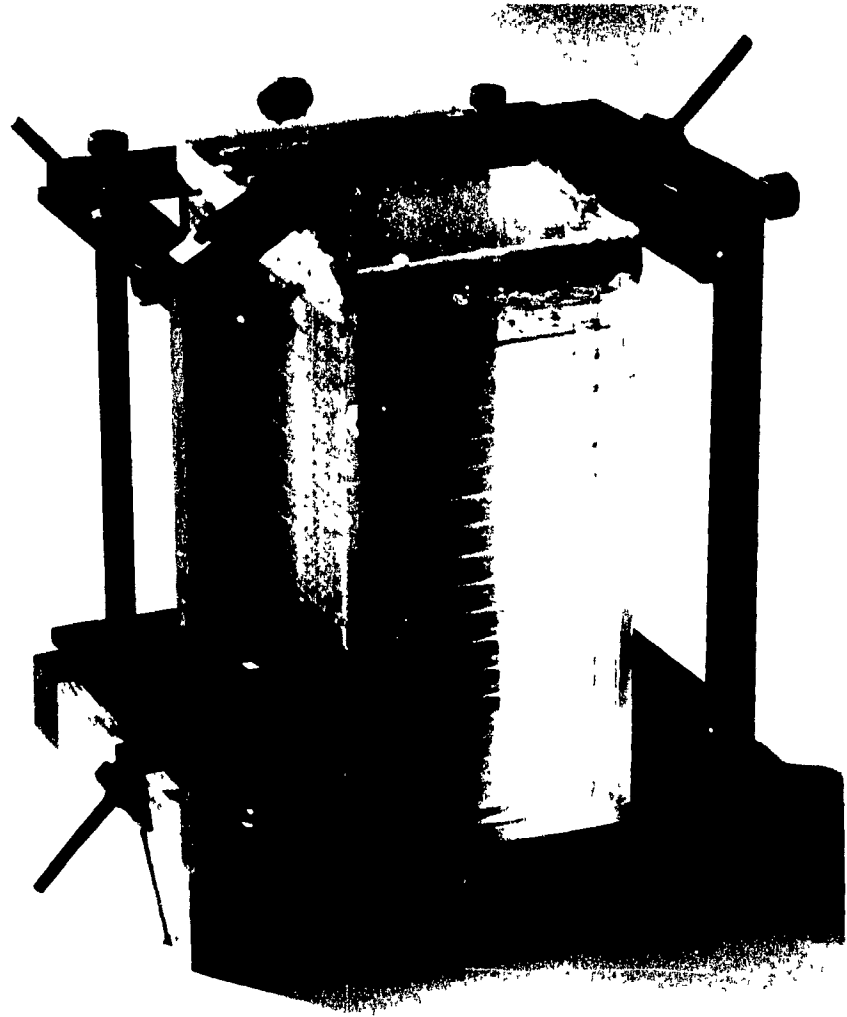


Figure 3.8: Phantom used for imaging with the stereotactic frame. It is made of a series of parallel 1.5mm thick plates whose midplanes are 1cm apart from one other. Carved in each plate is a square grid of 1.5mm diameter holes whose centers are separated from one another by a distance of 1cm . Such a phantom allows evaluation of the spatial linearity from the measurement of the relative separation of the holes.

the influence of the aluminum components of the frame, even though aluminum only exhibits weak paramagnetic properties. The independence of this phenomenon with respect to the relative position in the magnet bore was demonstrated and therefore incriminated the misimaging of the markers in the vicinity of the aluminum posts of Fig. 3.6 as the probable cause of the observed discrepancies. This was also confirmed by the fact that the problem was not encountered with transverse images in which the intercepted parts of the marker plates are relatively remote from the aluminum components. Ferromagnetic compounds contained in aluminum alloy are believed to be the cause of this problem which was eliminated with the use of an experimental frame free from aluminum components.

3.6.2 BMS shift effect on the markers

In this work, the proper imaging of the fiducial markers in the light of possible distortions other than the ones associated with aluminum components was examined. The knowledge of the readout gradient role in determining the direction of any distortion arising from susceptibility effects or main field inhomogeneities was used by looking at the subtraction of 2 similar images with exchanged readout and preparation gradients. Following the acquisition of each second member of any one pair, the resonant frequency was locked so that no variation of this parameter could possibly affect the validity of the method by yielding different values of distortion for the same static field error. 3D FT imaging was chosen to avoid some distortion in the slice selection direction from the presence of static field error, therefore ensuring that any distortion from this cause would occur in the readout gradient direction only.

The resonant frequency of the imager as determined by the system was compared to the one of the human head in similar conditions in order to ascertain that the fiducial markers were imaged at a resonant frequency typical of clinical cases. In Table 3.2, it is shown that no discrepancy large enough to be of any importance with a readout bandwidth of about $100Hz/pixel$ and a FOV of $250mm$ (similar to the values used with

Object Imaged	Resonance Frequency [Hz]
Patient 1	63867284
Patient 2	63867291
Patient 3	63867228
Phantom (trial 1)	63867290
Phantom (trial 2)	63867301
Phantom (trial 3)	63867276

Table 3.2: Typical resonant frequencies for head scans of patients and trials with the stereotactic phantom.

most experiments that were conducted) was found. This signifies that the behavior of the fiducial markers imaged in the presence of the phantom in Fig. 3.8 can be assumed to be representative of the situation occurring in routine stereotactic imaging where the susceptibility of the head rather than that of the phantom dictates the resonant frequency determined by the system during the scan preparation sequence.

Fig. 3.9 illustrates a typical coronal image of the phantom in Fig. 3.8 mounted in the stereotactic frame with its fiducial marker plates as it appears when using the Montreal Stereotactic Planning System. Another similar image was obtained with a change in the direction of the readout gradient from caudal-cranial to left-right and was subtracted from the image presented in Fig. 3.9, thus yielding Fig. 3.10(A). The image shows some apparent discrepancy on the position of the holes in the phantom that do not exceed 1mm. A more important effect is visible around the phantom where the transition in susceptibility is important, but is of no concern. Also, a small discrepancy is present on the lateral marker plates, but it does not exceed the dimensions of the marker itself. However, the most noticeable distortion feature is observed in the position of the cranial marker plate. Its extent in the subtracted image in both the vertical and horizontal directions is 3mm. The 45° orientation of the displacement confirms the involvement of either main field inhomogeneity or susceptibility effects.

The effect described above was shown to be perfectly reproducible which therefore



Figure 3.9: Coronal image of the stereotactic phantom as displayed with the Montreal Stereotactic Planning System. It was acquired with the fiducial markers in place on an aluminum free stereotactic frame. The slice thickness is $1.5mm$. TE and TR are respectively 30 and $200ms$ and the readout gradient was applied in the cranial-caudal direction (vertical, top to bottom) with a bandwidth of $108.6Hz/pxel$ and a FOV equal to $299.2mm$.

excludes any mechanical failure of the frame assembly. In order to determine whether this effect was characteristic of the top plate itself or due to its position in space (with respect to the imager, from inherent distortion), the anterior-posterior offset of the coronal slice was modified. This proved to have no influence on the distortion of the top plate. Furthermore, a sagittal pair of slices of the phantom was taken with exchanged gradients and the same distortion pattern was found to be present in the subtracted image on the top plate with again a discrepancy of $3mm$. Thus a similar static field error is involved since the FOV are alike and the bandwidths are the same. This sagittal subtracted image is presented in Fig. 3.10(B). However, a similar subtraction of images, this time with the transverse orientation, failed to demonstrate any occurrence of the

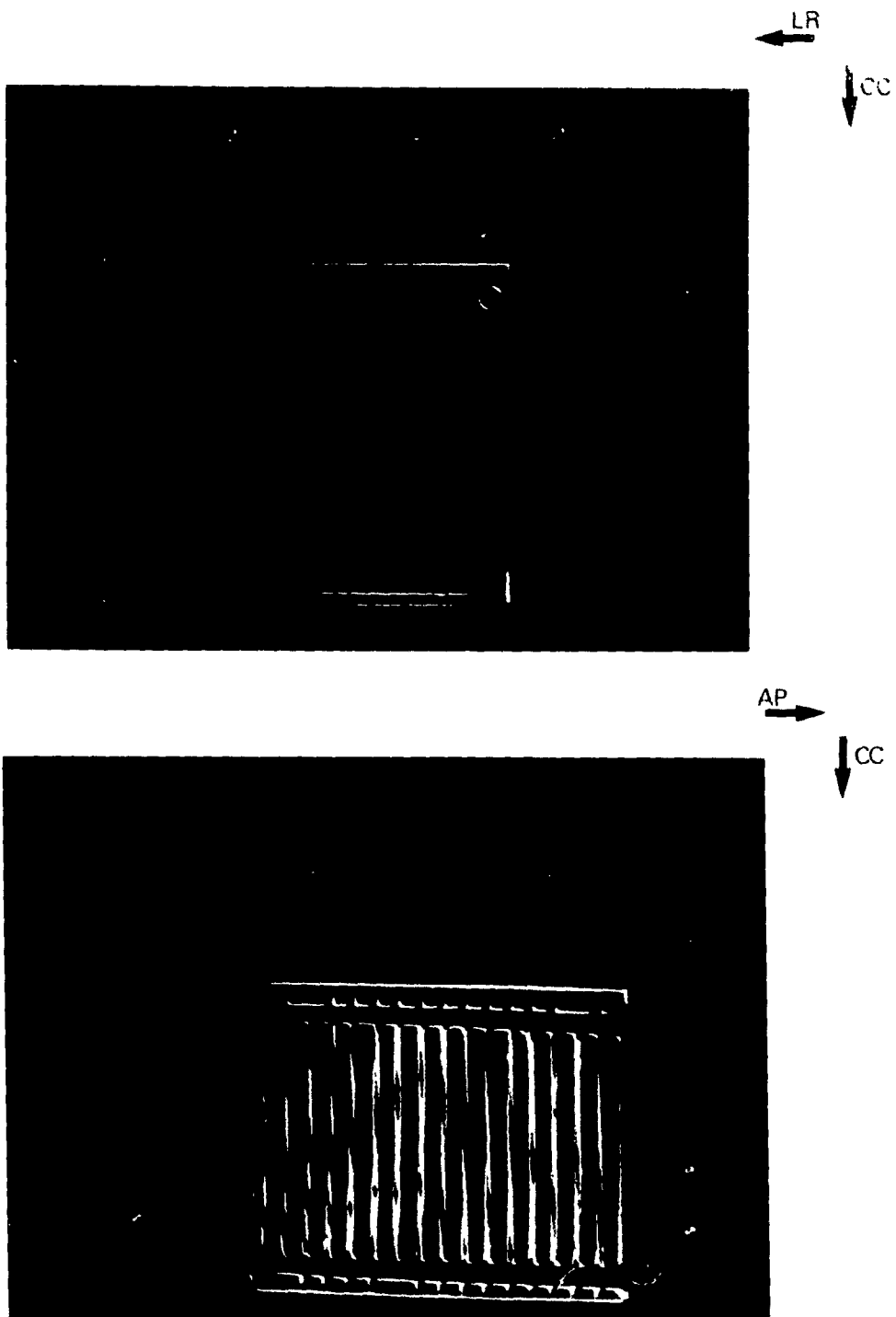


Figure 3.10: Result of the absolute subtraction of (A) two coronal and (B) two sagittal images. The readout gradient direction was changed before acquiring the second image of a given pair. The image distortion on the marker in both the coronal and the sagittal pairs is 3mm along the readout gradient direction, thus corresponding to a $3\sqrt{2}\text{mm}$ displacement in the above image. The FOV's were 299.2mm for (A) and 281.7mm for (B).

same marker distortion as shown by Fig. 3.11. The fact that no such phenomenon is visible on any transverse slice as well as its independence with respect to the position of the frame assembly within the magnet demonstrate that this effect is inherent to the frame itself. However, it is still unclear whether it is the plate itself rather than the phantom in close proximity that causes this. The second hypothesis was discarded when it was found that the distortion on the cranial plate was unchanged despite various attempted shifts in position of the phantom with respect to the markers and the frame ⁴.

It is thus apparent that the behavior of the plate in terms of geometrical integrity depends on a susceptibility effect characteristic of this plate. However, the composition and shape of the other plates is very similar to their distorted counterpart, except for the fact that the latter is the only one perpendicular (rather than parallel) to the main magnetic field.

In order to explain the effect observed with the help of the bulk magnetic susceptibility (BMS) concept, it is useful to write the shift in resonant frequency δ (evaluated in *ppm*) between an isolated nucleus and the same nucleus in a material environment as [20]

$$\delta = \delta_{\sigma} + \delta_s + \delta_x \quad (3.3)$$

where δ_{σ} is the shift from host molecule electronic shielding effects, δ_s is the shift from solvent electronic shielding effects and δ_x represents the BMS contribution. When all resonant nuclei share some common types of host molecules and solvent as it is the case in the experiments conducted with the stereotactic frame, the difference in resonant frequency in a homogeneous field can only be attributable to δ_x .

Nonetheless, the BMS shift of an object, besides depending upon the nature and shape of the material considered, also depends on the orientation with respect to the main magnetic field [20,121]. For instance, δ_x in a hollow infinite cylinder filled with

⁴Although the rest of the experiments of this chapter made no longer use of the pattern of the phantom in Fig. 3.8, its presence remained necessary to ensure appropriate imaging conditions.

resonant nuclei and parallel to the main magnetic field is

$$\delta_x = \chi_{inside}/3 \quad (3.4)$$

where χ_{in} is the volumetric susceptibility of the resonant substance⁵. However, at first approximation it becomes

$$\delta_x \simeq \chi_{air}/2 - \chi_{inside}/6 \simeq -\chi_{inside}/6 \quad (3.5)$$

when the cylinder is oriented perpendicularly to the main magnetic field and is surrounded by air. This could account for the different susceptibilities between all markers of transverse images and the top markers of sagittal and coronal images. Since the channels constituting each marker plate are either perpendicular or parallel with respect to the main magnetic field, it is tempting to explain the phenomenon using this description. Nonetheless, the fact that only the top plate suffers from this problem in both sagittal and coronal images suggests that another element is involved since all the channels present at those image orientations are perpendicular to the main magnetic field, yet only the ones that are part of the top plate exhibit some distortion effects.

It was then hypothesized that the observed distortion effect could be caused by the influence of the medium in the vicinity of the channels and the orientation of this medium with respect to the main magnetic field. Considering the images of Fig. 3.6 and assuming a coronal image orientation, it can be understood that since nothing distinguishes the vertical channels of the top plate from the vertical channels of the lateral plates (the channels all have a square section, the composition of the plates are identical and the shape of these plates are nearly the same) the hypothesis of a BMS effect involving the orientation of the material around the channels with respect to B_0 appears appropriate.

A test was made to validate this hypothesis by imaging a plate in the presence of the stereotactic phantom. Two image subtractions with exchanged gradients were carried out, one with the plate perpendicular to the main field (corresponding to the actual

⁵ χ is evaluated in *ppm* with respect to the resonant frequency of an isolated nucleus

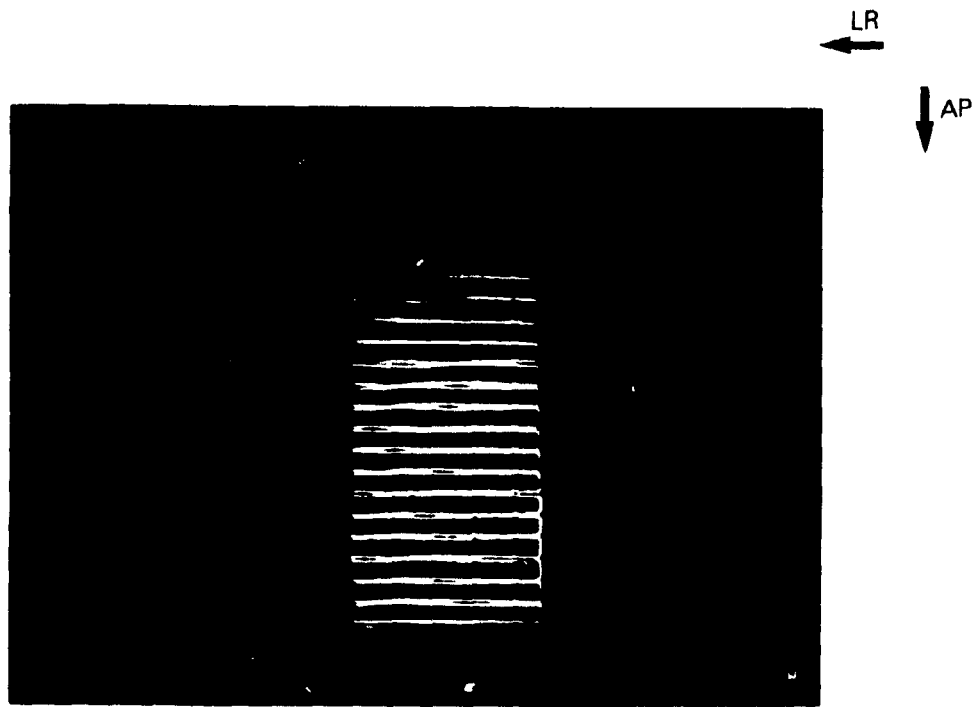


Figure 3.11: Result of the absolute subtraction of 2 transverse images acquired with the same parameters as Fig. 3.9 but for the direction of the readout gradient strength which was along the LR direction for one image and AP for the other. The lateral and AP marker plates show no distortion comparable to the one of Fig. 3.10(A) and (B). The FOV was 312.3mm .

orientation of the top plate) and one with the plate rotated by 90° about the axis of the filled channel. The rotation was performed in such a way as to leave the channel in the same position with respect to the magnet and the phantom in order to exclude any potential effect from inherent distortion or phantom susceptibility, even though earlier data indicated that the former element is unlikely to contribute to distortion. Furthermore, the copper sulfate solution was emptied out from all channels but one in order to demonstrate that the occurrence of this BMS phenomenon does not involve other sections (channels) of the fiducial marker plate. The subtraction of the images taken at both plate orientations is presented in Fig. 3.12.

Fig. 3.12(B) reveals the misimaging of the marker which suffers from a 9mm dis-

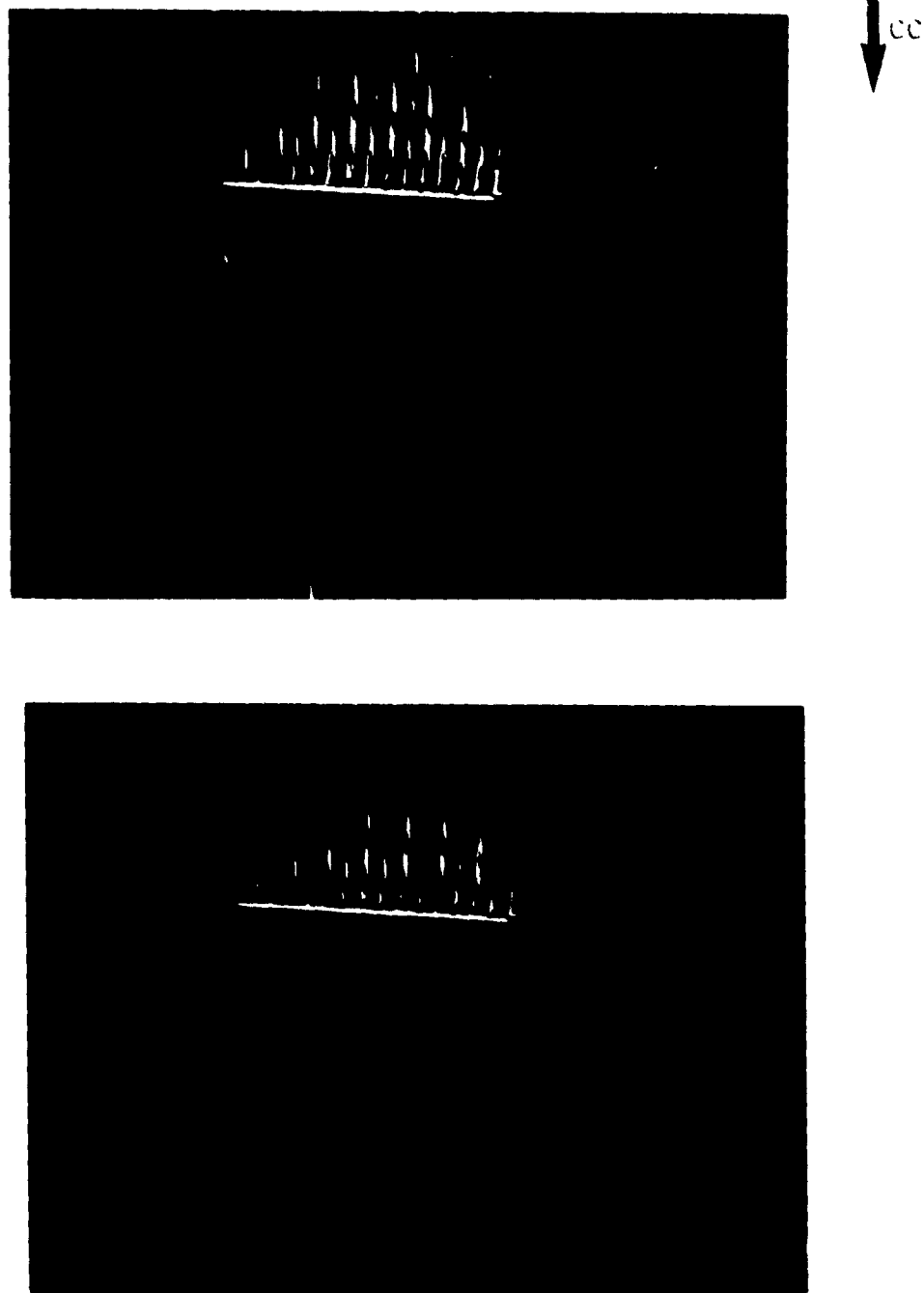


Figure 3.12: Subtraction of the images of the marker plate with the stereotactic phantom. TR and TE are respectively 200 and 50ms. The readout bandwidth is 36.2Hz/pixel and the FOV is 350mm. The plane of the plate is (A) parallel and (B) perpendicular to the direction of the main field. All channels were emptied except one. The effect of the rotation on the marker displacement in this last subtracted image is dramatic. This displacement corresponds to a 9mm marker distortion.

tortion at a readout bandwidth of $36.2\text{Hz}/\text{pixel}$, or $238 \pm 18\text{Hz}$. In this position, it is similar to the top plate mounted on the stereotactic frame whose distortion was 3mm at $108.6\text{Hz}/\text{pixel}$, corresponding to $279 \pm 54\text{Hz}$ in the case of Fig. 3.10(A) and to $296 \pm 54\text{Hz}$ in the case of Fig. 3.10(B). Both values are similar to the displacement obtained in Fig. 3.12(B) when a single channel was filled. This confirms the appropriateness of the model based on the assumption of a behavior dictated by the single channel geometry. On the other hand, one sees that the previous distortion is considerably reduced when the plate is parallel to the main field as in Fig. 3.12(A). This situation is similar to the perpendicular channels of the LR and AP plates which do not exhibit the same distortion phenomenon. Since the rotation was performed about the channel axis, no change could have possibly been brought to a contribution to distortion from field inhomogeneity, gradient field non-linearity or distant phantom influence from BMS effect if one of these was involved. Also, the section of the channel itself is square and the rotation was approximately 90° , so the symmetry involved ascertains that no effect from the shape of the filled part can contribute to a difference in susceptibility.

In order to obtain a quantitative explanation for this behavior, one would have to proceed with the calculation of the BMS shift of such a plate whose cross section is shown in Fig. 3.13. The work of Chu [20] has recently revealed the need for this phenomenon to be accounted for in NMR experiments. One can describe the resonant frequency shift δ_x seen by a nucleus in a compartment i using

$$\delta_x = \frac{D_i B_0 + I_i}{B_0} \times 10^6 \quad (3.6)$$

where B_0 is the main magnetic field and D_i and I_i are respectively the homogeneous and inhomogeneous components of the BMS shift. This last quantity is more important than the homogeneous one for all but the simplest shapes which implies that BMS shift is generally dependent upon the position within the compartment considered. In the case of the channels of the stereotactic plate, it seems reasonable to assume that the homogeneous component plays the most important role in light of the previous image which demonstrates a distortion effect of greater importance than the dimension of the

channel section, so that one can write $I_i \simeq 0$ and $\delta_x \simeq D_i$.

The previous imaging experiments revealed that the marker distortion was similar along all of the length of the channel, except in the close vicinity of a vertex where the BMS effects become more complicated. This indicates that these channels can be considered as infinite cylinders for the purpose of explaining the misimaging with the help of the BMS concept. Chu provides values for many simple compartments i , most particularly for an infinite cylinder (with or without a surrounding coaxial layer of material) contained in a homogeneous material of infinite extent. For these situations, the BMS shift can be known in any of the compartments in play using an expression involving the volumetric susceptibility of the compartment considered as well as the one of the *other* compartments in the vicinity of the first one. Chu has successfully approximated the infinite cylinder behavior with a length vs diameter ratio of 10 while the marker plate channel has a length vs side ratio of over 40. Also, it was believed that the square section of the channel did not cause the value of δ_x to differ largely from the one of a circular section cylinder. Nonetheless, Fig. 3.13 depicts a more complicated situation since the surrounding acrylic does not assume a coaxial form around the filled channels.

The expression of D_i for an infinite cylinder perpendicular to the main field and surrounded by a coaxial layer of material is expressed by Eq. 3.5. Note the absence from the expression of the susceptibility of the material of the container which is in direct contact with the inner medium. It can be suggested that the behavior of the channel in the top plate which is perpendicular to the main field is close to the situation that satisfies Eq. 3.5. However, it can also be suggested that the particular case of a channel parallel to the main magnetic field is different since it is now along the direction of the magnetization. This appears to be a situation closer to the case of a cylinder in an acrylic environment of large extent, this corresponding to replacing χ_{air} in Eq. 3.5 by the value for the acrylic which is non-zero

It was thus thought that the appropriateness of this hypothesis could be verified

by covering the channels of the top plate with further acrylic in the form of tongues running along one channel, so as to approximate more closely the case of a cylinder perpendicular to the main field and contained in some extended acrylic medium. χ_{air} is then replaced by the same value for acrylic. Compared with the previous figure of $-\chi_1/6$ for the perpendicular channels of plates other than the top one, a difference $\Delta D_1 = \chi/2$, where χ is the susceptibility of acrylic is obtained with this situation. The brand name of the compound used in making the marker plates is Cast Acrylic™ (Polypenco, Guelph, Ont.). This was identified as being methyl methacrylate, a polymer of magnetic susceptibility $\chi = -6.7 \times 10^{-6}$ in MKSA units [110]. Presuming that the content of a covered channel resonates at the nominal resonant frequency ω_0 (just like the channels of the LR and AP plates seemed to do since little distortion was perceived), one could expect a theoretical distortion of $5.5mm$ for a non-covered channel with $FOV = 299mm$ and a readout bandwidth of $36.2Hz/pixel$ (from Fig. 3.14), since $\chi/2 \times 64 \times 10^6 Hz$ translates into $214Hz$, so $5.5mm$. The top plate was prepared in the manner illustrated in Fig. 3.13.

Imaging in the coronal orientation was then performed in order to verify whether any difference in distortion between the covered and uncovered sections could be observed using the subtraction technique. As Fig. 3.14 clearly demonstrates, this was indeed the case and the covered channel hardly exhibits any distortion effect at all. Hence, this signifies that the BMS value of the modified channel is close to the one of the other channels perpendicular to the main magnetic field that were not found to show the distortion effect and were assumed to be in an infinite extent of material. More importantly, this suggests an easy way to remove the unwanted effect and avoid redesigning the plate. It simply consists in covering all the channels of the top plate in a manner similar to that described in Fig. 3.14. Hence, this would extend the immunity against the BMS phenomenon to all channels of the top plate.

So far, only the behavior of the *perpendicular* (with respect to the main field) channels was discussed. However, a more thorough explanation calls for the evaluation of

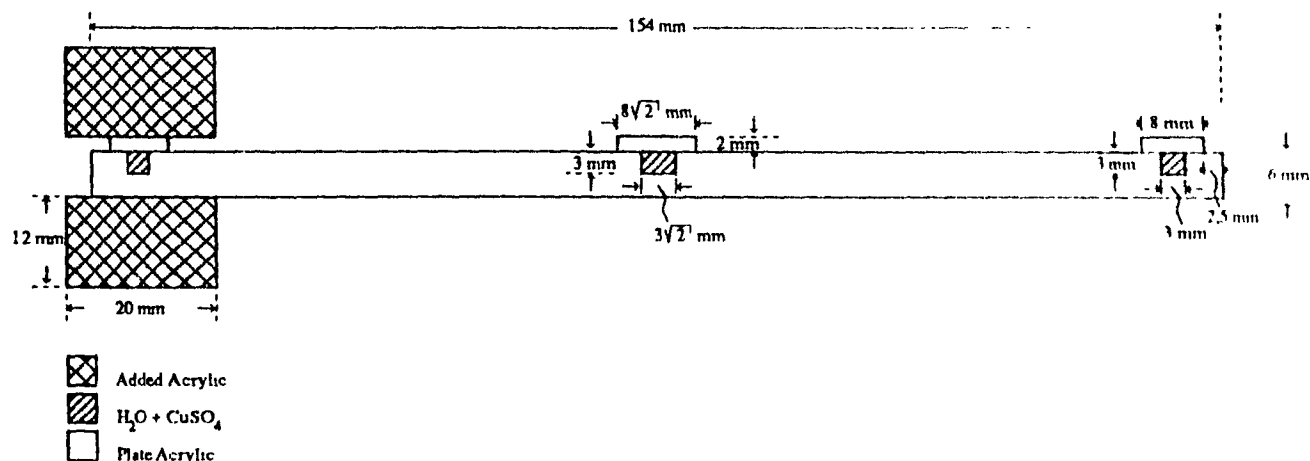


Figure 3.13: Cross section of a modified fiducial marker plate used to verify the influence of some added material on the occurrence of BMS effects. The view is taken at the midplane of the marker plate

the non-occurrence of distortion with the channels *parallel* to B_0 such as all the ones encountered with transverse slices. For such a situation, Eq. 3.4 gives $D_t = \chi_m/3$. Comparing this value with the case of a perpendicular cylinder evaluated by Eq. 3.5, this yields a difference $\Delta D_t = \chi_m/2$ ⁶. Taking -9.1×10^{-6} as the susceptibility of water and a readout bandwidth of 108.6 Hz/pxel , theoretical distortions of 3.1 mm and 2.9 mm , respectively, are obtained for the FOV of Figs. 3.10(A) and 3.10(B), in agreement with the experiments in both cases.

The same evaluations were performed with the FOV and readout bandwidths of Figs. 3.12(B) and 3.14. This yielded 10.9 mm and 7.5 mm respectively, thus again consistent with the actual marker distortion

⁶In fact, a 0.5 mM CuSO_4 solution was used. However, the contribution of this paramagnetic molecule to the overall magnetic susceptibility is negligible at this concentration

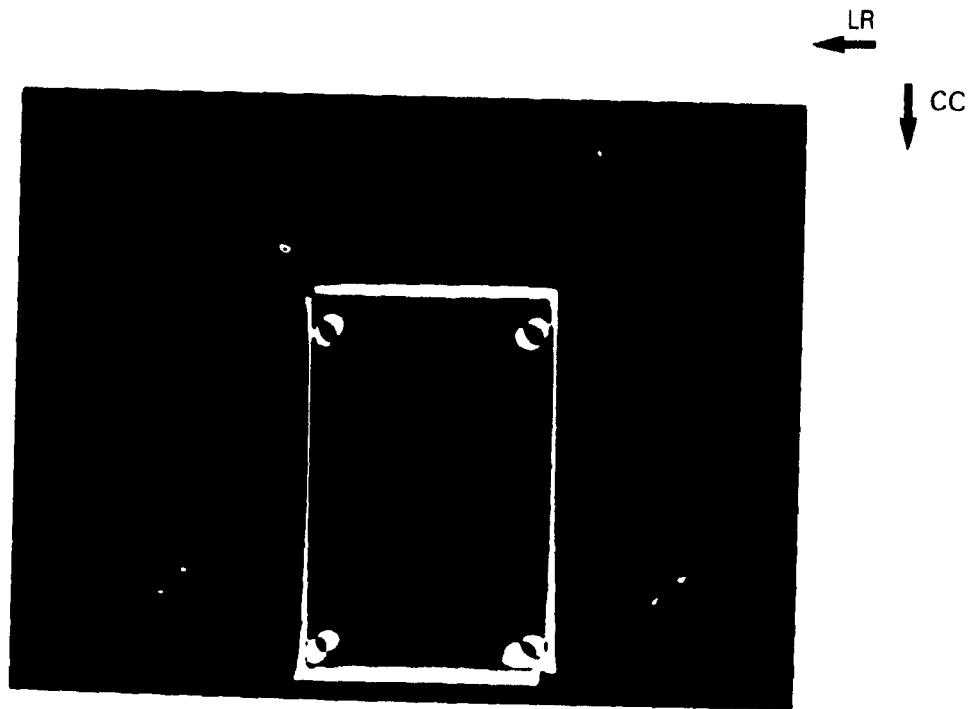


Figure 3.14: Subtraction of coronal images of the stereotactic phantom mounted in the stereotactic frame. A FOV of 239mm with a slice thickness of 2mm were employed, along with a bandwidth of 36.2Hz/pixel. TR= 1000ms and TE= 50ms for both images. One of the channel was covered with acrylic as shown in Fig. 3.13. Distortion has been almost completely removed but some 7mm distortion is present on the 2 other channels. Note that for logistical reasons, the aluminum stereotactic frame was utilized instead of the version made of a composite material that was used for all the previous stereotactic images. This is seen from the distortion at the bottom left and right corners from the presence of the aluminum posts.

3.7 Effect of top plate distortion on accuracy of localization

It is now clear that the accuracy of position calculation in the context of stereotaxy does not depend only upon the geometrical integrity of the patient image but also on the proper positioning of the fiducial markers in this image. However, the problem of a particular type of distortion involving the cranial fiducial marker plate from the presence of BMS effects was raised previously. In order to give some insight into the impact of such misimaging described by the erroneous screen coordinate (u_1, v_1) of the cranial marker in Eq. 3.1, a typical coronal image was chosen and the position of the markers determined with the aid of the MNI stereotactic program. The point $(256, 256)$ ⁷ situated in the middle of the FOV was selected as a reference point and the effect of the plate distortion on the localization of that point was verified.

The effect of a uniform shift of the cranial marker plate, either in the readout or in the preparation direction was verified by simulating with the help of Eq. 3.1, the BMS effect occurring on the top plate. It can be seen that such a shift would be of no consequence on the stereotactic position of the marker plate as described in Section 3.5 since the relative positions of the individual markers are preserved. However, it will obviously change the pixel position within the FOV and a new position $(u_1, v_1, 1)$ will be obtained for the point P_2 of that plate. Moreover, the coordinate axes of the stereotactic system are closely parallel to those of the magnet and the slices used for the purpose of stereotaxy are generally not angled. Hence, the BMS distortion affects only one of the u or v coordinates of the marker. Fig. 3.15 illustrates the consequence of this shift of the marker plate.

Error on slice selection was neglected in Fig. 3.15 since it can easily be circumvented

⁷All stereotactic MRI images are acquired using 256×256 pixels but linearly expanded to 512×512 . Nevertheless, the bandwidth in $Hz/pixel$ refers to the original pixel size, and should consequently be divided by 2 when considering the expanded pixel size.

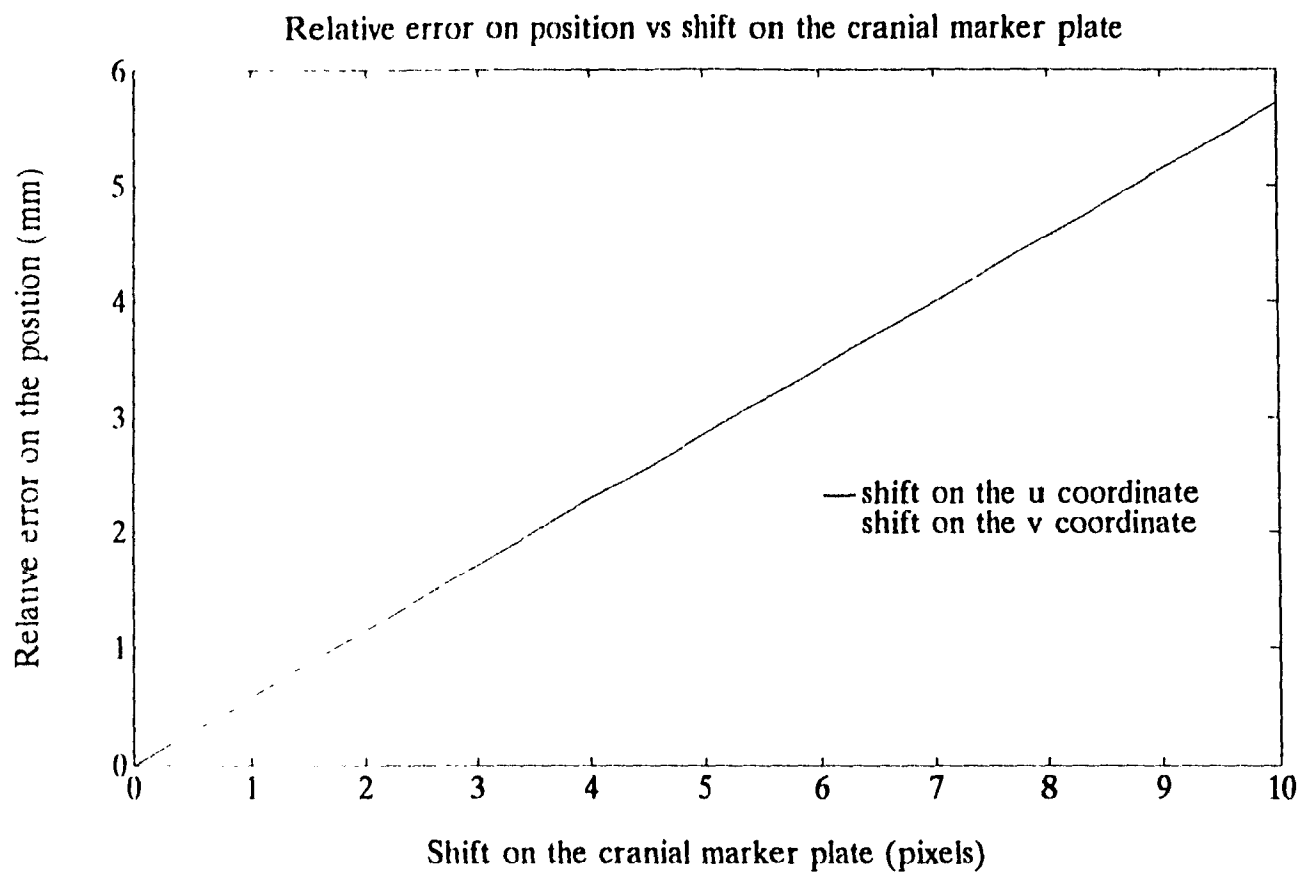


Figure 3.15: Plot of the 3D relative positional error of a point situated at screen coordinates (256, 256) with the use of a shifted cranial marker plate. The error is evaluated with respect to the stereotactic position obtained with unaltered fiducial markers for both possible readout gradient orientations. A 239mm FOV with a slice thickness of 2mm were employed, along with a bandwidth of 36.2Hz/pixel. TR= 1000ms and TE= 50ms.

by the use of thinner slices or 3D FT imaging. New altered cranial marker screen positions $(u', v, 1)$ and $(u, v', 1)$ were introduced with the set of (x_i, y_i, z_i) in order to simulate a horizontal and vertical (LR and CC) readout gradient direction. The relative error on the 3D position with respect to the above reference point was plotted by the shift in pixels.

It is clear that the consequences of an inaccurate localization of the fiducial markers can be quite detrimental to positional accuracy, whether this shift is horizontal or vertical in the image. Since a minimum set of 3 coordinate pairs is used to generate a complete mapping of all (u, v) in terms of (x, y, z) , the relative error on the 3D position differs throughout the FOV, being small in the vicinity of the properly imaged markers but larger close to the distorted ones.

3.8 Conclusion

The inherent distortion of the MRI system was characterized by the imaging of a phantom of known geometry. Inherent distortion was found to be sufficiently important at low gradient strength that neither fiducial markers nor patient anatomy could conserve sufficient geometrical integrity in the MR image to allow for accurate use of stereotaxy. While it appears that the situation would be more satisfactory at high gradient strength for the patient's anatomy, special methods to account for marker distortions still present may be necessary.

It is possible to distinguish between the distinct influences of B_0 inhomogeneities and gradient field non-linearity in the inherent distortion from the occurrence of the former along the direction of the readout gradient. As expected, gradient field non-linearity becomes more evident away from the isocenter. Nonetheless, main field inhomogeneity seems to be the dominant cause of distortion at large distances from this point. Attempts to improve the spatial linearity performance at those distances should therefore focus on that contribution. Furthermore, no dependence of distortion on the echo time could

be demonstrated, which suggests that eddy current effects might only play a limited role in the distortion phenomenon with the imager utilized for the experiments of this work.

Limitation on the positional accuracy in stereotaxy from susceptibility effects, caused by the frame assembly, was shown still to occur despite the use of an aluminum free frame. The origin of the distinct behaviors of the fiducial markers from the point of view of distortion was attributed to bulk magnetic susceptibility characterized by the orientation of the marker plate with respect to the main magnetic field. Its impact on accuracy in the context of stereotaxy was clearly demonstrated. A quantitative explanation of this occurrence was provided, along with an effective and straightforward method to remove it.

Chapter 4

Distortion correction methods

There are numerous ways to approach the problem of distortion. This partly reflects the fact that many factors contribute to this problem, and most correction methods are aimed at reducing, to various extents, the contribution of one or many of these causes. Some of the most representative techniques are described here. This chapter, along with the previous discussion on eddy currents in the Chapter 2, give a broad overview of the many approaches. Chapter 5 is dedicated to a more thorough study of an additional method.

4.1 B_0 inhomogeneity correction using hardware methods

The need to avoid image non-linearity accounts for a large part of the cost of a magnet since a field homogeneity of a few *ppm* is needed over the useful volume. Geometrical distortion of up to $\Delta B/G_{read}$ can be observed in an image whose non-linearity is mainly attributable to main field inhomogeneity represented by ΔB . Since $3mT/m$ is a typical readout gradient strength at $1.5T$, a $6ppm$ inhomogeneity corresponds to a $3mm$ distortion, which is unacceptable in the context of stereotaxy. Section 2.3 has showed that

an increase in G_{read} to minimize the above ratio is a solution whose cost is evaluated in terms of SNR, as shown by Eq. 2.26. Furthermore, the use of a higher gradient strength has other detrimental consequences, such as increased switching time and greater design cost. Consequently, ΔB needs to be reduced to allow the use of narrow bandwidths for optimal image quality.

The development of magnet technology has therefore focused on improving the homogeneity of the main field around the isocenter. Because of finite manufacturing tolerances in the construction process and the possible presence of magnetic material in the magnet's environment [3], an empirical system able to further shim the field of the magnet is needed. At present, two types of such systems are employed to achieve this, namely shimming coils and steel or magnetic elements placed around the magnet bore.

In order to describe the static field in terms of the contribution of many components, decomposition in spherical harmonics is generally used. In this discussion, a spherical coordinate system is assumed. The polar angle θ is measured with respect to the positive z axis direction (generally parallel to the bore axis and the main field direction) whereas the azimuthal angle ϕ is measured from the positive x axis as illustrated in Fig. 4.1. The origin of this spherical reference frame is assumed to lie at the magnet isocenter, close to which most imaging fields of view are centered. One can assume that the resonant frequency is dictated by B_z and write [18]

$$B_z = \sum_{nm} C_{nm} r^n (\text{or } r^{-n-1}) P_{nm}(\cos \theta) \cos m(\phi - \psi_{nm}) \quad (4.1)$$

where C_{nm} and ψ_{nm} are constants and $P_{nm}(\cos \theta)$ is the Associated Legendre function of order n and degree m that satisfy $n \geq m \geq 0$. Shimming methods are intended to cancel out as many of these harmonics as possible, except that of order and degree zero which represents a homogeneous static field. Since spherical harmonics are orthogonal functions, one can modify the influence of one component without modifying the other harmonics.

Many assumptions are useful in simplifying the use of this formalism. For instance, the decomposition of the magnetic field certainly does not include any harmonics con-

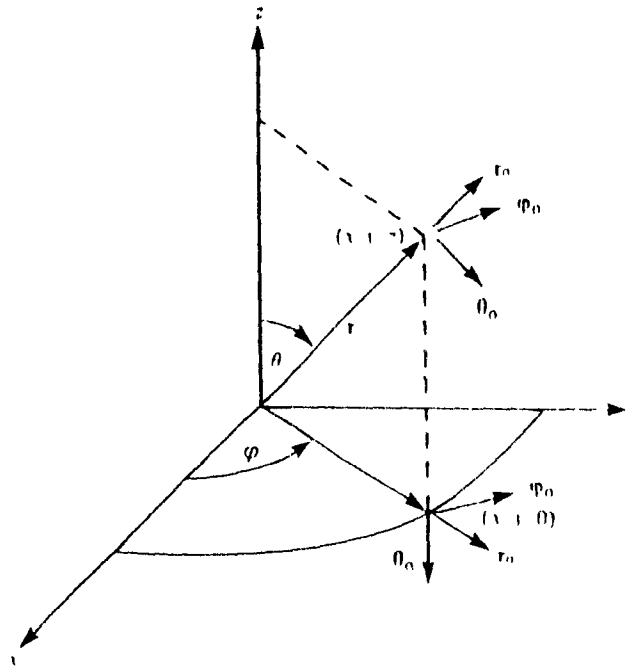


Figure 4.1: Measurement of r , θ and ϕ for a spherical coordinate system

taining r^{-n-1} since no discontinuity in B_z can possibly be present at $r = 0$. Also, one usually considers individually the *zonal* harmonics for which $m = 0$ and the *tesseral* harmonics for which $m \geq 1$. Zonal harmonics are evaluated by an axial (or z axis) field plot. Components up to order 6 are generally sufficient for the evaluation around the isocenter (r to the n^{th} power in Eq. 4.1), although this also implies that this evaluation is defeated at greater distances. It can be seen that the axial field plot does not depend on the influence of the tesseral harmonics since Legendre associated functions always involve a factor $\sin \theta$ which ensures that these harmonics are zero along the z axis. An azimuthal field plot along with Fourier analysis allows the evaluation of the tesseral harmonics. Many elements in addition to those cited above may be utilized as well [18].

Once an adequate description of the static field has been obtained, one must proceed with cancelling out the most important inhomogeneous components about the isocenter. As mentioned above, steel or magnet elements are one such method of shimming the field. The analysis of their effect is facilitated since all but the z component of the field they produce can be neglected in the face of the overwhelming main magnetic field

oriented along the z direction. Generally, their contribution is aimed at eliminating tesseral harmonics ($m \geq 1$) by arranging them in rings perpendicular to the z axis. These rings are intended to eliminate the contribution of the lower orders (remember that $n \geq m$) of the tesseral harmonics of degree such that ($m \leq 5$). The remaining high orders of these first tesseral harmonics can be neglected about the origin due to the role of r^n in Eq. 4.1, and so can be all tesseral harmonics of higher degree.

The cancellation of tesseral harmonics in the manner described above can create important zonal harmonics. Shimming coils can be used to eliminate these zonal harmonics. They are composed of a set of current loops oriented perpendicularly to the bore axis [18,36]. For each set, θ and the direction of the current flow of each loop are chosen so that all orders less than the one the set is intended to adjust and the next higher order of the same parity are not present. Hence, one carries out the cancellation process from low to high orders. Tesseral harmonics can also be created with shimming coils by utilizing configurations of coaxial arcs of current [104]. Note that shimming coils are linked by segments oriented along the z direction, thereby producing no field component in that direction.

4.2 Correction using *a priori* distortion knowledge

The earliest example of distortion correction using *a priori* knowledge of the error field may be Hutchison's method [51]. Unfortunately, it only accounts for intensity distortion expressed by Eq. 2.20, thus leaving the inherent geometrical distortion uncorrected. Lai [64] proposed a curvilinear back-projection technique to handle inhomogeneities when dealing with back-projection reconstruction. However, the form of the point spread function with back-projection reconstruction varies throughout the image plane, which complicates the reconstruction scheme [87].

Kawanaka's first technique fully accounts for the role of ΔB in geometrical and intensity distortion [59]. His method is based on estimating the importance of the

static field perturbation using a phantom composed of many point-like objects of known position. Distortion over the image plane is then interpolated using a 2D polynomial, and the distribution of the static field error can be used with Eq. 2.20 which is applied on the distorted image to allow for the recovery of the spin density distribution. Kawanaka's second technique is an extension of the first but also takes into account gradient field non-linearity [60]. Since the respective contributions of both gradient field non-linearity and static field inhomogeneity need to be known for post-processing to be possible, two rather than one measurements with the same type of phantom are performed, with the roles of the gradients being exchanged in the second acquisition. Yamamoto presented a similar technique to acquire the knowledge of both main field inhomogeneity and gradient field non-linearity with the help of two acquisitions at 2 different readout gradient strengths [122]. O'Donnell [87] also describes a method that account for ΔB and gradient field non-linearity.

Sekihara [107] also devised a correction method accounting for both the intensity and space distortion from main field inhomogeneity. In a second communication [108], he suggests a phase encoding method with non-simultaneous gradient and spin echo formation. Schad handles separately the problems of 2D distortion of the image plane and of tilting of this same plane, the latter of which has been ignored with most of the previous methods [106]. 2D distortion is obtained using a phantom from which the distortion map is interpolated in the same manner as in Kawanaka's technique. Following this, the depth position of the image plane is characterized using a 3D phantom made of a pattern of Z-shaped markers like those found in some stereotactic frames. It is then 2D corrected with the polynomial determined in the first step and processed to yield the geometry of the image plane. Currents in the shimming coils are then adjusted to approach image plane flatness and the scheme is repeated from the 2D phantom acquisition. Two or three iterations are sufficient to obtain an almost flat image plane. The last set of shimming currents is then used for stereotactic imaging.

The previous methods all rely on some distortion knowledge which has to be acquired prior to the acquisition of images in which non-linearity is to be removed. This

implies that the image non-linearity does not change much in time. While this is a reasonable statement when dealing with gradient field non-linearity for all systems and with main field inhomogeneity of superconductive magnets, it is often unrealistic for the inhomogeneity of resistive and permanent magnet systems [3]. An interesting technique that is not affected by this limitation was presented by Jonckheere but concerns only distortions caused by the magnetic components of the stereotactic apparatus. A ring of calibration rods allows "on-line" acquisition of the distortion contribution of these elements, avoiding the need for a supplementary measurement. Distortion of the area in the neighborhood of these rods is then obtained from interpolation.

Nevertheless, this last method does share an important drawback with the previous correction schemes; it fails to correct for magnetic susceptibility effects and chemical shift. These have to be acquired and corrected for each patient, and cannot be obtained with phantom measurements. Moreover, the use of phantom measurements has to be performed carefully to avoid corrupting the distortion field maps with bulk magnetic susceptibility effects that may occur with improperly shaped phantoms.

4.3 Other correction methods

Other ways to correct for MR image non-linearity have also been proposed. Many authors have presented different variants of the so-called phase encoding methods [5,14,83,119]. Applied to imaging, this basically consists of replacing frequency encoding by phase encoding, as illustrated in Fig. 4.2. An oscillating gradient (generally sinusoidal to minimize eddy currents effect) is used along with a series of π pulses applied every time t such that $t = 2n + \tau$.

As one can see, the phase gain from 0 to τ due to inhomogeneities is cancelled out at $t = 2\tau$ by a phase lag of equal magnitude and accumulated between τ and 2τ . On the other hand, the phase gain due to the G_z influence between 0 and τ becomes a phase lag at τ . This lag is then increased between τ and 2τ by the now inverted contribution

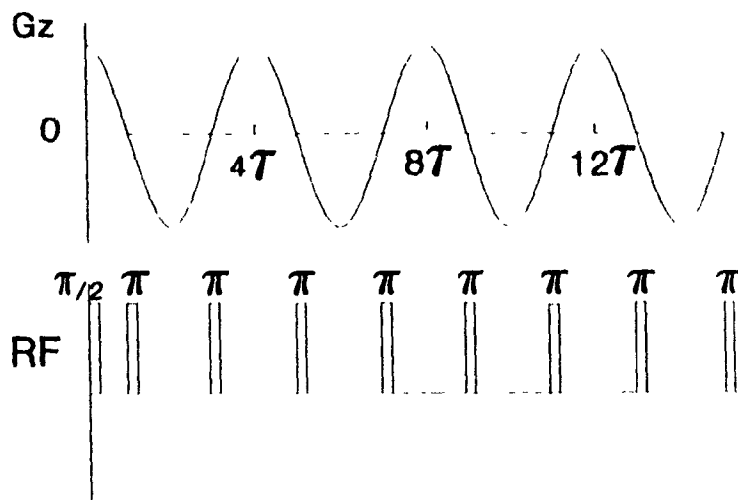


Figure 4.2: Pulse sequence used with the class of MRI distortion correction methods replacing frequency encoding by phase encoding. The alternating gradient illustrated is sinusoidal, but other periodic shapes can be used. The period of G_z is 4τ .

of the gradient. Therefore, it is apparent that the inhomogeneity contribution to phase is eliminated every $2n\tau$ while the contribution of the alternating gradient builds up. If N_z samples are acquired during a total time $2N_z\tau$ in the context of an otherwise conventional 3D Fourier scheme, the contribution of generalized field errors (main field inhomogeneities, magnetic susceptibility and chemical shift) are removed. Note that it was assumed that the changing polarity of the magnetization (every 2τ) is accounted for. Otherwise one has to sample every 4τ .

As Wong has shown, the inhomogeneities that this technique can handle are quite high, typically a few hundred ppm. Nonetheless, it necessitates long imaging times since the sampling period is lower bounded by the duration of the π pulse. Increased RF power can partly circumvent this problem, but patient safety may limit the feasibility of this option because of excessive RF power deposition.

As with Sekihara's and Kawanaka's techniques, Feig uses the knowledge of the static field distortion to compute the Jacobian in Eq. 2.20 and hence accounts for both geometrical and intensity distortions [32,33]. However, he uses an acquisition with non-simultaneous spin and gradient echo to encode the signal with the contribution of the inhomogeneity, eliminating the need for phantom imaging. Cho has also shown a correction technique using view angle tilting. This method accounts for generalized static field inhomogeneities [19].

Chapter 5

Image correction using double-gradient acquisition

In Chapter 2, the contributions of some of the factors playing a role in the occurrence of distortion were evaluated. Main field inhomogeneity was then shown to be the main cause of image non-linearity in areas relatively remote from the isocenter. It was also seen that the methodology for the correction of this problem is the same as for the correction of susceptibility and chemical shift since their overall effect is contained in the Jacobian of Eq. 2.20.

However, the acquisition of the information regarding the static field errors differ when dealing with main field inhomogeneity on one side and susceptibility and chemical-shift effects on the other side since the latter are patient dependent, thus prohibiting the use of *a priori* information about $\Delta B(x, y, z)$. The problem of distortion from susceptibility also includes some effects particular to stereotactic imaging, as exemplified in Chapter 3 of this work, in [27] and in [54]. Nevertheless, even main field inhomogeneity may exhibit some variation in time, the problem being more pronounced with resistive and permanent magnet systems. The use of distortion correction methods relying on *a priori* inhomogeneity information may therefore be even further defeated by this fact. The on-line acquisition of the distortion information is therefore more appropriate to

fully account for generalized static field inhomogeneities.

On the other hand, gradient field non-linearity is a problem that can only be addressed by using warping algorithms. The information related to the gradient field non-linearity needs to be acquired once and does not change afterwards. Some systems already include such correction scheme [47], and this will in all likelihood become generalized. Moreover, geometrical distortion problems associated with eddy currents do not appear to be of major importance with MR imagers such as the one used for the experiments of this work and could conceivably be well taken care of through the use of active shielding, at least until ultra-fast sequences become more popular. Therefore, the problem of generalized static field inhomogeneity is of particular concern when dealing with stereotaxy and it is for this reason that a distortion correction method that could account for it using conventional pulse sequences was sought.

The image post-processing method proposed recently by Chang is satisfactory from this point of view that it allows one to obtain an image free from distortion due to the presence of the term $\Delta B(x, y, z)$ in the spatial description of the magnetic field [16]. In order to perform this post-processing, two input images acquired at two different gradient strengths are needed. This doubles the time required to perform the acquisition. This chapter describes the work that has been performed in order to adapt this method to stereotactic imaging [35]. At the MNI, stereotactic procedures have been performed for many years using a locally developed program that is now available on a commercial basis [93,92]. Consequently, efforts were directed towards creating a program that could be used with the existing software platform.

5.1 Theory

The effectiveness of this double-gradient acquisition method is best demonstrated for a 1D case. When phase encoding is used in the two other directions, generalization is straightforward since immunity of this type of encoding against generalized static

field errors was demonstrated in Chapter 2. The special case of 2D FT method will be discussed in the next section.

Differentiating Eq. 2.19 and using Eq. 2.20, one can write the Jacobian of the transformation using

$$J(x') = 1 + \frac{1}{G_x} \frac{d\Delta B(x)}{dx}. \quad (5.1)$$

Conventional reconstruction schemes assume this Jacobian to be unity and yield a reconstructed profile $\lambda'(x')$ affected by distortion from the presence of the term $\Delta B(x)$. The undistorted profile $\lambda(x)$ is then given by [16]

$$\lambda(x) = J(x')\lambda'(x') \quad (5.2)$$

which is the equivalent of Eq. 2.22. Assuming the gradient field to be perfectly linear, one can consider the acquisition of the two profiles $\lambda_1(x_1)$ and $\lambda_2(x_2)$ with the two gradient strengths G_1 and G_2 respectively. Using Eq. 2.20, $\lambda(x)$ can be expressed from the two distorted profiles by both

$$\lambda(x) = \lambda_1(x_1) \frac{dx_1}{dx} \quad (5.3)$$

and

$$\lambda(x) = \lambda_2(x_2) \frac{dx_2}{dx}. \quad (5.4)$$

Eqs. 5.3 and 5.4 are used to obtain Eq. 5.5 which allows the mapping of each position of one distorted image into the position of the other.

$$\frac{dx_2}{dx_1} = \frac{\lambda_1(x_1)}{\lambda_2(x_2)} \quad (5.5)$$

Since Eq. 5.5 is differential, this mapping is allowed provided that one such pair of corresponding positions is known. Also, Eq. 5.5 shows that B_0 inhomogeneity implies the presence of intensity distortion.

It is now interesting to look at the case of a single spin situated at x . Using a gradient strength G_1 , the actual position x of the spin can be written in terms of the apparent one x_1 with the help of Eq. 2.19 as

$$x = x_1 - \frac{\Delta B(x)}{G_1}. \quad (5.6)$$

Similarly, one can write for the profile acquired with G_2

$$x = x_2 - \frac{\Delta B(x)}{G_2}. \quad (5.7)$$

Writing $\alpha = G_1/G_2$, this last pair of equations can be used to obtain the position of the spin in a distortion free image from its apparent positions in the two distorted profiles and without any knowledge of $\Delta B(x)$. If one combines Eqs. 5.6 and 5.7 and eliminates $\Delta B(x, y, z)$, it follows that

$$x = \frac{\alpha x_1 - x_2}{\alpha - 1}. \quad (5.8)$$

Eq. 5.8 can be differentiated and Eqs. 5.3 and 5.4 substituted, thereby yielding

$$\lambda(x) = (1 - \alpha) \frac{\lambda_1(x_1)\lambda_2(x_2)}{\lambda_1(x_1) - \alpha\lambda_2(x_2)} \quad (5.9)$$

With Eqs. 5.5, 5.8 and 5.9, it is possible to obtain $\lambda(x)$ from $\lambda_1(x_1)$ and $\lambda_2(x_2)$. In order to do this the correspondence between the positions in the distorted profiles is first established with the help of Eq. 5.5. Following that, the positions in $\lambda(x)$ corresponding to the homologous positions in $\lambda_1(x_1)$ and $\lambda_2(x_2)$ are found using Eq. 5.8. Finally, $\lambda(x)$ is evaluated for all x with the help of Eq. 5.9.

Nonetheless, there are limits to the size of distortion that this method can handle, or more precisely to the size of the gradient $d\Delta B(x)/dx$ that can be tolerated. This limit is simply that the readout gradient G_x be chosen so that

$$\left| \frac{d\Delta B(x)}{dx} \right| < \min(G_x, \frac{G_x}{\alpha}) \quad (5.10)$$

everywhere within the FOV, or otherwise there will be a non-unique correspondence between the frequency and the coordinate along the readout gradient direction. Such an occurrence is illustrated in Fig. 5.1 where Inequality 5.10 is defeated between the local maximum and the local minimum.

5.2 Effect of slice selection

Using frequency encoding along with phase encoding in the two other directions allows the direct application of this method to MR imaging using a conventional 3D FT

Magnetic field vs readout position

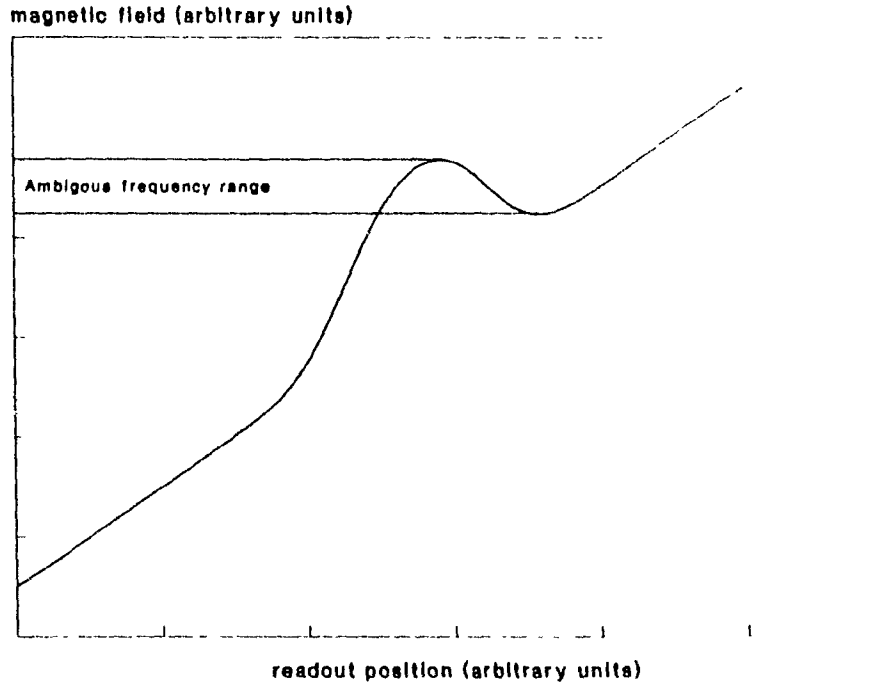


Figure 5 1: Example of distortion phenomenon for which $d\Delta B(r)/dr$ is larger than the readout gradient strength. This yields ambiguous frequency components that can be assigned to more than one position.

method. Assuming x to lie along the readout gradient direction and y, z to be the phase encoding directions, one simply applies Eqs. 5.5, 5.8 and 5.9 to the stack of voxels at (y, z) in the first and the second volume. Performing that for each pair (y, z) allows for the complete recovery of the undistorted image intensity for the whole volume. On the other hand, the use of a 2D FT multiple slices method introduces an error along the slice selection direction (slice non-planarity) on top of the error along the readout gradient direction. Assuming the slice selection to be along the z direction, the expression of the Jacobian is no longer given by Eq. 5.1, but rather by

$$J(x_1, y_1, z_1) = 1 + \frac{1}{G_x} \frac{\partial \Delta B(x, y, z)}{\partial x} + \frac{1}{G_z} \frac{\partial \Delta B(x, y, z)}{\partial z} \quad (5.11)$$

where G_x and G_z are the readout and slice selection gradient strengths respectively since an additional component $\Delta B(x, y, z)/G_z$ is added to the overall distortion. Therefore,

the geometrical distortion in the presence of erroneous slice selection is described by

$$\mathbf{r}' - \mathbf{r} = \frac{\Delta B(x, z)}{G_x} \mathbf{i} + \frac{\Delta B(x, z)}{G_z} \mathbf{k} \quad (5.12)$$

where \mathbf{r}' is the distorted position vector, \mathbf{r} is the actual position vector, G_x is the phase encoding gradient strength and \mathbf{i} and \mathbf{k} are the unit vectors respectively oriented along the x and z directions. For simplicity, the phase encoding position is ignored in Eq. 5.12.

In these conditions, the simple application of the double-gradient method along the readout gradient direction is no longer exact. It is then instructive to examine the generalization of this technique to the 2D FT multiple slice method. With the use of slice selection rather than phase encoding in the z direction, the distortion vector $\mathbf{r}' - \mathbf{r}$ lies in the xz plane. If one chooses a new system of coordinates (x_2, y_2, z_2) such that the x_2 axis is parallel to the vector $\mathbf{r}' - \mathbf{r}$, one can rewrite Eq. 5.12 and obtain a form homologous to Eq. 2.19 (the vectorial notation is dropped since the distortion is again oriented along one coordinate axis)

$$x_2' = x_2 + \Delta B(x_2) \sqrt{\frac{1}{G_x^2} + \frac{1}{G_z^2}} \quad (5.13)$$

where x_2' is the distorted coordinate and x_2 is the original coordinate. If one acquires the two required images with the set of gradient strengths G_x, G_z for the first image along with $G_x/\alpha, G_z/\alpha$ for the second image, both acquisitions share a common x_2 axis as determined above. This makes it possible to use Eqs. 5.5, 5.8 and 5.9 along this x_2 axis. Chang [17] has successfully applied the method to 2D FT images using this approach.

Nevertheless, it is interesting to evaluate the consequences of ignoring the influence of the slice selection gradient despite its role and obtain some insight into the consequences of using the method along the readout gradient direction. Taking Eq. 5.11, the equivalent of Eq. 5.2 with slice selection is

$$\rho(x, z) = \left[1 + \frac{1}{G_x} \frac{\partial \Delta B(x, z)}{\partial x} + \frac{1}{G_z} \frac{\partial \Delta B(x, z)}{\partial z} \right] \rho_1(x_1, z_1). \quad (5.14)$$

The second acquisition is performed with a readout gradient strength of G_x/α , in which

case $\rho(x, y, z)$ is given by

$$\rho(x, z) = \left[1 + \frac{\alpha}{G_x} \frac{\partial \Delta B(x, z)}{\partial x} + \frac{1}{G_z} \frac{\partial \Delta B(x, z)}{\partial z} \right] \rho_2(x_2, z_1). \quad (5.15)$$

From Eqs. 5.14 and 5.15, it is seen that the approximation of ideal slice selection can be made if

$$\min \left(\frac{1}{G_x} \frac{\partial \Delta B(x, z)}{\partial x}, \frac{\alpha}{G_x} \frac{\partial \Delta B(x, z)}{\partial x} \right) \gg \frac{1}{G_z} \frac{\partial \Delta B(x, z)}{\partial z}. \quad (5.16)$$

5.3 Miscellaneous considerations

This section presents some other considerations of importance in the application of Chang's technique that were dealt with in the course of the development of the adaptation presented in this chapter. Furthermore, the most important details necessary for such an adaptation are outlined.

5.3.1 Image intensity normalization

In order to enounce more simply the considerations at the basis of imaging in non-ideal conditions, C in Eq. 2.17 was presented as a constant. In reality, the situation is not as simple and C does in general vary. Even though this primarily depends on the nature of the object that is being imaged, it was experienced in the course of this work that it could also change for a same object imaged at different readout gradient magnitudes, especially when large static field distortions are present.

The explanation for this lies in Eq. 5.5 that demonstrates the inherent character of intensity distortion along with geometrical distortion, also expressed by the conservation of the quantity $\int_{\mathcal{O}} i(u, v) du dv$ where \mathcal{O} is the extent of the object in the image and u and v are the pixel coordinates [34]. At identical density and relaxation characteristics, areas where physical pixels are "squeezed" in the image correspond to the presence of a term $\nabla[\Delta B(x, y, z)]$, the "distortion gradient", whose component along the readout direction is in a sense opposite to the readout gradient. Hence, pixels corresponding

to these areas have a greater intensity than pixels where the distortion gradient is zero along the same direction. Conversely, areas where the two above gradients are in the same sense correspond to areas where physical pixels are "stretched" in the image and where a smaller intensity is found. When the reconstruction algorithm assigns the largest available gray scale value to a pixel situated in an area where the readout gradient G_1 and the readout component of $\nabla[\Delta B(x, y, z)]$ are opposite to each other, the same acquisition performed with G_2 such that $G_1 > G_2$ also assigns the maximum gray scale value to the pixel corresponding to the same physical position. However, this area shows a relatively brighter intensity since $G_1 > G_2$ implies that the second image is more vulnerable to the distortion. Hence, the new image will be normalized so that the quantity $\int_{\mathcal{O}} i(u, v) du dv$ is smaller than the corresponding value in the image acquired with G_1 .

It is helpful to introduce the normalization constants N_1 and N_2 that account for the variability of C as described above. Therefore, it can be seen from Eq. 2.21 that Eqs. 5.3 and 5.4 should have been written

$$\lambda(x) = \lambda_1(x_1) \frac{dx_1}{dx} N_1 \quad (5.17)$$

and

$$\lambda(x) = \lambda_2(x_2) \frac{dx_2}{dx} N_2 \quad (5.18)$$

to yield

$$\frac{dx_1}{dx_2} = \frac{\lambda_2(x_2) N_2}{\lambda_1(x_1) N_1} \quad (5.19)$$

rather than Eq. 5.5.

The algorithm presented here handles this problem by first determining the boundary of the object in the FOV for each input image. This being known, the sum of all object pixels belonging to each image (equivalent to $\int_{\mathcal{O}} i(u, v) du dv$) is obtained. The ratio of both sums is finally multiplied by the intensity of all pixels of the image yielding the greater sum so that the value of $\int_{\mathcal{O}} i(u, v) du dv$ for both images become equal. In these conditions, Eqs. 5.5, 5.8 and 5.9 can be used.

5.3.2 Repositioning of the fiducial markers

Since geometrically accurate MR images are primarily required for stereotactic applications, any approach to distortion removal should be able to cope with the presence of fiducial markers within the field of view. However, these markers are generally small and separated from the imaged object so their accurate localization might suffer from digitization errors associated with an approach such as Chang's algorithm [16]. Consequently, it was found that the use of this algorithm with stereo¹ xy should preferably be carried out by handling the treatment of these fiducial markers separately. In order to do this, the distortion for each marker is assumed to be homogeneous, implying that the static field distortion is constant over the extent of the marker¹. Note that this assumption is not defeated by the problem of bulk magnetic susceptibility effects raised in the Chapter 3 since it appeared to be dominated by a homogeneous distortion effect.

This therefore eliminates the importance of intensity distortion and the correction of the fiducial markers only requires the use of Eq. 5.8 to reconstruct the marker position in the final image. The localization of the marker center is a problem handled by using a semi-automated approach that has already been implemented in some stereotactic software [43]. Firstly, this consists of obtaining the approximate marker position (U_0, V_0) with the help of a mouse. A 7×7 pixels square centered at this point is then searched in order to find the highest intensity pixel. Last, the centroid² of the 5×5 pixels square centered at this last point is used to obtain the position (U_m, V_m) of the marker. This next step consists of applying

$$U_m = \frac{1}{N} \sum_{i=U-2}^{U+2} \sum_{j=V-2}^{V+2} i\sigma(i, j) \quad (5.20)$$

and

$$V_m = \frac{1}{N} \sum_{i=U-2}^{U+2} \sum_{j=V-2}^{V+2} j\sigma(i, j) \quad (5.21)$$

¹As illustrated in Fig. 3.13, the side channel section is 3mm.

²Analogous to the concept of center of mass with this last quantity being replaced by image intensity.

where

$$N = \sum_{i=U-2}^{U+2} \sum_{j=V-2}^{V+2} \sigma(i, j) \quad (5.22)$$

and $\sigma(i, j)$ is the image intensity at pixel (i, j) .

Assuming that the readout gradient direction lies along the U axis and that 3D FT imaging is used, the final position of a given marker can be recovered through the application of Eq. 5.8 where x_1 and x_2 are replaced by Eq. 5.20 applied on the images acquired with readout gradient strengths G_1 and G_2 respectively. Nevertheless, the fractional part of U_n and V_n is significant and is advantageously carried along in the application of Eq. 5.8. It is then acceptable to round off the result to the nearest integer. A 3×3 matrix centered at the calculated position is finally overlaid in the final image. This scheme is repeated for all markers prior to any other processing step and requires the user to perform the markers designation in the same order for both images.

The current version of the stereotactic software used clinically at the MNI carries out an automated search of the fiducial markers in the image prior to stereotactic analysis. However, the process is sometimes unsuccessful, in which case user's guidance is required. It was found that the markers of the images processed as described above are easily localized by the stereotactic software.

5.3.3 Application of the differential equation

As mentioned earlier, Eq. 5.5 can be solved only with the help of an initial boundary condition. Since this process needs to be repeated for each of the image lines, the obvious solution to the problem is the use of the object boundary [16]. Out of the 128 levels of gray available with the image format utilized by this program, the threshold 30 was found to be generally appropriate, although this choice is not critical. The localization of the image boundary in both input images is restricted to an area comprised within the fiducial marker ring.

Although Eqs. 5.5, 5.8 and 5.9 are exact, they obviously need to be applied with a

knowledge of the intensity profile which is discrete in nature. Thus, numerical methods are required. Eq. 5.5 constitutes the basis of the application of the distortion correction method described in this chapter. It expresses the problem of determining for one input image the corresponding position in the other. In general, the calculated position will be real, and its fractional part should be carried along to allow greater precision. For clarity, Eq. 5.5 can be written

$$\frac{dx_2}{dx_1} = f(x_1, x_2) \quad (5.23)$$

with

$$f(x_1, y_2) = \frac{\lambda_1(x_1)}{\lambda_2(x_2)}. \quad (5.24)$$

A basic numerical method to solve Eq. 5.23 is called Euler method. It consists of determining the position x_2^i corresponding to a position x_1^i for all i using

$$x_2^{i+1} = x_2^i + hf(x_1^i, x_2^i). \quad (5.25)$$

h is called the step size and represents the minimum distance in x_1 . However, it is recognized as being too crude an approximation in many instances [4].

A more satisfactory avenue is the fourth order Runge-Kutta method. In applying this solution to the current problem, one has the following rather than Eq. 5.25 [56]

$$x_2^{i+1} = x_2^i + \frac{1}{6}[k_0 + 2k_1 + 2k_2 + k_3] \quad (5.26)$$

where

$$\begin{aligned} k_0 &= hf(x_1^i, x_2^i), \\ k_1 &= hf(x_1^i + \frac{h}{2}, x_2^i + \frac{k_0}{2}), \\ k_2 &= hf(x_1^i + \frac{h}{2}, x_2^i + \frac{k_1}{2}), \\ k_3 &= hf(x_1^i + h, x_2^i + k_2). \end{aligned} \quad (5.27)$$

Computing time increases with the use of a smaller step size h evaluated in pixels. Nevertheless, the knowledge of the intensity is provided for each pixel, which limits the gain that can be achieved with the use of a smaller h . $h = 0.2$ was used with all the processed images.

5.4 Algorithm

The implementation of this method was performed on the workstation currently used at the MNI for stereotactic planning [93]. It consists of a 80386 based computer provided with a 80387 math coprocessor and runs at 20 MHz clock speed. Special features are the support of two supplementary monitors for conventional images display in the first case and stereoscopic images display in the second [44]. Also provided are a tape drive for loading scanner or DSA images along with a printer for image hardcopy. MR images are displayed at 7 bits depth.

The implementation of the distortion algorithm was built around the existing set of stereotactic utility programs for image display and mouse control. Therefore, 1600 lines of code written using the C programming language were sufficient to implement this algorithm. Each pair of 3D FT images requires between 3 and 5 minutes to be processed using the hardware mentioned earlier. Beside accessory input-output control sequences, the program includes the following steps.

1. Pre-processing

Marker position entering The user enters the position of the fiducial markers for both input images with the help of a computer mouse. For consistent association of each marker in both images, the same order of entering needs to be used.

Adjustment of marker position The entered positions of the markers are corrected using Eqs. 5.20 and 5.21, as previously described.

2. Processing

Object boundary determination Each of the 2 input images is searched for its boundary along the readout gradient direction. An intensity threshold value provided by the user is utilized for this purpose. Starting from one of

the edge of the image in the readout gradient direction, the first pixel to show a greater intensity than this threshold is chosen as being a boundary pixel. The search field is restricted to an area comprised within the ring formed by the fiducial markers.

Calculation of the intensity integral The value of $\int_{L_i}^{H_i} \sigma_i(x, y) dx, dy$ where L_i and H_i are respectively the lower and higher boundary (or x position) of the object in the readout gradient direction for image i are obtained for image $i = 1$ and $i = 2$. Assuming that this value is higher for image $i = 2$, a new image $\sigma'_2(x_2, y)$ is calculated using

$$\sigma'_2(x_2, y) = \sigma_2(x_2, y) \frac{\int_{L_1}^{H_1} \sigma_1(x_1, y) dx_1}{\int_{L_2}^{H_2} \sigma_2(x_2, y) dx_2} \quad (5.28)$$

Determination of the homologous pairs Using the initial correspondence provided by the object boundary determination, Eq. 5.5 is solved by associating a position x_2 to every pixel in image 1. This is done with the help of Eq. 5.26. The same process is repeated to obtain this correspondence in image 1 for every pixel of image 2, the role of x_2 and x_1 being inverted. Note that the calculated position carries the fractional part. For each calculated position, the local intensity is obtained by linear interpolation between the 2 adjacent pixels.

Undistorted image intensity For each pair of homologous input image positions, the intensity of the corresponding point in the distortion free image is calculated through Eq. 5.9.

Undistorted image position For each pair of homologous input image positions, the position of the corresponding point in the distortion free image is calculated through Eq. 5.8.

Sorting of final points Since the above steps are performed twice by exchanging the role of x_1 and x_2 , 2 groups of final points are obtained and this set needs to be sorted by position. The "Quicksort" sorting function is used for

this purpose ³.

Interpolation at integer sites The sorted positions (real values) with their intensity need to be interpolated at integer sites in order to obtain the final image.

3. Post-processing

Fiducia¹ markers placement The positions of the fiducial markers in the final image are calculated with the help of Eq. 5.8. The result is rounded off to the nearest integer and a 3×3 matrix centered at this integer is overlaid on the final image.

Final image interpolation The final image is linearly expanded from a 256×256 size to a 512×512 size.

5.5 Experimental results

5.5.1 Evaluation of image accuracy using stereotaxy

In order to validate the efficiency of the distortion removal algorithm, one needs to use a phantom of known geometry. The phantom described in Fig. 3.8 appears to be satisfactory since its images show a pattern of holes that can be used as landmarks. Moreover, it was designed and built to fit in the OBT stereotactic frame in use at the MNI, thus allowing position validation of images acquired in the presence of the stereotactic frame with the help of the current stereotactic analysis system.

Chang has already demonstrated the effectiveness of the technique for non-linear experimental images of phantoms exhibiting sharp contrast edges with an otherwise homogeneous density [16,17]. However, for the validation of the accuracy of the processed image it was desirable to obtain a lower contrast, a case closer to the appearance of

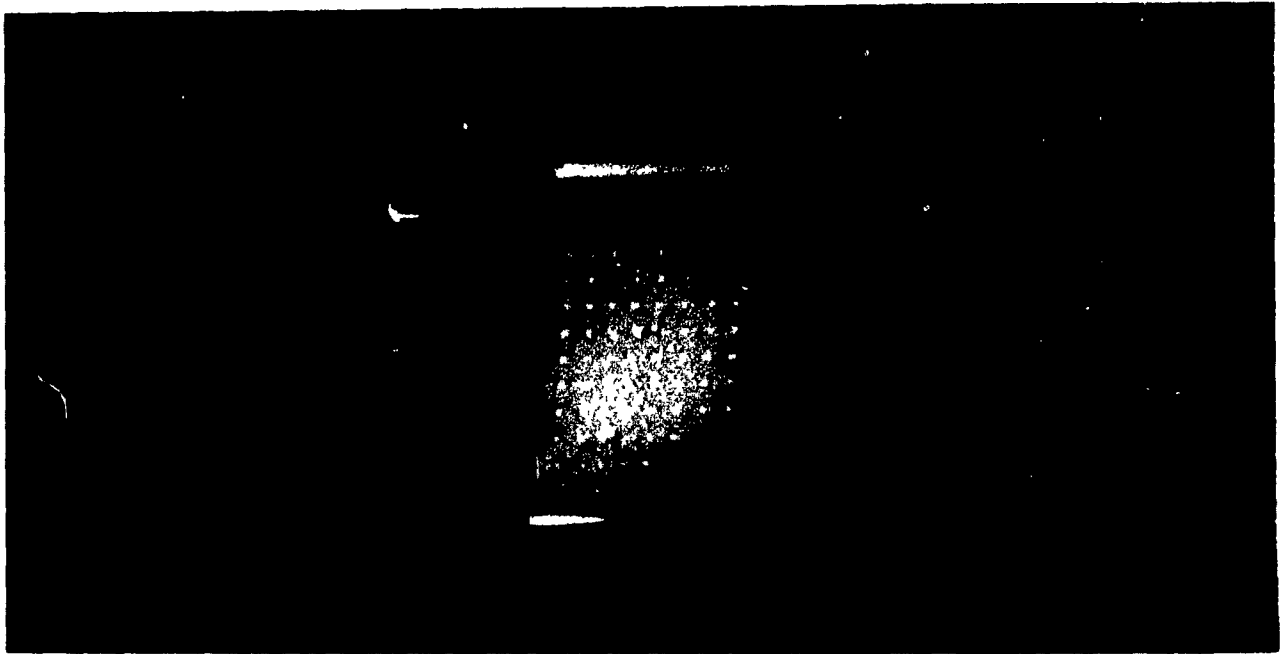
³It is a standard function with the ANSI version of C.

small structures in the brain. A slice thickness of $3mm$ was therefore utilized while the plate thickness is only $1.5mm$ in order to lower the contrast through partial volume effect. Fig. 5.2 illustrates the two input images fed into the program for processing. In order to create some obvious distortion, the shimming coils were turned off during the acquisition of the two input images.

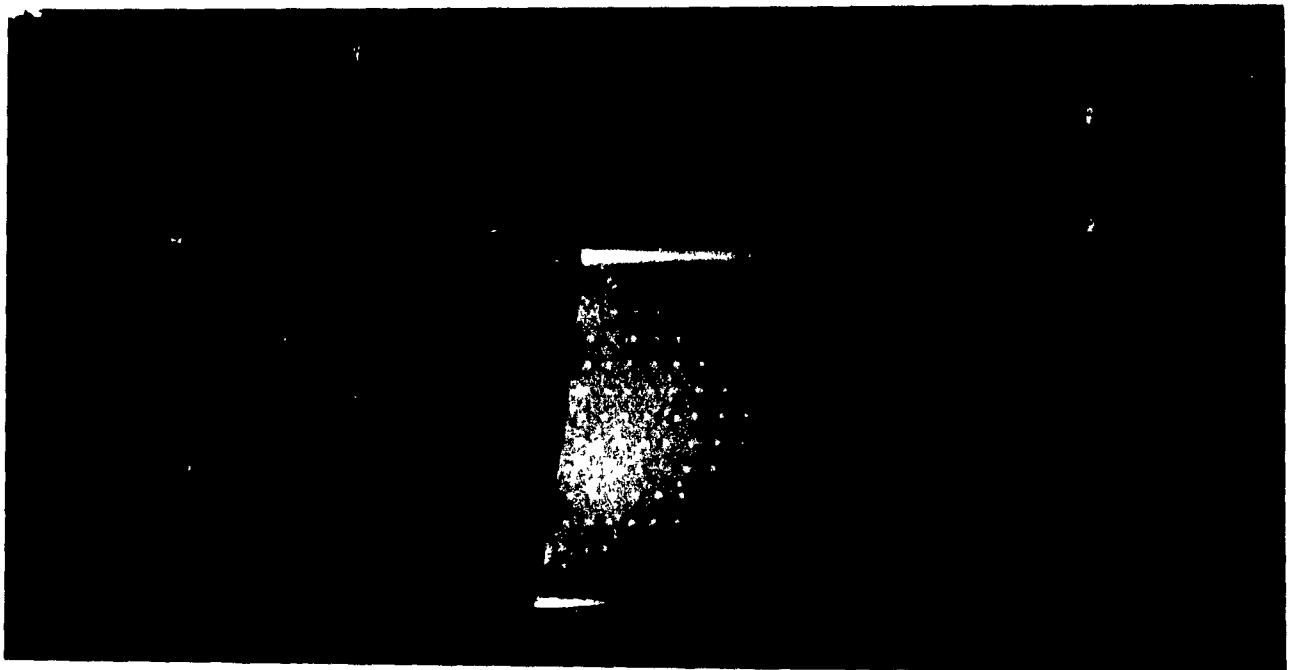
The algorithm relies on $\Delta B(x, y, z)$ to be constant for the acquisition of both input images. Since this parameter depends on the value of ω_0 obtained during the preparation sequence before each acquisition, its determination was inhibited prior to the scan from which the second image of this pair was obtained. Considering the images A and B of the phantom placed in the stereotactic frame as images 1 and 2 respectively, the ratio α to be introduced in Eqs. 5.8 and 5.9 is 1.67. The step size was chosen as $h = 0.2$ and the threshold for boundary determination was taken as 30. The image was processed in the left to right order. Since the shimming coils were turned off, both the phantom and the fiducial markers show some important distortion effect.

The image A of Fig. 5.3 shows the processed image from the two input images of Fig. 5.2. Although the numerical nature of the process introduces apparent digitization errors (discussed in the next section), the image integrity has been recovered, as demonstrated by the now regular appearance of the hole pattern. The fiducial markers have also been repositioned in a way that appears appropriate since the markers that are part of the same plate are colinear. As mentioned earlier, their new positions were calculated with Eq. 5.8 and the markers were drawn in the new image. The lower image in Fig. 5.3 shows the result of the subtraction between the processed and the less distorted ($72.4Hz/pixel$) image.

Nevertheless, a quantitative validation is in order. Since it is generally recognized that the purpose of obtaining geometrically accurate images lies in stereotaxy, it was felt that this quantitative evaluation of the image accuracy should be made using stereotactic techniques which allow the evaluation of the accuracy of the marker repositioning as well.



A

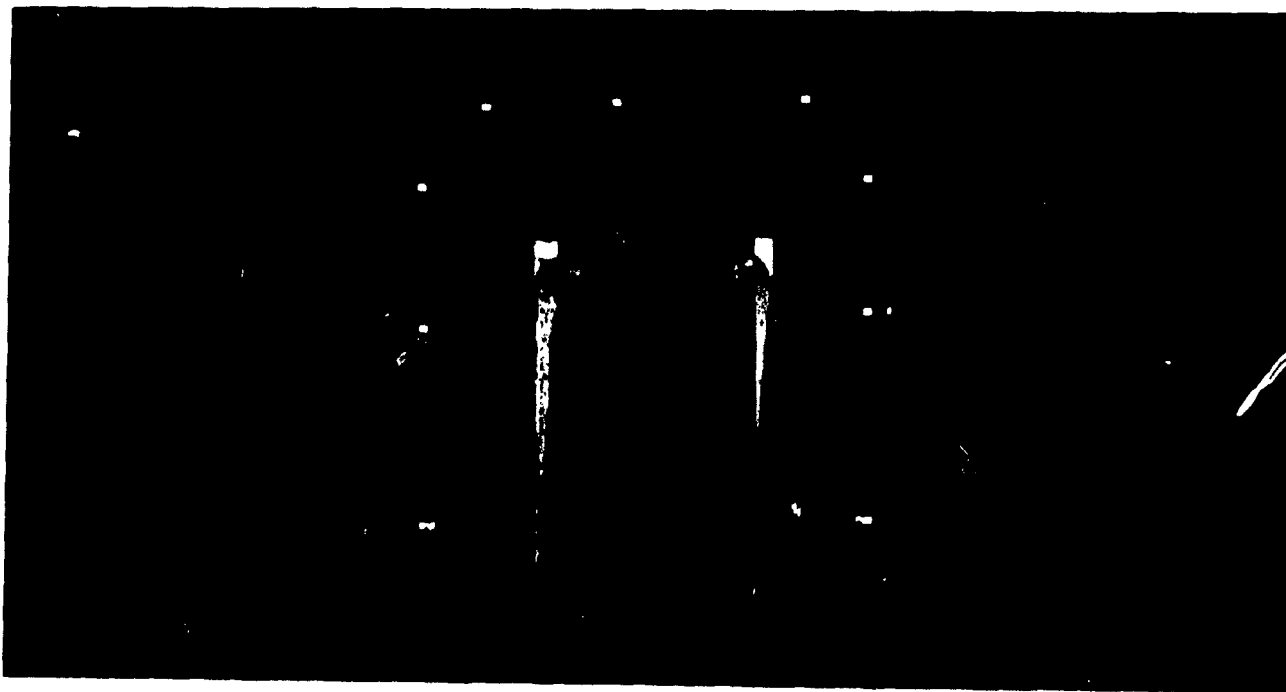


B

Figure 5.2: A pair of input images for the distortion correction program. They were acquired using a 3D FT method with $TR=200ms$, $TE=50ms$, $FOV=300mm$, $th=3mm$ and $n=25$. The shimming coils are turned off so important distortions are visible in the readout gradient direction (horizontal). The readout bandwidth was $72.4Hz/pixel$ for (A) and $43.4Hz/pixel$ for (B).



A



B

Figure 5.3: (A) Result of the processing of the two images in Fig. 5.2. (B) Subtraction of (A) above with Fig. 5.2(A).

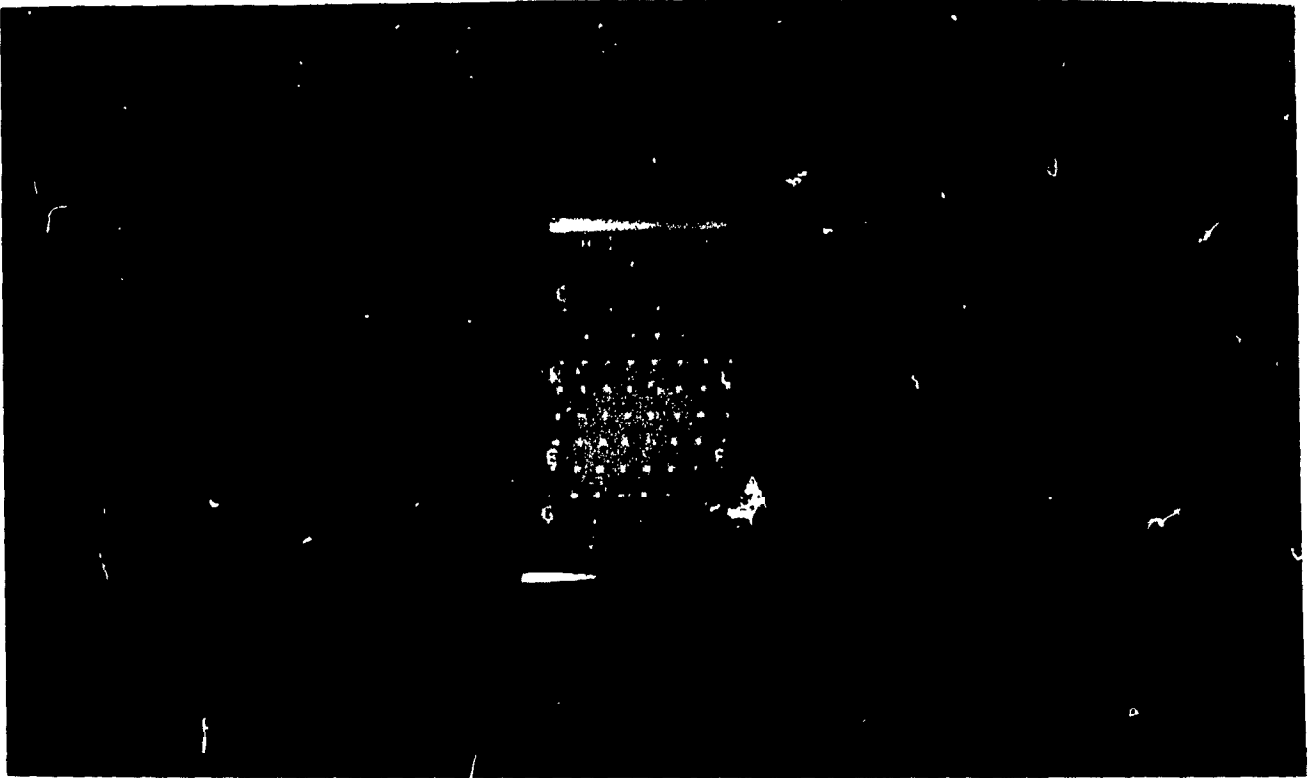


Figure 5.4: Points used for distance evaluation

Relative distances were evaluated between many pairs of points in the phantom using the distance measuring function that is part of the Montreal Stereotactic Planning System [27]. True distances are easily obtained by counting the number of holes separating the two points considered along both phantom axis with the knowledge that the separation between any closest neighbors is 1cm . Fig. 5.4 illustrates the choice of the points that were utilized for relative distance evaluation. The values of the separations are contained in Table 5.1.

Table 5.1 demonstrates the improvement of the image linearity. When significant discrepancies are present between the actual value and the distance measured on the image acquired with a $72.4\text{Hz}/\text{pixel}$ readout bandwidth, those discrepancies increase when considering the image acquired at $43.4\text{Hz}/\text{pixel}$. This is consistent with the presence of static field errors.

Segment	Separation $\pm 0.1cm$			
	43.4Hz/pixel	72.4Hz/pixel	Processed	Actual
AH	12.4	12.0	11.6	11.7
BG	11.5	11.6	11.8	11.7
CF	9.8	9.5	9.3	9.2
DE	9.7	9.8	10.0	9.9
IJ	11.1	11.1	11.0	11.0
KL	7.2	7.0	7.0	7.0

Table 5.1: Validation of the effectiveness of the algorithm. The various distances were provided with the help of the stereotactic software and thus also reflect the correct placement of the fiducial markers.

5.5.2 Digitization errors

Although it is clear that important distortions of the image can be removed using this algorithm, some loss in image quality is present. The most noticeable unwanted feature may be the right edge of the processed image which is jagged rather than straight. The left edge did not suffer from such effect as it constitutes the point from which the reconstruction starts, with the help of the boundary condition. These problems were also met by Chang with his phantom images. However, it is not possible to verify whether his treatment was able to handle low contrast details, as those present in the images herein, since he only presented high contrast experimental images.

It is believed that some of the current limitation on image quality can be attributed to the numerical application of exact equations, that is Eqs. 5.5, 5.8 and 5.9. This causes digitization errors to be present in the final image. Moreover, the processing utilized to obtain the final image involves the use of *two* input images, this increasing the vulnerability toward this type of error.

A first instance of digitization error is found in the use of a limited number of gray scale steps. The Montreal Stereotactic Planning system presently uses 7 bits to characterize the intensity of the images from all modalities. However, the S15HP MR scanner used at the MNI can provide up to 12 bits of information regarding this

parameter. This consequently increases even further the importance of the limitation brought by the digitization of the image intensity.

In order to verify the importance of the low number of gray scale steps, the depth of the images of Fig. 5.2 was brought down to 6 bits and the new input images were used for the distortion treatment algorithm. The result of the processing is presented in Fig. 5.5(A). It can be seen that the importance of the jagged edge effect has increased. Moreover, the circularly shaped voids that correspond to the 4 plexiglas posts holding the plate assembly have suffered from an increased occurrence of digitization errors. It therefore seems that the importance of the gray scale width calls for the use of this algorithm with greater depth images, particularly at the site of sharp intensity gradients. Nonetheless, smoother areas of the image remain basically unaffected by this change.

Fig. 5.5(B) illustrates this last point well. This time, the input images were smoothed with a 3×3 blurring mask such that at each point, the modified intensity $\sigma'(U, V)$ was obtained from the original $\sigma(U, V)$ through the application of

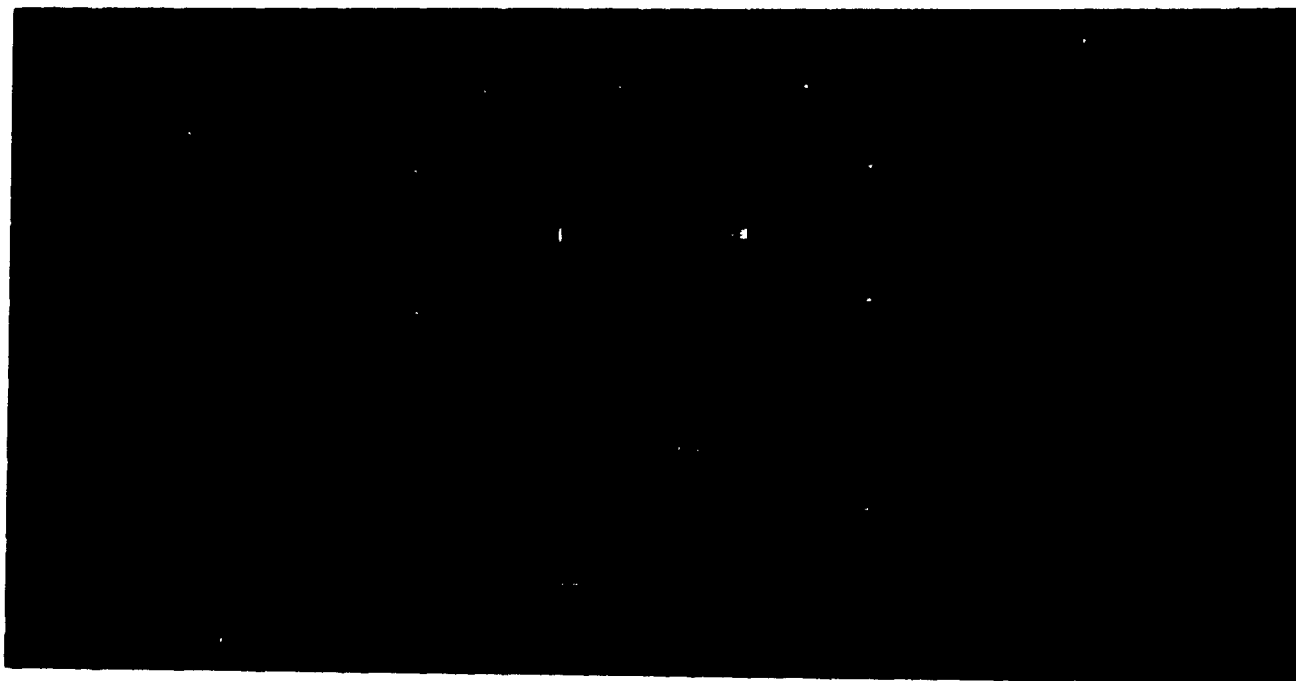
$$\sigma'(U, V) = \frac{1}{9} \sum_{i=U-1}^{U+1} \sum_{j=V-1}^{V+1} \sigma(i, j) \quad (5.29)$$

thus smoothening the intensity gradient at every point. The improvement on the accurate definition of boundaries is seen well.

Another limitation in the numerical adaptation of Eqs. 5.5, 5.8 and 5.9 is the fact that the knowledge of $\sigma(x, y)$ is only provided for every pixel. For instance, it was seen previously that in order to deal with this problem, the calculated centroid of the fiducial markers must carry the fractional part since merely rounding off the coordinates of the centroid position causes the fiducial markers that are part of the same plate to be a few pixels away from colinearity. Hence, the search for the boundary of the object in both input images, in order to provide the boundary conditions needed by Eq. 5.5, could benefit from the determination of this value at a sub-pixel precision. Moreover, the calculation of the positions in one input image, homologous to every pixel of the other input image, was done by accounting for the fractional part of the result. However, the intensity at such "inter-pixel" positions was calculated by linear interpolation between



A



B

Figure 5.5: (A) Result of the processing of the two images of Fig. 5.2 whose gray scales were reduced to 6 bits. (B) Image obtained with the same input images but on which was applied the blurring function described by Eq. 5.29.

the adjacent intensity values, a possible element of inaccuracy when sharp intensity gradients are present.

It would appear then that this algorithm is a promising way to cope with all static field errors. This provides a remedy for main field inhomogeneities as well as for susceptibility and chemical-shift effects, yet requires only conventional pulse sequences. Nevertheless, the sensitivity of this algorithm to digitization errors makes its adaptation difficult without an increase in image detail. An improvement that would allow at least the use of such processed images for position calculation along with narrow bandwidth images with good SNR for qualitative analysis would be most valuable.

At the origin of the current limitation is the fact that the processing relies on two input images with a consequent increase in the sensitivity toward digitization errors. A possible avenue to improve the adaptation of this algorithm could be its application on images expanded to a greater image matrix through the use of an interpolation scheme such as the *sinc* interpolation. This would in the first place improve the precision of the boundary condition determination and possibly yield a reconstructed image of a quality comparable to the original one. Such post-processing would advantageously be carried out on a more powerful workstation where the speed and memory considerations would not constitute a problem.

Chapter 6

Conclusion

6.1 Summary

MR images are affected by the presence of geometrical distortion in contrast to computed tomography which can be considered, for most purposes, as distortion free. Reasons for the presence of distortion in MRI are generally recognized as being main field inhomogeneity, susceptibility effects, chemical shift, gradient field non-linearity and induced transient currents from gradient switching. For most purposes, the presence of distortion in medical images has no detrimental consequence. Stereotaxy, on the other hand, constitutes an exception to this rule. For stereotactic treatment such as radiosurgery, it is generally agreed upon that 1mm is the upper limit of target position inaccuracy that can be admitted.

Many basic considerations are important in the study of the distortion phenomenon in MRI. The occurrence of the first three causes of image distortion stated above (that can be called generalized static field errors) can be minimized by the use of a higher readout gradient strength. Nevertheless, the signal-to-noise ratio (SNR) is decreased when a greater bandwidth is employed, thus a tradeoff has to be made between SNR and distortion from generalized static field errors at a given acquisition time. When 2D FT methods are used, geometrical distortion from generalized static field errors may

also be present in the slice selection direction and are seen when a non-planar excited slice is obtained. This problem can be circumvented by the use of 3D FT in which slice selection is replaced by phase encoding, since such encoding is immune from this type of distortion.

Experiments were carried out using a 1.5T S15HP Gyroscan imager in order to verify the contribution of the various causes of image distortion. Since many causes of image distortion tend to become more important away from the magnet isocenter, it is appropriate to specify the volume over which spatial linearity is required. In the case of stereotactic imaging with the OBT stereotactic frame, it seems reasonable to expect good image linearity when considering the head alone. However, the fiducial markers fall in the area where the geometrical integrity of the image deteriorates rapidly and may affect the localization of the innermost structures because of their role in the calculation of the frame coordinates. This problem calls for an optimal centering of the stereotactic frame about the magnet isocenter. Where the precision of the data allowed it, it appeared that the main field inhomogeneity was the dominant cause of image distortion, although there is good evidence that gradient non-linearity is involved as well. Furthermore, the role of eddy currents in geometrical distortion could not be demonstrated by the use of pulse sequences with different echo times.

A phenomenon other than the inherent distortion of the imager seems to be the cause of a yet greater distortion effect involving the top plate which is transversely oriented and placed on the cranial side of the frame, thus only visible in coronal and sagittal images. Its dependence on readout gradient strength indicates the involvement of either main field inhomogeneity or bulk magnetic susceptibility effect arising from the combined influence of the magnetic susceptibility, the shape and the orientation with respect to the main field. Further experiments can show that a fiducial marker plate undergoes such distortion from bulk magnetic susceptibility effect when the normal of its plane is parallel with B_0 , an orientation assumed only by the top plate. Hence, in order to account for this phenomenon, it is necessary to consider both the influence of the medium surrounding the channels, or namely the orientation that this medium

assumes with respect to B_0 , and the orientation of these channels.

This along with experimental data indicate that the magnetic susceptibility of channels parallel to B_0 , as well as perpendicular to B_0 but with the normal of the plate containing them perpendicular to the field, are close to each other and such that the channels will not exhibit a distortion effect noticeable in an imaging experiment like the ones performed. However, the channels that are perpendicular to the main magnetic field and that are part of a plate whose plane has a normal parallel to B_0 have a magnetic susceptibility that differ from the first group by a value comprised between 200 and 300 Hz at 1.5T.

This can be easily demonstrated as being detrimental to the accuracy of stereotactic position calculation. The discrepancy in resonant frequency between the perpendicular channels contained in plates of either orientation indicates a remedy to the problem. It simply consists of "sandwiching" the channels of the top plate with supplementary plexiglas along the direction of B_0 in order to model the case of a perpendicular channel contained in a plate whose plane has a normal perpendicular to the main field.

Shimming methods are essential in improving the main field inhomogeneity, but are not sufficient to eliminate entirely its contribution to inherent distortion. A lack often encountered with other distortion correction methods is their failure to account for susceptibility effects and chemical shift, necessitating the use of a patient based correction. One method that does not suffer from the above limitation is based on the use of two images acquired at two different readout gradient strengths in order to post-process a third image in which distortion is absent. The method successfully treats all three causes of static field errors. Spurious gradients of amplitude smaller than the weaker of the two readout gradient amplitudes utilized for input image acquisition can be handled. A version of this method for 3D FT images was developed but a 2D FT version that copes with error on slice selection is possible as well [17]. The algorithm was validated with the help of two input images of a phantom mounted in the OBT stereotactic frame, thus allowing for position evaluation with the help of the

stereotactic utilities. Distortion was successfully removed. Nevertheless, the method will benefit from the use of the full image dynamic range information.

6.2 Future work

It appears that an evaluation of the inherent distortion of the imager using a phantom with a finer but denser pattern could allow a better evaluation of this parameter. The improved distortion mapping combined with a technique allowing for the evaluation of the field inhomogeneity, such as phase imaging [86], could provide a more precise figure concerning the impact of gradient non-linearity and the value of warping methods to counteract it.

The analytical evaluation of the bulk magnetic susceptibility of the channels contained in the fiducial marker plates could allow for the development of precise guidelines concerning the design of such plates. Moreover, it appears that it could be useful to devise a correction scheme that would handle the distortion effect of the fiducial markers from bulk magnetic susceptibility effects or the presence of aluminum components in the frame. For instance, when only one channel out of the three appearing in the image is affected by the vicinity of an aluminum post (as it is the case with most coronal slices with the OBT frame), it could be shifted along the readout gradient direction in order to force it to become colinear with the two other markers that are known to be exempt from this problem.

Likewise, the knowledge of the relative positions of the fiducial marker plates could be the basis of a treatment that would detect and correct the bulk magnetic susceptibility effect occurring with the top plate. This is seen in the fact that this effect uniformly shifts the three markers of the top plate along the readout direction, while the screen position (u_i, v_i) of these three markers can be determined in a unique way from the position of the markers that are part of the two other plates appearing in the image, thus avoiding the need to use the corrupted screen position of the top plate when

applying Eq. 3.1.

The distortion correction method based on the use of two input images can seemingly be improved if applied to an expanded matrix size in order to solve the problem of digitization errors. This expansion could be performed using sinc interpolation. Furthermore, it seems that the full image dynamic range should be used for the purpose of applying the correction technique.

Bibliography

- [1] C.B. Ahn and Z.H. Cho. Analysis of eddy currents in nuclear magnetic resonance imaging. *Magnetic Resonance in Medicine*, 17:149-163, 1991.
- [2] C.B. Ahn and Z.H. Cho. Analysis of the eddy-current-induced artifacts and the temporal compensation in nuclear magnetic resonance imaging. *IEEE Transactions on Medical Imaging*, 10:47-52, 1991
- [3] D.E. Andrews. Magnet homogeneity and testing of MRI magnets. In *MRI: acceptance testing and quality control*, pages 77-81, Winston-Salem, NC, April 6-8 1988.
- [4] G. Arfken. *Mathematical methods for physicists*. Academic Press, Orlando, FL, 1985.
- [5] P. Bendel. Echo-projection imaging: a method to obtain NMR images undistorted by magnetic field inhomogeneities. *IEEE Transactions on Medical Imaging*, MI-4:114-119, 1985.
- [6] G.D. Bergland. A guided tour of the fast Fourier transform. *IEEE spectrum*, 41-52, July 1969.
- [7] W. Birg, f. Mundinger, and M. Mohadjer. X-ray and MR-stereotaxy for functional and nonfunctional neurosurgery. *Applied Neurophysiology*, 48:22-29, 1985.
- [8] F. Bloch. Nuclear induction. *Physical Review*, 70:460-474, 1946.

- [9] F. Bloch, W.W. Hansen, and M. Packard. The nuclear induction experiment. *Physical Review*, 70:474-485, 1946.
- [10] R. Bowtell and P. Mansfield. Gradient coil design using active magnetic screening. *Magnetic Resonance in Medicine*, 17:15-21, 1991.
- [11] R. N. Bracewell. *The Fourier Transform and its Physical Applications*. McGraw Hill, New York, 1978.
- [12] W.G. Bradley, K.E. Kortman, and J.V. Crues. Central nervous system high-resolution magnetic resonance imaging: effect of increasing spatial resolution on resolving power. *Radiology*, 156:93-98, 1985.
- [13] R.A. Brown, T.S. Roberts, and A.G. Osborn. Stereotaxic frame and computer software for CT-directed neurosurgical localization. *Investigative Radiology*, 15:308-312, 1980.
- [14] P.T. Callaghan. Susceptibility-limited resolution in nuclear magnetic resonance microscopy. *Journal of Magnetic Resonance*, 87:304-318, 1990.
- [15] H.Y. Carr and E.M. Purcell. Effects of diffusion on free precession in NMR experiments. *Physical Review*, 94:630-635, 1954.
- [16] H. Chang and J.M. Fitzpatrick. Geometrical image transformation to compensate for MRI distortions. In *Medical Imaging IV: Image Processing*, 1990.
- [17] H. Chang and J.M. Fitzpatrick. A technique for accurate magnetic resonance imaging in the presence of field inhomogeneities. Submitted to *IEEE Transactions on Medical Imaging*.
- [18] C.-N. Chen and D.I. Hoult. *Biomedical magnetic resonance technology*. Adam Hilger, Bristol and New York, 1989.

- [19] Z.H. Cho, D.J. Kim, and Y.K. Kim. Total inhomogeneity correction including chemical shifts and susceptibility by view angle tilting. *Medical Physics*, 15:7-11, 1988.
- [20] S.C.-K. Chu, Y. Xu, J.A. Balschi, and C.S. Springer. Bulk magnetic susceptibility shifts in NMR studies of compartmentalized samples: use of paramagnetic reagents. *Magnetic Resonance in Medicine*, 13:239-262, 1990.
- [21] R.H. Clarke. Investigations of the central nervous system. Methods and instruments. *Johns Hopkins Hospital Special Report, Special Volume*, 1-162, 1920.
- [22] A.G. Collins, D. Rodger, P. Eastham, P.J. Leonard, D.J. Bryant, and I.R. Young. Correction of eddy currents using shaped gradient pulses to avoid hardware modification. In *Proc. 8th Society of Magnetic Resonance in Medicine*, page 967, Amsterdam, The Netherlands, August 12-18 1989.
- [23] L.F. Czervionke. Magnetic susceptibility artifacts in gradient-recalled echo MR imaging. *American Journal of Neuroradiology*, 9:1149-1155, 1988.
- [24] R. Damadian. Tumor detection by NMR. *Science*, 171:1151, 1971.
- [25] J.H. den Boef, C.M.J. van Uijen, and C.D. Holzcherer. Multiple-slice NMR imaging by three-dimensional Fourier zeugmatography. *Physics in Medicine and Biology*, 29:857-867, 1984.
- [26] C. Dittmar. Über die lage des sogenannten gefäßszentrums in der medulla oblongata. *Ber Saechs Ges Wiss Leipzig (Math Phys)*, 25:449-469, 1873.
- [27] M. Drangova. *Stereotactic neurosurgical planning using magnetic resonance imaging distortion evaluation*. Master's thesis, McGill University, Medical Physics Unit, Montreal Neurological Institute, April 1987.
- [28] W.A. Edelstein, G.H. Glover, C.J. Hardy, and R.W. Redington. The intrinsic signal-to-noise ratio in NMR imaging. *Magnetic Resonance in Medicine*, 3:604-618, 1986.

- [29] W.A. Edelstein, J.M.S. Hutchison, G. Johnson, and T. Redpath. Spin warp imaging and applications to human whole-body imaging. *Physics in Medicine and Biology*, 25:751-756, 1980.
- [30] H. Egloff. Elimination of base field shifts due to pulsed magnetic gradients. In *Proc. 8th Society of Magnetic Resonance in Medicine*, page 969, Amsterdam, The Netherlands, August 12-18 1989.
- [31] A.C. Evans, C. Beil, S. Marrett, C.J. Thompson, and A. Hakim. Anatomical functional correlation using an adjustable MRI based atlas with PET. *Journal of Cerebral Blood Flow and Metabolism*, 6:813-830, 1988.
- [32] E. Feig, F. Greenleaf, and M. Perlin. Magnetic resonance imaging with non-uniform fields. *Physics in Medicine and Biology*, 31:1091-1099, 1986.
- [33] E. Feig, F. Greenleaf, and M. Perlin. Self-correcting NMR image recovery under magnetic fields with large inhomogeneities. In *Proc. 3th Society of Magnetic Resonance in Medicine*, pages 227-228, New York, NY, August 13-17 1984.
- [34] J.M. Fitzpatrick, D.R. Pickens, H. Chang, Y. Ge, and M. Ozkan. Geometrical transformations of density images. In *Proc. Conf. Science and Engin. of Medical Imaging*, pages 12-21, 1989.
- [35] A. Gauvin and T.M. Peters. MR image distortion in the context of stereotaxy. In *Proceedings of the Canadian Organization of the Physicists in Medicine*, page 12, Winnipeg, Manitoba, June 21-22 1991.
- [36] M.J.E. Golay. Field homogeneity coils for nuclear spin resonance instrumentation. *The Review of Scientific Instrumentation*, 29:313-315, 1958.
- [37] P.M. De Groot. Image intensifier design and specifications. In *AAPM 91 summer school: specification, acceptance testing and quality control of diagnostic x-ray imaging equipment*, pages 477-510, University of California, Santa Cruz, July 15-19 1991.

- [38] E.L. Hahn. Spin echos. *Physical Review*, 80:580-594, November 1950.
- [39] M.I. Hariz, A.T. Bergenheim, A.A.F. DeSalles, L. Rabow, and T. Trojanowski. Percutaneous stereotactic brain tumour biopsy and cyst aspiration with a non-invasive frame. *British Journal of Neurosurgery*, 4:397-406, 1990.
- [40] D.G. Hawksworth. New magnets designs for MR. *Magnetic Resonance in Medicine*, 17:27-32, 1991.
- [41] R.M. Henkelman and M.J. Bronskill. Artifacts in magnetic resonance imaging. *Reviews in Magnetic Resonance Imaging*, 2:1-126, 1987.
- [42] C.J. Henri. *Application of digital subtraction angiography to stereotactic neurosurgery planning*. Master's thesis, McGill University, Medical Physics Unit, Montreal Neurological Institute, October 1989.
- [43] C.J. Henri. Personal communication. 1991.
- [44] C.J. Henri, L.D. Collins, and T.M. Peters. Multimodality image integration for stereotactic surgical planning. *Medical Physics*, 18:167-177, 1991.
- [45] W.S. Hinshaw. Image formation by nuclear magnetic resonance. *Journal of Applied Physics*, 47:3709-3721, 1976.
- [46] H. Hirschberg. Localization of brain tumors with a simple scalp-mounted fiducial device. *The Journal of Neurosurgery*, 70:280-281, 1989.
- [47] N. Hoffman. Personal communication. 1992.
- [48] V. Horsley and R.H. Clarke. The structure and functions of the cerebellum examined by a new method. *Brain*, 31:45-124, 1908.
- [49] G.N. Hounsfield, J. Ambrose, and B.J. Perry. Computerized transverse axial scanning (tomography). *British Journal of Radiology*, 46:1016-1051, 1973.

- [50] D.G. Hughes, S. Robertson, and P.S. Allen. Analysis of the eddy current fields in a 40 cm bore magnet. In *Proc. 9th Society of Magnetic Resonance in Medicine*, page 539, New York, NY, August 17-21 1990.
- [51] J.M.S. Hutchison, R.J. Sutherland, and J.R. Mallard. NMR imaging: image recovery under magnetic fields with large non-uniformities. *Journal of Physics E: Scientific Instrumentation*, 11:217-221, 1978.
- [52] P. Jehenson, M. Westphal, and N. Schuff. Measurement and exact compensation of eddy currents induced by pulsed magnetic field gradients in NMR systems. In *Proc. 8th Society of Magnetic Resonance in Medicine*, page 966, Amsterdam, The Netherlands, August 12-18 1989.
- [53] A.B. Jenny, P.R. Biondetti, B. Layton, and R.H. Knapp. The computer and stereotactic surgery in neurological surgery. *Computers in Medical Imaging and Graphics*, 12:75-83, 1988.
- [54] E.A. Jonckheere and Y.S. kwoh. Correction of distortion of magnetic resonance (MR) pictures for MR-guided robotic stereotactic procedures. *Optical Engineering*, 29:1469-1477, 1990.
- [55] P.M. Joseph. *NMR in medicine: the instrumentation and clinical application*, chapter Pulse sequences for magnetic resonance imaging, pages 71-84. American Institute of Physics, 1986.
- [56] D. Kahaner, C. Moler, and S. Nash. *Numerical methods and software*. Prentice-Hall, Englewood Cliffs, New Jersey, 1989.
- [57] A.C. Kak and M. Slaney. *Principles of computerized tomographic imaging*. IEEE Press, New York, NY, 1988.
- [58] A. Kato, T. Yoshimine, T. Hayakawa, Y. Tomita, T. Ikeda, M. Mitomo, K. Harada, and H. Mogami. A frameless, armless navigational system for

- computerized-assisted neurosurgery. *The Journal of Neurosurgery*, 74:845-849, 1991.
- [59] A. Kawanaka and M. Takagi. Correction method of image distortion. In *Proc. Conf. Science and Engin. of Medical Imaging*, pages 173-177, July 1984.
- [60] A. Kawanaka and M. Takagi. Estimation of static magnetic field and gradient fields from NMR image. *Journal of Physics E: Scientific Instrumentation*, 19:871-875, 1986.
- [61] J.E. Kirsh and L.S. Makow. Steady state evolution of eddy currents. In *Proc. 9th Society of Magnetic Resonance in Medicine*, page 537, New York, NY, August 17-21 1990.
- [62] C. Kittel. *Introduction to solid state physics*. John Wiley & Sons, New York, NY, 1986.
- [63] A. Kumar, D. Welti, and R.R. Ernst. NMR Fourier Zeugmatography. *Journal of Magnetic Resonance*, 18:69-83, 1975.
- [64] C.M. Lai. Reconstructing NMR images under magnetic fields with large inhomogeneities. *Journal of Physics E: Scientific Instrumentation*, 15:1093, 1982.
- [65] P.C. Lauterbur. Image formation by induced local interactions: examples using nuclear magnetic resonance. *Nature*, 242:190-191, 1973.
- [66] L. Leksell. A stereotaxic apparatus for intracerebral surgery. *Acta Chirurgica Scandinavica*, 99:229-233, 1949.
- [67] L. Leksell. *Stereotaxis and radiosurgery: An operative system*. Charles C. Thomas, Springfield, IL, 1971.
- [68] L. Leksell and B. Jernberg. Stereotaxis and tomography. *Acta Neurochirurgica*, 52:1-7, 1980.

- [69] L. Leksell, D. Leksell, and J. Schwebel. Stereotaxis and nuclear magnetic resonance. *J Neurol Neurosurg Psychiatry*, 48:14-18, 1985.
- [70] D.N. Levin, C.A. Pelizzari, G.T.Y. Chen, C.-T. Chen, and M.D. Cooper. Retrospective geometric correlation of MR, CT, and PET images. *Radiology*, 169:817-823, 1988.
- [71] J.M. Libove and J.R. Singer. Resolution and signal to noise ratio in NMR imaging of the human body. *Journal of Physics E: Scientific Instrumentation*, 13:38-44, 1980.
- [72] K.M. Ludeke, P. Roshmann, and R. Tischler. Susceptibility artefacts in NMR imaging. *Magnetic Resonance Imaging*, 3:329-343, 1985.
- [73] L.D. Lunsford, editor. *Modern Stereotactic neurosurgery*, chapter General concepts of stereotactic surgery. Martinus Nijhoff Publishing, Boston, 1988.
- [74] P.D. Majors, J.L. Blackley, S.A. Altobelli, A. Caprihan, and E. Fukushima. Eddy-current compensation by direct field detection and digital gradient modification. *Journal of Magnetic Resonance*, 87:548-553, 1990.
- [75] S. Majumdar, D. Thomasson, A. Shimakawa, and H. Genant. Correlation of inherent magnetic field inhomogeneity in vertebral bodies with trabecular bone density. In *Proc. 9th Society of Magnetic Resonance in Medicine*, page 582, New York, NY, August 17-21 1990.
- [76] P. Mansfield and B. Chapman. Active magnetic screening of gradient coils in NMR imaging. *Journal of Magnetic Resonance*, 66:573-576, 1986.
- [77] P. Mansfield and B. Chapman. Multishield active magnetic screening of coil structures in NMR. *Journal of Magnetic Resonance*, 72:211-223, 1987.
- [78] P. Mansfield and A.A. Maudsley. Line scan proton spin imaging in biological structures by NMR. *Physics in Medicine and Biology*, 21:847-852, 1976.

- [79] P. Mansfield and I.L. Pykett. Biological and medical imaging by NMR. *Journal of Magnetic Resonance*, 29:355-373, 1978.
- [80] S. Marrett, A.C. Evans, and T.M. Peters. Volume of interest (VOI) atlas for the analysis of neurophysiological image data. In *Proceedings of SPIE Medical Imaging*, 1989.
- [81] S. Meiboom and D. Gill. Modified spin-echo method for measuring nuclear relaxation times. *Review of Scientific Instruments*, 29:688-691, 1958.
- [82] R.A. Meuli, F.R. Verdun, and F.O. Bochud. Assessments of MR distortions for stereotaxic neurosurgery. In *Proc. 10th Society of Magnetic Resonance in Medicine*, page 949, San Fransisco, CA, August 10-16 1991.
- [83] J.B. Miller and A.N. Garroway. Removal of static inhomogeneity and chemical-shift effects in NMR imaging. *Journal of Magnetic Resonance*, 67:575-579, 1986.
- [84] M.A. Morich, D.A. Lampman, W.R. Dannels, and F.T.D. Goldie. Exact temporal eddy current compensation in magnetic resonance imaging systems. *IEEE Transactions on Medical Imaging*, 7:247-254, 1988.
- [85] O. Nalcioglu. Basics of nuclear magnetic resonance (NMR) imaging. *Physica Medica*, 3:1-60, 1987.
- [86] J.G. Och, G.D. Clarke, W.T. Sobol, C.W. Rosen, and S.K. Mun. Acceptance testing of magnetic resonance imaging system: report of AAPM nuclear magnetic resonance task group no. 6. *Medical Physics*, 19:217-229, 1992.
- [87] M. O'Donnell and W.A. Edelstein. NMR imaging in the presence of magnetic field inhomogeneities and gradient field nonlinearities. *Medical Physics*, 12:20-26, 1985.
- [88] A. Olivier, G. Bertrand, and T.M. Peters. Stereotactic systems and procedures for depth electrode placement: technical aspects. *Applied Neurophysiology*, 46:37-40, 1983.

- [89] A. Olivier, T.M. Peters, and G. Bertrand. Stereotactic system and apparatus for use with MRI, CT and DSA. *Applied Neurophysiology*, 48:94-96, 1986.
- [90] D.I. Parker and G.T. Gullberg. Signal-to-noise efficiency in magnetic resonance imaging. *Medical Physics*, 17:250-257, 1990.
- [91] T.M. Peters, J. Clark, G.B. Pike, M. Drangova, and A. Olivier. Stereotactic surgical planning with magnetic resonance imaging digital subtraction angiography and computed tomography. *Applied Neurophysiology*, 50:33-38, 1987.
- [92] T.M. Peters, J.A. Clark, G.B. Pike, C. Henri, L. Collins, D. Leksell, and O. Jeppsson. Stereotactic neurosurgery planning on a PC based workstation. In *1092 Medical Imaging III: Image Processing*, pages 556-564, 1989.
- [93] T.M. Peters, J.A. Clark, G.B. Pike, C. Henri, L. Collins, D. Leksell, and O. Jeppsson. Stereotactic neurosurgery planning on a personal-computer-based workstation. *Journal of Digital Imaging*, 2:75-81, 1989.
- [94] T.M. Peters, M. Drangova, J.A. Clark, G.B. Pike, and A. Olivier. Image distortion in MR imaging for stereotactic surgery. In *Proc. 7th Society of Magnetic Resonance in Medicine*, page 1066, San Francisco, CA, August 20-26 1988.
- [95] T.M. Peters, M. Drangova, G.B. Pike, A. Olivier, and R. Ethier. The applicability of MRI for stereotactic neurosurgical planning. In *Proc. 6th Society of Magnetic Resonance in Medicine*, page 623, New York, NY, August 17-21 1987.
- [96] T.M. Peters and B.C. Sanctuary. *Technology of nuclear magnetic resonance*, chapter Overview of NMR Reconstruction Principles, pages 15-26. Society of Nuclear Medicine, 1984.
- [97] C. Picard, A. Olivier, and G. Bertrand. The first human stereotaxic apparatus. *The Journal of Neurosurgery*, 59:673-676, 1983.
- [98] G.B. Pike, E.B. Podgorsak, T.M. Peters, C. Pla, and A. Olivier. Three-dimensional isodose distributions in stereotactic radiosurgery. *Proceedings of the*

Xth Meeting of the World Society for Stereotactic and Functional Neurosurgery, 519-524, 1990.

- [99] E.B. Podgorsak, G.B. Pike, A. Olivier, M. Pla, and L. Souhami. Radiosurgery with high energy photon beams: a comparison among techniques. *International Journal of Radiation Oncology Biology Physics*, 16:857-865, 1989.
- [100] E.B. Podgorsak, G.B. Pike, M. Pla, A. Olivier, and L. Souhami. Stereotactic radiosurgery with photon beams: physical aspects and adequacy of linear accelerators. *Radiotherapy and Oncology*, 17:349-358, 1990.
- [101] E.M. Purcell, H.C. Torrey, and R.V. Pound. Resonance absorption by nuclear magnetic moments in solids. *Physical Review*, 69:127, 1946.
- [102] D. Purdy. Acceptance testing of magnetic resonance imagers: which tests are worthwhile? In *MRI acceptance testing and quality control: the role of the clinical medical physicist*, pages 115-125, Winston-Salem, NC, April 1988.
- [103] T. Riechert. *Stereotactic brain operations*. Hans Huber, Bern, Stuttgart, Vienna, 1980.
- [104] F. Roméo and D.I. Hoult. Magnet field profiling: analysis and correcting coil design. *Magnetic Resonance in Medicine*, 1:44-65, 1984.
- [105] J. Rousseau, P. Clarysse, S. Blond, D. Gibon, P. Dubois, and X. Marchandise. A new method for stereotaxic localization using MRI. In *Proc. 9th Society of Magnetic Resonance in Medicine*, page 183, New York, NY, August 17-21 1990.
- [106] L. Schad, S. Lott, F. Schmitt, V. Strurm, and W. Lorenz. Correction of spatial distortion in MR imaging: a prerequisite for accurate stereotaxy. *Journal of Computer Assisted Tomography*, 11:499-505, 1987.
- [107] K. Sekihara, M. Kuroda, and H. Kohno. Image restoration from non-uniform magnetic field influence for direct fourier NMR imaging. *Physics in Medicine and Biology*, 29:15-24, 1984.

- [108] K. Sekihara, S. Matsui, and H. Kohno. NMR imaging for magnets with large non-uniformities. *IEEE Transactions on Medical Imaging*, MI-4:50-55, 1985.
- [109] K. Sixel and E.B. Podgorsak. Cylindrical dose distribution in dynamic rotation radiosurgery. In *Medical Physics*, page 621, San Francisco, CA, 21-25 July 1991.
- [110] G.W. Smith. *Diamagnetic susceptibilities of organic compounds*, pages E111-E119. CRC Press, Inc., Boca Raton, FL, 1984.
- [111] E.A. Spiegel, H.T. Wycis, and E.G. Szekely. Stereotaxic apparatus for operations on the human brain. *Science*, 106:349-350, 1947.
- [112] J. Talairach, P. Aboulker, and G. Ruggiero. Utilisation de la méthode radiostéréotaxique pour le traitement radioactif *in situ* des tumeurs cérébrales. *Revue de neurologie*, 90:656-658, 1953.
- [113] J. Talairach, H. Hécaen, and M. David. Recherches sur la coagulation thérapeutique des structures sous-corticales chez l'homme. *Revue de neurologie*, 81:4-24, 1949.
- [114] D.G. Taylor, R. Inamdar, and M.-C. Bushell. NMR imaging in theory and in practice. *Physics in Medicine and Biology*, 33:635-670, 1988.
- [115] S.R. Thomas. *NMR in medicine: The instrumentation and clinical application*, chapter Gradient coil technology, pages 111-141. American Institute of Physics, 1986.
- [116] E.M. Todd. *Manual of stereotactic procedures*. Codman and Shurtleff, Randolph, MA, 1967.
- [117] R. Turner and R.M. Bowley. Passive screening of switched magnetic field gradients. *Journal of Physics E: Scientific Instrumentation*, 19:876-879, 1986.
- [118] K.R. Winston and W. Lutz. Linear accelerator as a neurosurgical tool for stereotactic radiosurgery. *Neurosurgery*, 22:454-464, 1988.

- [119] T.S. Wong and D. Rosenfeld. Spin-inversion imaging: a technique for NMR imaging under magnetic fields with high field nonuniformities. *IEEE Transactions on Medical Imaging*, MI-6:148-156, 1987.
- [120] Y. Xu, J.A. Balschi, and C.S. Springer. Magnetic susceptibility shift selected imaging: MESSI. *Magnetic Resonance in Medicine*, 16:80-90, 1990.
- [121] Y. Xu and C.S. Springer. On the theory of bulk magnetic susceptibility shift: the case of a cylinder at any angle to B. In *Proc. 9th Society of Magnetic Resonance in Medicine*, page 130, New York, NY, August 17-21 1990.
- [122] E. Yamamoto and H. Kohno. Correction of distortion caused by field errors in MR imaging. In *Proc. 6th Society of Magnetic Resonance in Medicine*, page 402, New York, NY, August 17-21 1987.
- [123] I.R. Young, S. Khenia, G.T. Thomas, C.H. Davis, D.G. Gadian, I.J. Cox, B.D. Ross, and G.M. Bydder. Clinical magnetic susceptibility mapping of the brain. *Journal of Computer Assisted Tomography*, 11:2-6, 1987.
- [124] D.N. Zernov. L'encéphalomètre. *Proc Gen Clin Ther*, 19:302, 1890.
- [125] J. Zhang, M.F. Lévesque, C.L. Wilson, R.M. Harper, J. Engel, R. Lufkin, and E.J. Behnke. Multimodality imaging of brain structures for stereotactic surgery. *Radiology*, 175:435-441, 1990.

Glossary

List of Symbols

Symbol	Meaning
t_x	half duration of readout gradient application
τ_y	duration of y preparation gradient application
τ_z	duration of z preparation gradient application
J	Jacobian of coordinate transformation
κ	Boltzmann constant
T	temperature
$N_{\parallel\parallel}$	number of parallel magnetic moments
$N_{\parallel\uparrow}$	number of antiparallel magnetic moments
V	root mean square of voltage fluctuation
$\Delta\nu$	frequency bandwidth
w_x, w_y, w_z	voxel dimensions
r	number of signal averages
N_x, N_y, N_z	k-space dimensions
k_x, k_y, k_z	spatial frequency coordinates
u	step response
τ_i	i^{th} eddy current time constant
β_i	i^{th} eddy current amplitude
T_i	i^{th} correction time constant
α_j	j^{th} correction amplitude

List of Symbols (continued)

Symbol	Meaning
δ	shift in resonant frequency
δ_σ	shift from host molecule electronic shielding effects
δ_s	shift from solvent electronic shielding effects
δ_χ	shift from bulk magnetic susceptibility effects
χ	volumetric susceptibility
s	standard deviation
D_i	homogeneous BMS component
I_i	inhomogeneous BMS component
τ	quarter of alternating gradient period
\min	smallest value operator
i, j, k	unit vectors of cartesian coordinate system
B_1	amplitude of RF field
θ	tip angle
T_1	spin-lattice relaxation time
T_2	spin-spin relaxation time in a homogeneous main field
T_2^*	spin-spin relaxation time
M	magnetization
M_0	size of magnetization
B	main magnetic field
B_0	nominal size of the main magnetic field
ΔB	deviation of main field from homogeneity
H	magnetic intensity
G_x, G_y, G_z	size of x, y, z magnetic gradient
$\Delta G_x, \Delta G_y, \Delta G_z$	deviation of x, y, z gradient at a reference gradient current
h	Planck constant
\hbar	$h/2\pi$
γ	gyromagnetic ratio

List of Symbols (continued)

Symbol	Meaning
Ω	angular frequency
\mathbf{r}	spatial position
\mathbf{r}'	distorted spatial position
ω	nominal resonant frequency
U	potential energy
t	time
x,y,z	cartesian coordinates
x_1,y_1,z_1	rotating frame coordinates
x'	distorted readout position
r,θ,ϕ	spherical coordinates
u,v	screen coordinates
S	induced signal
λ,σ,ρ	1D,2D,3D spin density
TE	echo time
TR	repetition time
n	number of slices
th	slice thickness
G_1,G_2	gradient strengths of input images
α	G_1/G_2
∇	nabla operator
t_a	time of application of RF pulse
μ	magnetic moment
L	angular momentum
J	total angular momentum

List of Abbreviations

Abbreviation	Meaning
AP	anterior-posterior
AVM	arterio-venous malformation
BMS	bulk magnetic susceptibility
CC	cranial-caudal
CT	computed tomography
DSA	digital subtraction angiography
FT	Fourier transform
FFT	fast Fourier transform
FID	free induction decay
FOV	field of view
LR	left-right
MR	magnetic resonance
MRI	magnetic resonance imaging
MRS	magnetic resonance spectroscopy
NMR	nuclear magnetic resonance
OBT	Olivier-Bertrand-Tipal
PSF	point spread function
RF	radio frequency
SE	spin echo
SNR	signal-to-noise ratio
1D	one dimensional
2D	two dimensional
3D	three dimensional